MATERIAL FLOW ANALYSIS IN FRICTION STIR WELDING OR PROCESSING

Ph.D. THESIS

by

RAHUL KUMAR

DEPARTMENT OF METALLURGICAL & MATERIALS ENGINEERING
INDIAN INSTITUTE OF TECHNOLOGY ROORKEE
ROORKEE- 247667 (INDIA)
FEBRUARY, 2019

MATERIAL FLOW ANALYSIS IN FRICTION STIR WELDING OR PROCESSING

A THESIS

Submitted in partial fulfilment of the
requirements for the award of the degree

of

DOCTOR OF PHILOSOPHY

in

METALLURGICAL & MATERIALS ENGINEERING

by

RAHUL KUMAR

DEPARTMENT OF METALLURGICAL & MATERIALS ENGINEERING
INDIAN INSTITUTE OF TECHNOLOGY ROORKEE
ROORKEE- 247667 (INDIA)
FEBRUARY, 2019

INDIAN INSTITUTE OF TECHNOLOGY ROORKEE

CANDIDATE'S DECLARATION

I hereby certify that the work which is being presented in the thesis entitled **"MATERIAL FLOW ANALYSIS IN FRICTION STIR WELDING OR PROCESSING"** in partial fulfilment of the requirements for the award of the Degree of Doctor of Philosophy and submitted in the Department of Metallurgical & Materials Engineering of the Indian Institute of Technology Roorkee, Roorkee is an authentic record of my own work ingeniously carried out during the period from July, 2013 to February, 2019 under the supervision of Dr. Vivek Pancholi, Associate Professor, Department of Metallurgical and Materials Engineering, Indian Institute of Technology Roorkee, Roorkee.

The matter presented in the thesis has not been submitted by me for the award of any other degree of this or any other institute.

(RAHUL KUMAR)

This is to certify that the above statement made by the candidate is correct to the best of my knowledge.

(Vivek Pancholi)
Supervisor

The PhD Viva-Voce Examination of Mr. Rahul Kumar, Research Scholar, has been held on July 12, 2019.

Chairperson, SRC **Signature of External Examiner**

This is to certify that student has made all the correction in the thesis.

(Vivek Pancholi)
Supervisor **Head of the Department**
Dated: July 12, 2019

I am dedicating this thesis

With love and affection ***TO MY SISTER, Smt. Sandhya Devi Baghel***

ACKNOWLEDGEMENT

Completion of this thesis was possible with the support of several people. I would like to express my sincere gratitude to all of them. First of all, I am extremely grateful to my supervisor, Dr. Vivek Pancholi, Associate Professor, Department of Metallurgical and Materials Engineering, Indian Institute of Technology Roorkee, for his valuable guidance, scholarly inputs and consistent encouragement. This feat was possible only because of the unconditional support provided by him. A person with an amicable and positive disposition, he has always made himself available to clarify my doubts despite his busy schedule and I consider it as a great opportunity to do my doctoral programme under his guidance and to learn from his research expertise.

I wish to thank Dr. Anjan Sil, Professor and Head, Department of Metallurgical and Materials Engineering, for providing me nice work environment. I thank the SRC members, Dr. Ujjwal Prakash, Dr. B. S. S. Daniel, Dr. Devendra Singh, Department of Metallurgical and Materials Engineering and, Dr. R. P. Bharti, Chemical Engineering Department, for constant encoragment and support. I am thanking to all faculty members of the Department of Metallurgical and Materials Engineering for generously providing guidance whenever required. Mr. R. K. Sharma and Mr. Rajendra Sharma in the labs made sure that research resources are available in time.

I wish to thank Dr. R. P. Bharti, Associate Professor, Department of Chemical Engineering, to extended invaluable support in the thesis writing, computational analysis and for his valuable suggestions and concise comments on some of the research papers of the thesis.

I wish to express my gratitude to Dr. Ajay Gairola, Professor, Centre of Excellence in Disaster Mitigation and Management, for his support in allowing to use Particle Image Velocimetry (PIV) system located in the Wind Simulation Laboratory, Centre of Excellence in Disaster Mitigation and Management of the Institute.

I thank my seniors, juniors, friends and specially my research group members Mr. A. Raja, Mr. Suresh Sonkar, Dr. Kuldeep Kumar Saxena and Mr. Aniruddha Malakar, for their constant support and lively working environment. I was lucky to be a part of such a group filled with learning experiences. I also thank, Abhishek Kumar Lal, research scholar, Chemical Engineering Department, Ashutosh Sharma and Hemant Mittal, research scholars, Centre of Excellence in Disaster Mitigation and Management, for their help. Without their help and support it would not have been possible for me to complete my work.

A special thanks to my family. Words cannot express how grateful I am to my Mata ji Smt. Chandra Devi Baghel and Pita ji Shri Jeevaram Baghel for all of the sacrifices that they have made on my behalf and providing freedom to be myself. I wish to thank my Bhaiya and Bhabhi ji, Didi and Jija Ji, younger sister and brothers for their support and making me free from my social activities during my research work. And lovely thanks to my children team that called me Chacha and Mama for their best wishes.

I would like to thank to my beloved wife Er. Roopa Pal for supporting me for everything, and especially I can’t thank you enough for encouraging me throughout this experience. I am thankful to my beloved son Jatin Baghel whose smiling, loving and innocent face have always refreshed me and their innocent and naughty activities relieved the stress of my research work.

I am thankful to my father-in law Dr. Brijpal Singh Pal, mother-in-law Smt. Kavita Pal and brother-in-law Mr. Ashish Dhangar and their family for their support and good wishes.

I would like to thank everyone who is directly or indirectly involved to the successful completion of my thesis, I would like to sincere apology, if I could not mention anyone here. This could be due to lack of space but not due to lack of appreciation.

Finally, I thank God for letting me through all the difficulties. I have experienced Your guidance day by day. You are the one who let me finish my degree. I will keep on trusting You for my future. JAI BHOLENATH.

RAHUL KUMAR

ABSTRACT

Material flow in friction stir welding (FSW) process is a complex phenomenon, understanding of which plays a significant role in getting defect free weld. Additionally, quantification of the material flow characteristic in terms of strain, strain rate is important to obtain the required material properties in the weld region. Various techniques were used by researchers to understand material flow behaviour. In this work, material flow during FSW was investigated by using three different methods; i) by tracer insert technique using the same tracer and workpiece material, ii) in-situ material flow visualization by a new technique called particle image velocimetry, iii) by computational fluid dynamics.

Tracer insert technique: three dimensional material flow and strain accumulation during friction stir welding were investigated by inserting tracer extracted from the workpiece material. Same material for tracer and workpiece allowed accurate strain measurement during FSW. Complete material flow behaviour in three dimensions was obtained by embedding tracers in three orientations; transverse, longitudinal and parallel to the processing direction. Three prominent material movements were deduced from the study. First, rotation around tool pin of the material collected from the leading-advancing side and deposited at the trailing-advancing side. Second, vertical movement of the material from the trailing-advancing side in the cavity created at the back of the traversing tool. The flow occurred under the constraint imposed by the rotating shoulder, pin, and relatively hard surroundings. The constraint imposed by different bodies exerted a torque on the soft material and forced it to flow downward in AS and upward in RS. The surrounding hard material acted as a pivot to the vertical rotation. Third, extrusion and deposition of the material layer by layer from leading side towards trailing side via retreating side. Strain at different locations was determined by measuring the thickness of the deformed tracer. The maximum tensile strain of 2 was measured close to the top surface (near shoulder) and a maximum compressive strain of 0.4 was measured at 1.5 mm depth from the top surface.

Particle image velocimetry technique: Particle image velocimetry (PIV) technique has been adopted to understand the material flow and strain rate around the tool pin during friction stir welding (FSW). A transparent non-Newtonian fluid of similar viscoplastic behaviour as metallic material was selected as a modelling material. A negligible amount of micro-spherical glass particles were added in the modelling material, both of similar densities. Hence the physical

properties of the modelling material remained unaltered. The characteristics of material flow, in particular, flow velocity and strain rate were obtained by following the path of the tracer particles. Further, the results of PIV were validated by computational analysis. A rotational zone around the pin was formed due to large deformation of material close to the tool pin. The maximum velocity was found to be 85% of pin peripheral velocity, at 0.1 mm distance from pin surface at 300 rpm and 50 mm min^{-1}. The maximum strain rate was found 100 s^{-1}, at 0.47 mm distance from pin surface, at 300 rpm and 50 mm min^{-1} and increase from 20 s^{-1} to 145 s^{-1} with an increase in rotation speed from 75 rpm to 425 rpm. Predictive correlations were established for variations of velocity and maximum strain-rate as a function of rotational, traverse speeds and distance away from the tool pin surface. Overall, it is established that the PIV technique can successfully be utilized for the understanding of material flow and strain-rate behaviour during FSW.

Computational fluid dynamics: material flow velocity and strain rate around the tool pin during the friction stir welding process was investigated by computational fluid dynamics approach. The experimental results of PIV study were compared with numerical simulation results. The results from experimental and computational works were in good agreement. Maximum velocity and strain rate were found at the pin surface and have shown linear dependence on rotation speed. The maximum strain rate was found to increase from 48 s^{-1} to 275 s^{-1} with increase in rotation speed from 75 rpm to 425 rpm. However, at 0.47 mm from pin surface the strain rate was same as measured in PIV technique.

CONTENTS

DETAIL OF MATERIAL FLOW INVESTIGATION TECHNIQUES 41

MATERIAL FLOW ANALYSIS USING TI TECHNIQUE..57

LIST OF FIGURES

LIST OF TABLES

NOMENCLATURE

Symbol	**Description**
AS	Advancing side
CCD	Charge coupled device
CFD	Computational fluid dynamics
EDM	Electric discharge machining
FSW	Friction stir welding
FSP	Friction stir processing
FEM	Finite element method
FFT	Fast Fourier Transform
IA/IW	Interrogation area/ Interrogation window
LS	Leading side
MIG	Metal inert gas welding
Nd-YAG	Neodymium-Yttrium Aluminium Garnet
PCL	Process centreline
PIV	Particle image velocimetry
RS	Retreating side
RZ	Rotational zone
SP	Stagnation point
TIG	Tungsten inert gas welding
TIT	Tracer insert technique
TS	Trailing side
TZ	Transitional zone
T	Temperature, K
T_m	Melting point, K
N	Revolution per minute, rpm
K_t	Thermal conductivity, (W $m^{-1}K^{-1}$)
ρ	Density, kg m^{-3}
d_0	Un-deformed tracer thickness
d	Deformed tracer thickness
m	Consistency index, Pa s^n
n	Power law index

Δt	Laser pulse separation time, μs
N_i	Image number
u_{rms}	RMS value in X direction
v_{rms}	RMS value in Y direction
u	Velocity in X direction
v	Velocity in Y direction
V	Resultant velocity
p	Pressure, Pa
V_T	Traverse or welding speed
V_R	Tangential velocity/ Peripheral velocity
F_d	Drag force
F_g	Forging force
P	Weld-pitch, mm per revolution
τ	Shear stress, Pa
$\dot{\gamma}$	Rate of strain, s^{-1}
η	Viscosity, Pa.s

CHAPTER 1

INTRODUCTION

Friction stir welding (FSW) is a solid-state welding technology, which was invented by The Welding Institute (TWI) in 1991 [1]. Solid-state welding has been proven to be very effective in eliminating a large number of defects, like liquation cracking, high residual stresses, poor solidified microstructure, porosity, slag inclusion, incomplete penetration, solidification shrinkage, hydrogen attack, resulting from conventional fusion welding techniques like TIG, MIG, etc. All these defects act as a weak link in the weld joint, which significantly reduces the strength of the structure and its integrity. In Al alloys, the presence of the aluminium oxide layer on the surface which has a very high melting point than the base material creates an additional problem during arc welding. Thus, there is a need for a better alternative technique for welding of aluminium alloys without melting the material. FSW is one of the emerging solid-state welding processes, which has proven its capability of producing joints with higher strength and is extensively used in welding of different types of similar and dissimilar metals. FSW is especially suitable for the joining of many light alloys such as aluminium and magnesium [2-3].

The technique is very simple and offers enormous potential for joining and processing of low melting point materials. It is a severe plastic deformation process which involves deformation at high strain rates and elevated temperatures [5]. However, material flow during the FSW process is so complex that the weld formation mechanism has not been fully understood. Friction stir processing (FSP) is a derivative of FSW technique wherein the process is used for microstructural modification instead of joining [4, 6]. However, both FSW and FSP are similar in terms of material flow behaviour.

Material flow behaviour during FSW/P is one of the key factors that influence the quality of a joint and surface properties of material locally [7, 8]. There is a close relationship between the formation of defects and the flow behaviour of weld metal during FSW [9, 10]. Therefore, it is of vital importance to understand the weld metal flow behaviour in FSW. The material flow pattern actually helps in deciding the parameters required for particular tool geometry. Material flow field measurement provides quantitative information of FSW process such as local material flow velocity, strain and strain rate, which has a strong relationship with the microstructure.

The aim of the present study is to understand the material flow characteristics behaviour in FSW by different techniques such as tracer insert technique, particle image velocimetry technique and numerical modelling.

Structure of the thesis

The present thesis is divided into the following eight chapters. Chapter 1 consist of the introduction of the FSW process and its advantage over other joining processes. Role of material flow during FSW/P to achieve good quality welded zone or processed zone is discussed.

In Chapter 2, the literature review elaborates an understanding of material flow during FSW/P and factors affecting material flow during FSW/P are discussed in detail. This chapter contains discussion on the literature that used tracer insert technique (TIT) and numerical models to understand material flow after and during FSW. Particle image velocimetry (PIV) technique is introduced and its role in understanding material flow in other systems is discussed.

Chapter 3 contains, objectives of the present work to fill up the research gap. The objectives of the work are defined based on the important findings and gaps found in the reviewed literature.

In Chapter 4, the experimental procedure is explained in detail. Details of tracer insert technique used for material flow analysis, in particular, preparation of tracer is provided in this chapter. The second experimental technique used for material flow analysis was particle image velocimetry (PIV). Details of PIV measurement and selection of the transparent non-Newtonian material for experimental simulation and tracer particles for in-situ flow visualization is provided. The working of the PIV system and its components are described in details. Third, COMSOL Multiphysics CFD model for numerical simulation is explained.

In Chapter 5 results of material flow during friction stir welding process of 5083 Al alloy by tracer insert technique is presented. The tracers were embedded in three orientations and at different locations, to understand material flow as a function of distance from the process centre line or from the top surface of the workpiece. The post-process position of the tracer was studied by optical microscope.

In Chapter 6 results of particle image velocimetry (PIV) technique are presented. The technique allowed to visualize material flow and to measure strain rate during physical simulation of friction stir welding (FSW). The micro-spherical glass tracers in a transparent non-Newtonian material, both having almost similar densities, were used as experimental materials. The characteristics of material flow, in particular, flow velocity and strain rate were obtained by following the path of the tracer particles.

In Chapter 7, the friction stir welding process was numerically simulated to analyse 2D material flow and the results were verified with the results of particle image velocimetry measurements. The model quite accurately captured many real process characteristics such as velocity and strain rate, but it shows deformation zone slightly wider around the pin as compared to the experimental.

In Chapter 8, a brief summary of the outcomes from TIT, PIV and computational techniques on material flow, strain and strain rate during the FSW process and scope for future work is given.

CHAPTER 2

BACKGROUND LITERATURE

2.1 Introduction

The friction stir welding (FSW) is a solid-state welding technology, which was invented in 1991[1]. Right after its invention, it has attracted a considerable amount of research due to its advantageous features such as high-strength welds, small post-welding distortion and environmental-friendliness. Friction stir processing (FSP) is a derivative of FSW technique wherein the process is used for surface modification in a localized manner. However, both FSW and FSP are similar in terms of material flow behaviour.

The FSW technique is very simple and easy to implement [11]. It is a kind of severe plastic deformation process which involves deformation at high strain rates and elevated temperatures [12]. The process is performed by traversing a rotating tool through workpiece along a desired path as shown in Fig. 2.1. The FSW tool consists of a cylindrical shoulder and a concentric pin. The pin is forced into the workpiece whereas the shoulder is positioned at the surface of the workpiece. The shoulder generates heat due to friction and consolidates material that flows around the pin while pin stirs the material. The process is the combination of extrusion and forging of the material. High strain, strain rate and temperature experienced by the base metal during stirring cause grain refinement through dynamic recrystallization. Based on motions of the tool one can identify four sides around the tool; retreating side (RS), advancing side (AS), leading side (LS) and trailing side (TS), as shown in Fig. 2.1. At the retreating side of the tool, the tangential velocity of the rotating tool opposes its forward travel. At the advancing side, the tangential velocity of the tool is in the same direction as the tool traverse. The front and back sides of the tool are known as leading and trailing sides, respectively.

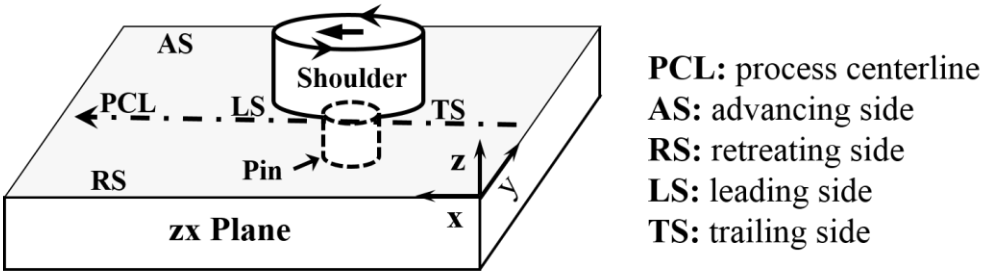

Fig. 2.1: Schematic of friction stir welding.

FSW give rise to microstructurally distinct zones along the workpiece thickness known as nugget zone (NZ), thermo-mechanical affected zone (TMAZ) and heat affected zone (HAZ) that can be seen across the cross-section of the processed workpiece as shown in Fig. 2.2.

The nugget zone during the FSW process experiences higher strain and maximum temperature resulting in fine grain equiaxed microstructure [13]. Usually, the NZ is basin shaped or elliptical in nature and its size is equal to the pin size or slightly greater than the pin size. TMAZ forms between NZ and HAZ. The deformed structure in the TMAZ indicates the effect of temperature and deformation experienced by this zone. Lower strains and temperatures are experienced by the material in this zone and it exhibits elongated and deformed grains. This zone is unable to show the recrystallization effect after plastic deformation due to insufficient strain and lower temperatures [14]. HAZ is the heat affected base metal (BM). The grain size in this zone is similar to the parent material. The grain refinement in the nugget zone improves the mechanical (tensile, fatigue and bending) and corrosion resistance properties of the weld. The extent of grain refinement depends on temperature, strain and strain rate. Strain and strain rate are dependent on material flow around the tool, hence a detailed understanding of material flow during FSW is imperative.

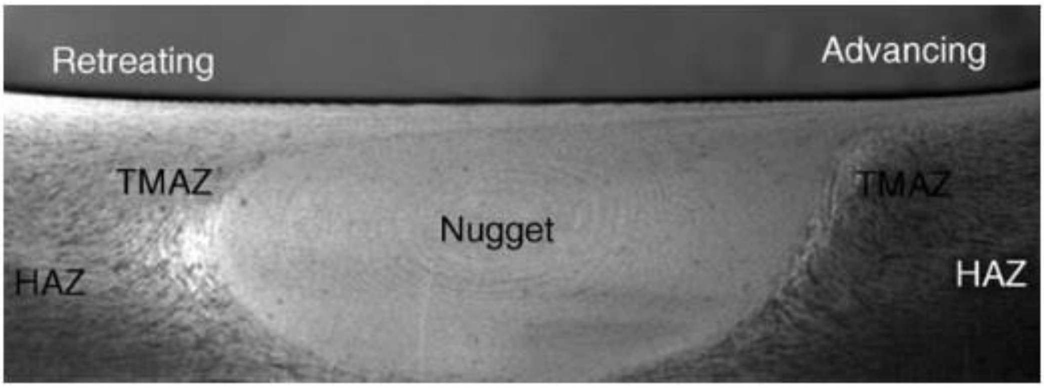

Fig. 2.2: A typical macrograph showing various microstructural zones in FSP 7075Al-T651 (standard threaded pin, 400 rpm and 51 mm/min) [5].

2.2 Temperature distribution

During the FSW process, the material softens and shows viscoplastic behaviour which depends on temperature attained in the nugget zone [15]. The maximum temperature never exceeds the melting point of the workpiece material [16, 17]. A large amount of heat is generated in and around NZ due to friction between the base material and shoulder/pin. The temperature measurement is usually carried out by inserting thermocouple at different locations in the material. The temperature distribution around the nugget zone is shown in Fig. 2.3 [14] with maximum a temperature of 475°C at the edge of the NZ. Tang et al. [16] placed thermocouple to measure temperature attained during the FSW of 6061Al-T6 and showed that the peak temperature is stable in the range of 425-450°C. However, the measurement of temperature by the thermocouple in the NZ is not possible due to stirring action. In order to get an estimate of temperature in the nugget zone researches took help of microstructural evolution in the NZ or computational methods. The microstructure evolution was studied in terms of grain size, grain boundary characteristics, coarsening and dissolution of precipitates.

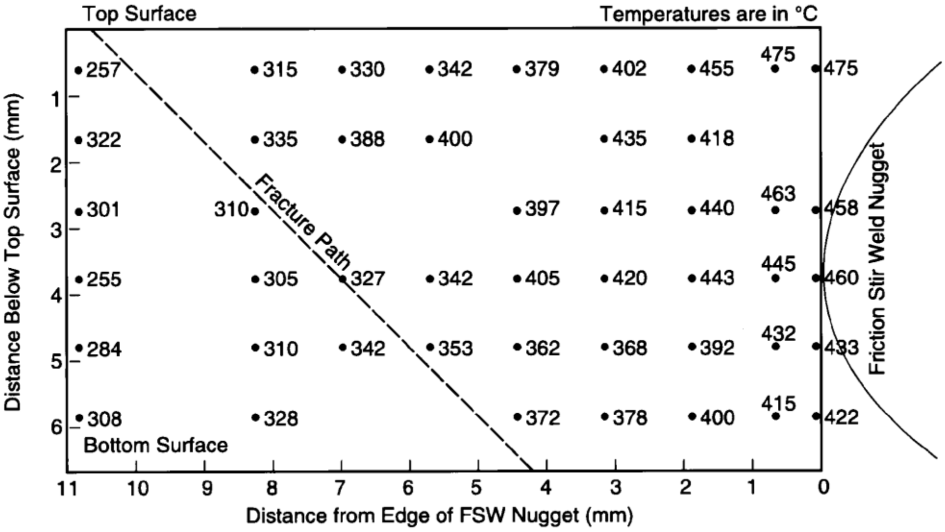

Fig. 2.3: Peak temperature distribution adjacent to a friction stir weld in Al 7075-T651 [14].

Maximum process temperatures of 400-480^{o}C were estimated from the precipitate dissolution kinetics during FSW of a 7075Al-T651 alloy [18]. In the case of the FSW of 6061 Al alloy few precipitates did not dissolve and the temperature was estimated to be 400^{o}C [19]. TEM study of the FSWed 6063 Al alloy [20] showed that the precipitates in the NZ were completely dissolved in the weld region up to a distance 8.5 mm from pin center. Heurtier et al. [21] estimated maximum temperatures of about 475^{o}C in the nugget zone, 425^{o}C in the TMAZ and 325^{o}C in the HAZ. In addition, it was found that the increase in rotational speed increased the peak temperature developed in the weld centerline. Increasing the ratio of tool rotation rate/traverse speed for material like 2024Al-T6, 5083Al-O and 7075Al-T6, increases the peak temperature of the weld zone. The increase in the pseudo-heat index which is the measure of rotation rate/traverse speed leads to a change in frictional condition from stick to stick/slip. In the FSW 6061Al-T6 welded joint, with the help of a regression analysis, it was proposed that the temperatures necessary for a good weld joint stand in the range of 365-390°C [15].

Maximum temperature developed in the nugget zone is a strong function of tool rotational speed N and heating rate depends on traverse speed V_T. For various aluminium alloys, a general relation for maximum welding temperature and FSW process parameters is given by the equation [22].

$$\frac{T}{T_m} = K\left(\frac{N^2}{V_T \times 10^4}\right)^{\alpha}. \tag{2.1}$$

The exponent α is in the range of 0.04-0.06, K is a constant 0.65-0.75 and T_m is the melting point of the aluminium alloy [22]. In general, the temperature generated in the stir zone is less than the melting point of the workpiece material and the tool shoulder dominates the heat generation.

2.3 Material flow

In order to get a defect free sound joint, understanding of the material flow, strains and strain rates achieved during FSW are important factors to understand [10, 23]. This has led to numerous investigations on material flow behaviour during FSW. A number of approaches, such as tracer insert technique, welding of dissimilar alloys/metals, have been used to visualize material flow pattern in FSW. In addition, some physical simulation and computational methods were also used to model the material flow.

2.3.1 Factors affecting material flow

Material flow during the FSW process depends on tool geometry (shape and size of shoulder and pin profile), processing parameters (rotational speed, traverse speed, tool tilt angle), contact load, i.e. axial force and material [24-27]. Optimizing these parameters the process will become defect free and evaluate the microstructure in the stir zone [26, 28]. The factors like tilt angle and axial force do not affect microstructure significantly but help in proper filling of the material in the cavity created by the moving tool.

2.3.1.1 Tool geometry

The tool geometry plays a critical role in material flow and in obtaining desirable microstructures in the weld and the TMAZ [29-33]. The FSW tool has two functions: (i) localized heating, to soften the material and (ii) material flow, to fill the cavity properly. The pin generates heat initially (during plunging) and the material surrounding the pin contributes some more heat due to deformation and finally when the shoulder come in contact of the workpiece surface, a large amount of heat is generated [30]. From the heating aspect, the relative size of the pin and shoulder is important compared to other design features. The other function of the tool is to stir the material and make the material to flow in the confined area.

In order to control the flow, heat generation and mixing of the material, different tool designs have been developed with different features in the tool pin (including threads, flutes, flats, whorls, flares and skew on cylindrical or cone frustum-shaped pins with rounded or flat bottom) and shoulder (including ridges, grooves, knurling and scrolls) [5].

(a) Shoulder

The tool shoulder generates frictional heat to soften the workpiece material, control the material flow and confine the hot material [34, 35]. The shoulder size decides the amount of heat generation. Also, it exerts downward forging action necessary for weld consolidation [36]. Other than size, the shape of the shoulder surface plays an important role. The shape can be planar, concave or convex [36-40]. The concave shoulder with tapered pin gives sound weld [36]. Galvao et al. [37] investigated the effect of various shoulder features as shown in Fig. 2.4, and noticed that the scrolled shoulder tool provides suitable material flow whereas the flat shoulder gives rise to defects. The scrolled shoulder generates more heat and results in finer grains and higher hardness in comparison to flat and concave shoulder profiles. Leal et al. [40] thoroughly investigated the effect of scrolled feature and observed that the dragging of material due to this feature helps in proper mixing.

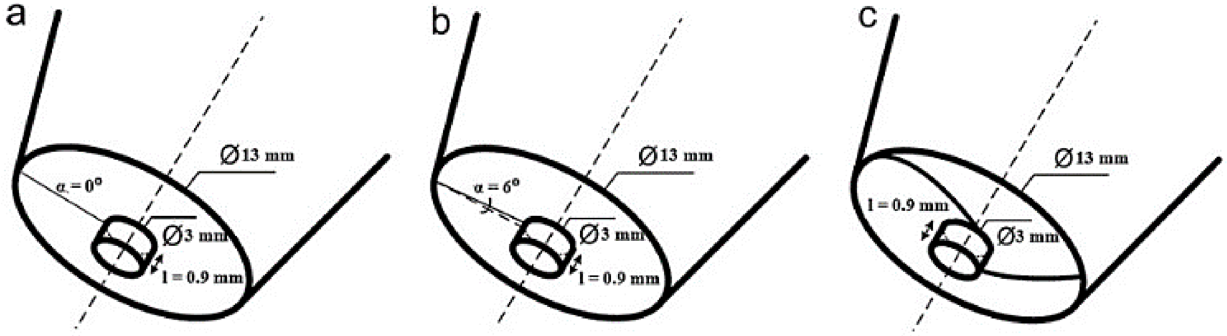

Fig. 2.4: Tool shoulder geometries, (a) flat, (b) conical concave and, (c) scrolled [37].

(b) Pin

Some authors have studied the effect of tool pin on the material flow and mechanical properties of the weld [41-48]. They found that the joints fabricated with the square tool pin profile achieved better properties compared to the other tool pins [41-43]. Buffa et al. [30] developed an effective methodology to optimally design welding tool and process parameters for FSW with increased nugget integrity. They observed the temperature and strain rate increases with the pin angle. Mugada et al. [49] addressed the effect of both shoulder and pin designs on material flow and weld quality. They used the ridge shoulder with different pin profiles as shown in Fig. 2.5. They observed, for a triangular tool more amount of material was sheared, plasticized and displaced from leading side to trailing side of the weld compared to other tools (square, pentagon, and hexagon). However, square pin profile results in better material flow, complete mixing and distribution of tracer material in the weld region, as shown in Fig. 2.6(c). The welds with triangular, pentagon and hexagon tools leave unmixed tracer material (represented in red colour arrows) in the weld region as shown in Fig. 2.6(b), (d) and (e) respectively.

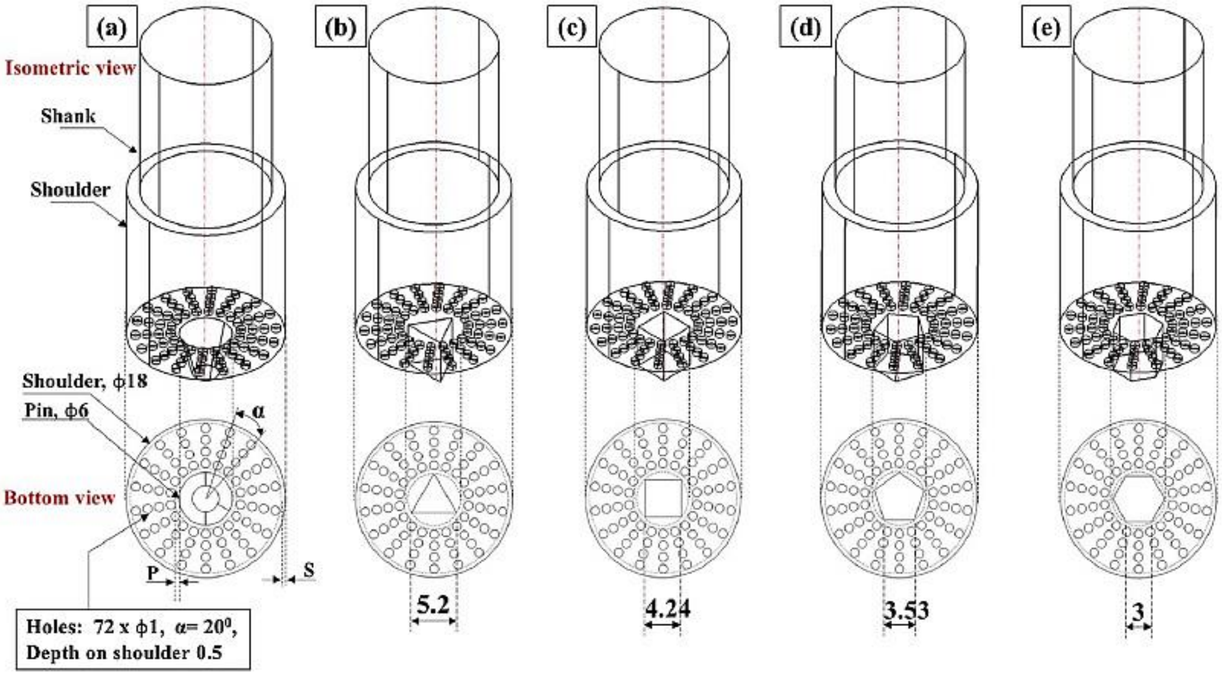

Fig. 2.5: Ridges shoulder with (a) Taper cylindrical, (b) Triangular, (c) Square, (d) Pentagon, and (e) Hexagon [49].

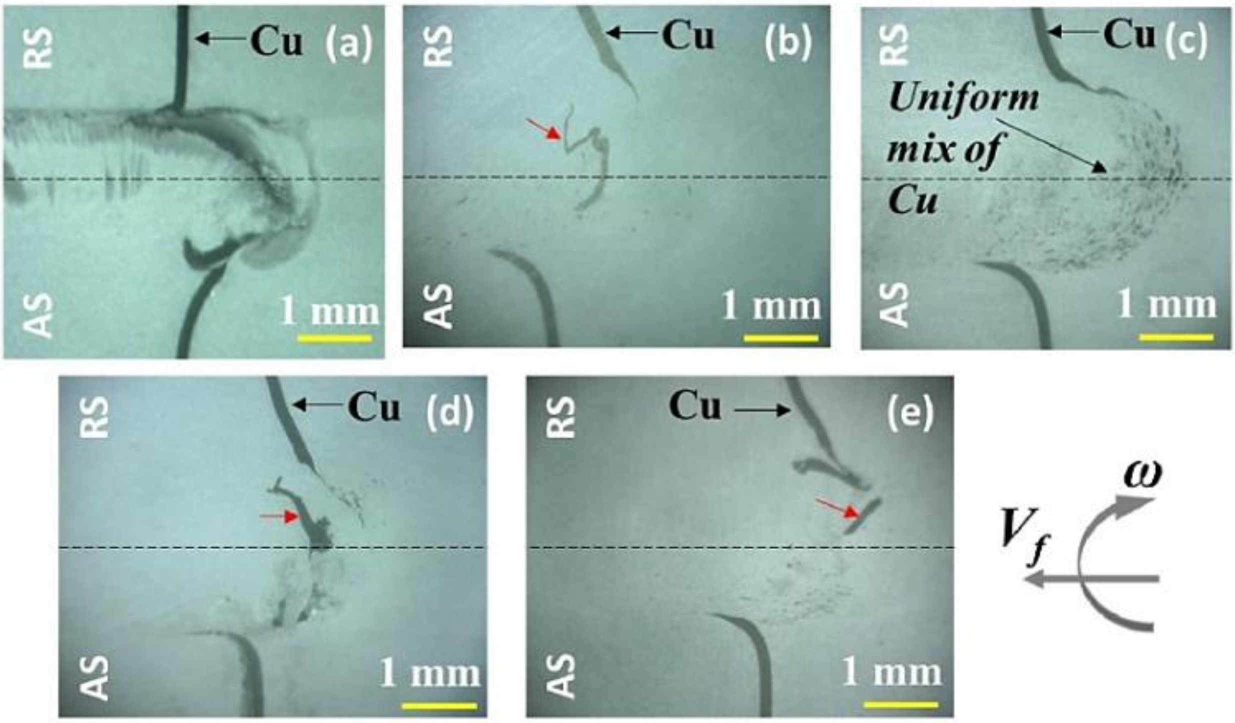

Fig. 2.6: Macrostructure at 3 mm from the top surface of plate at copper inserts location (perpendicular to weld configuration) for (a) Taper cylindrical, (b) Triangular, (c) Square, (d) Pentagon, and (e) Hexagon tool pin profiles [49].

2.3.1.2 Processing parameters

Processing parameters such as rotational speed, traverse speed and tool tilt angle decide the amount of heat generation, heat input and flow of the material during the process. Out of the above mentioned parameters, rotational speed is the dominant one to decide the material flow velocity, strain and strain rate [50-56], see Figs. 2.7 and 2.8.

Fig. 2.7 shows the effect of rotational speed on the material flow at a constant traverse speed i.e. 400 mm min^{-1} [50]. Material flow rate increased with an increase in the tool rotating speed up to 600 rpm and then decreased, and the maximum relative velocity was about 70% of the pin peripheral velocity. The material flow velocity does not increase monotonically with rpm due to change in the interface condition between tool pin surface and the material from sticking to slipping condition [57].

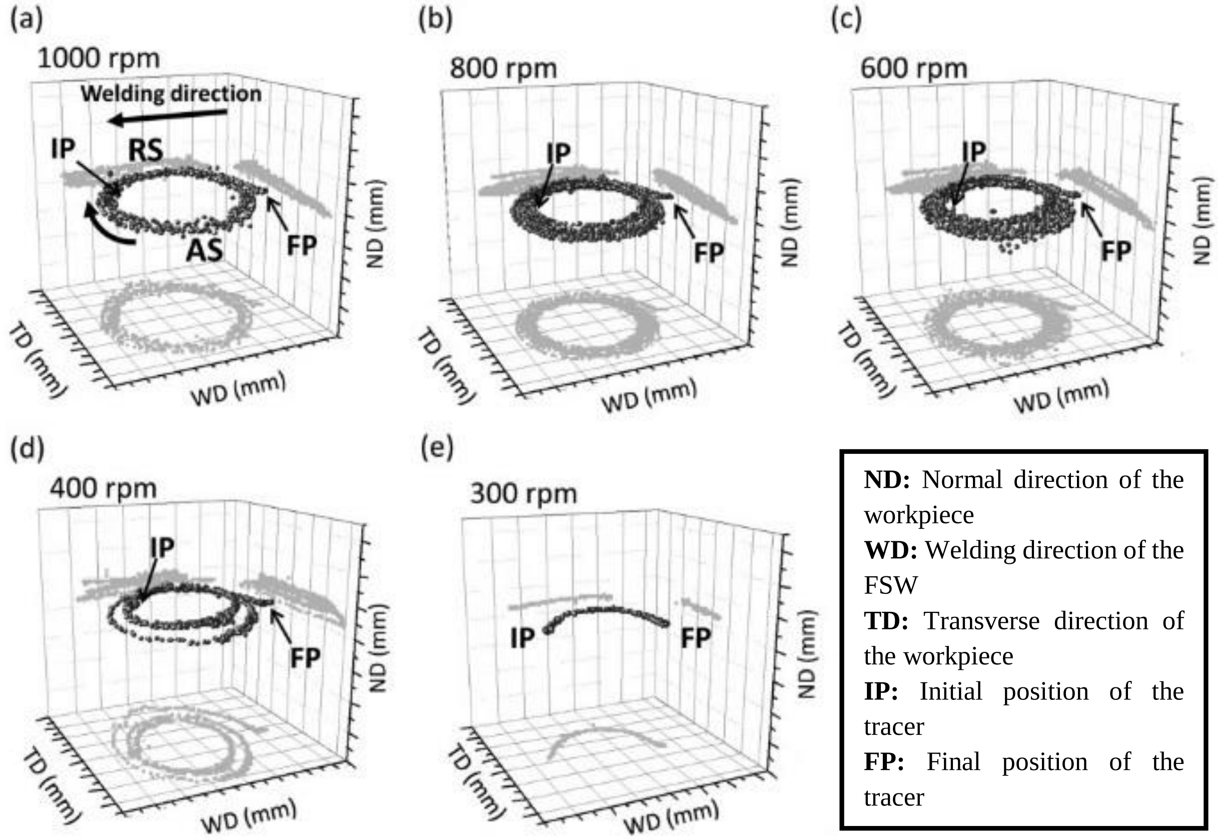

ND: Normal direction of the workpiece
WD: Welding direction of the FSW
TD: Transverse direction of the workpiece
IP: Initial position of the tracer
FP: Final position of the tracer

Fig. 2.7: Effect of rotational speed of the tool on material flow at 400 mm s^{-1} welding speed, a) 1000 rpm, b) 800 rpm, c) 600 rpm, d) 400 rpm and e) 300 rpm [50].

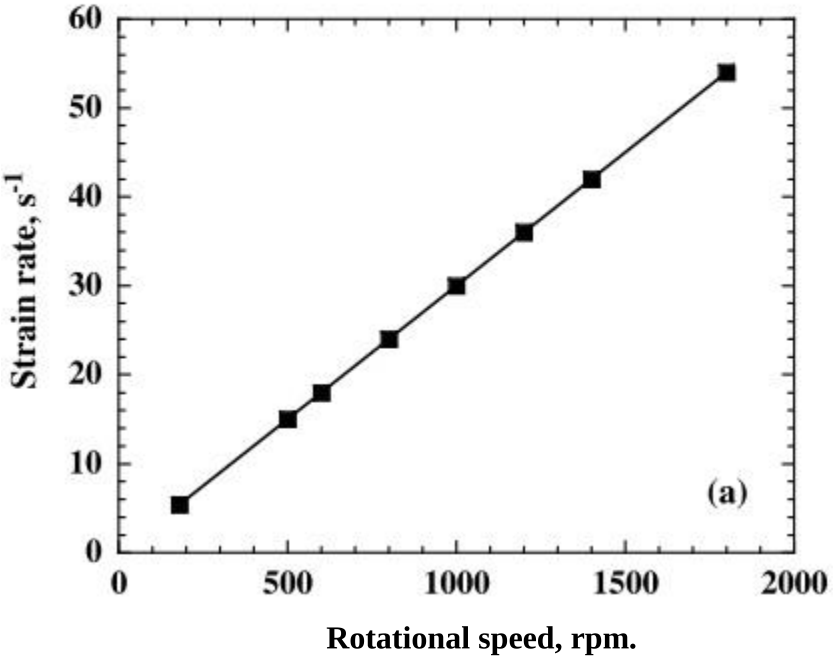

Fig. 2.8: Strain rate as a function of pin rotational speed [51].

In addition to the tool rotational and traverse speeds, another important process parameter is the tool tilt angle with respect to the workpiece surface. A suitable tilt angle of the spindle towards trailing direction ensures that the shoulder of the tool holds the stirred material by tool pin and move material efficiently from the front to the back and top to bottom of the pin. The tilt angle also enhances the temperature (as shown in Fig. 2.9), material fluidity and the compressive force in the rear side of the welding tool [28, 58, 59].

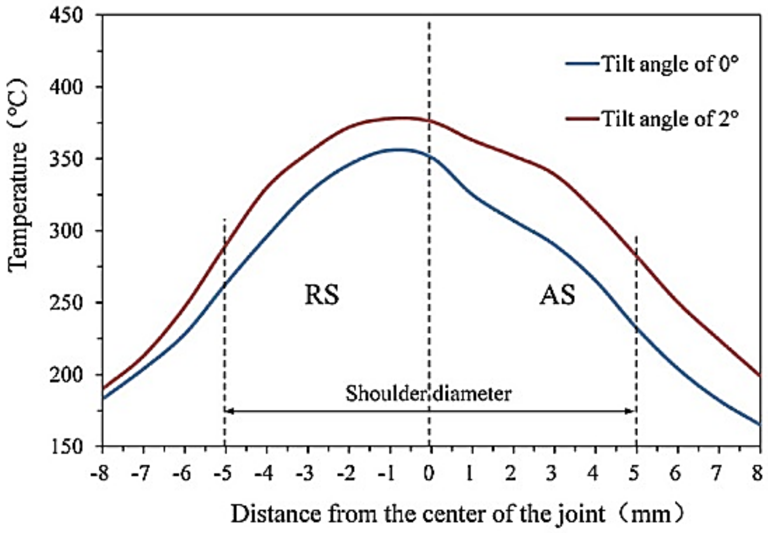

Fig. 2.9: Temperature distribution curves along the transverse section in the welds at the mid-thickness plane with different tilt angles [58].

2.3.1.3 Contact load

As the contact load increases the shoulder interaction with the workpiece is ensured. The increment in the contact load increased the fluidity of the material, due to frictional heat generation, so that the material fills in the cavity and make defect-free weld [60, 61]. From Fig. 2.10, it can be seen that the defect size is reduced as the contact load increases. Above a normal load of 7.4 kN (Fig. 2.10f), defects have disappeared. When the contact load is 7.4 kN, the transferred material from the leading side is confined in the weld cavity, and a sufficient amount of heat and hydrostatic pressure is generated to produce a defect-free weld.

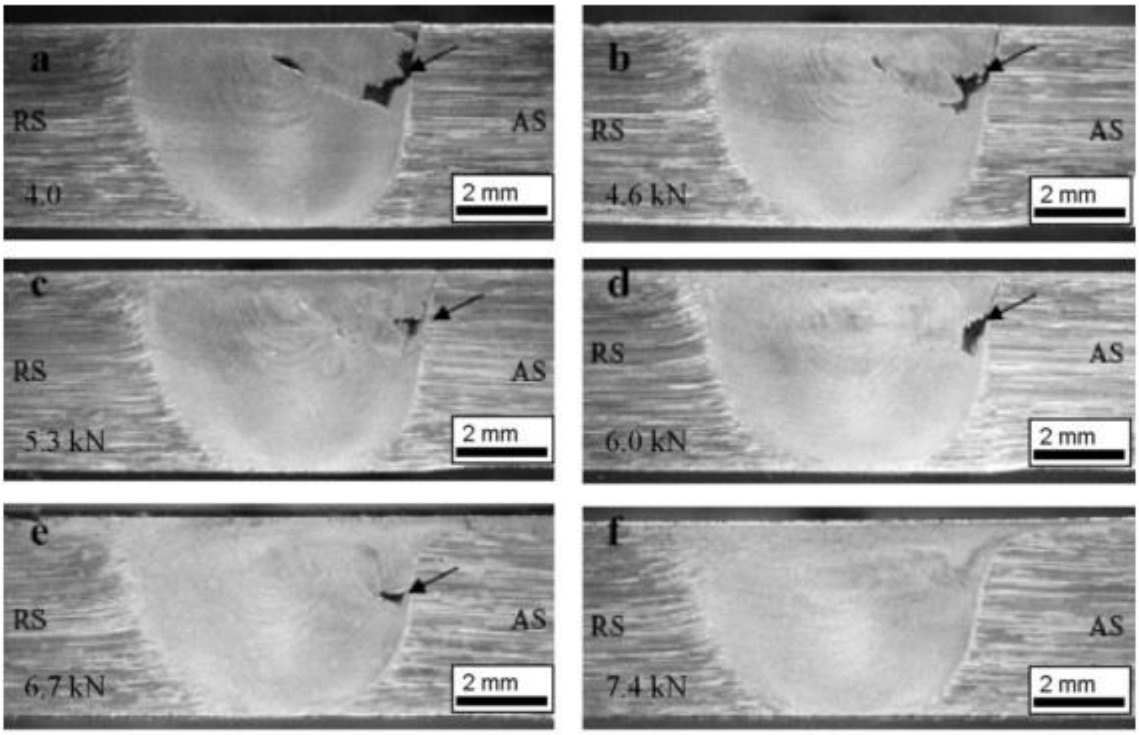

Fig. 2.10: Evaluation of defect free weld as a function of contact load. Arrow marks indicate the presence of voids in the weld [60].

2.3.1.4 Material

Fig. 2.11 shows the physical and thermo-mechanical (flow behaviour) properties of some materials. The figure shows the true stress-true strain curves of three aluminium alloys, AA2196. AA7150 and AA7085 respectively, at different temperatures and 0.01 s^{-1} strain rate [54, 105, 106]. In Figs. 2.11a, 2.11b and 2.11c, the peak stress of 2196, 7150 and 7085 aluminium alloys is 115 MPa, 100 MPa and 53 MPa respectively, at 350 °C and 0.01 s^{-1}. Since flow behaviour of materials is different as a function of temperature and strain rate, it is expected that material flow properties will also be different during FSW.

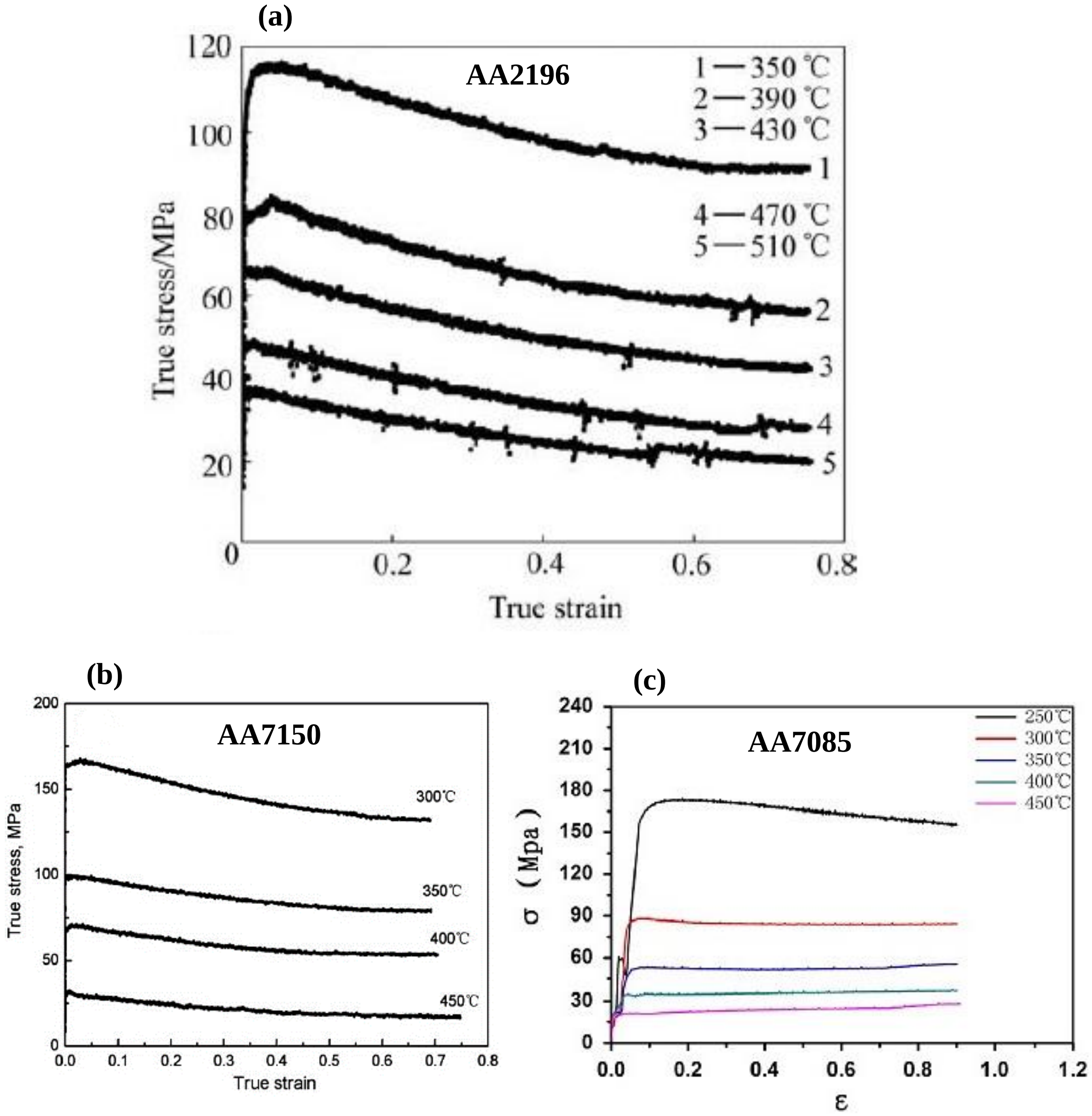

Fig. 2.11: True stress–true strain curves of: a) AA2196 [105], b) AA7150 [106] , and c) AA7085 [54], at strain rate 0.01s^{-1}, during hot compression.

2.4 Strain and strain rate

In addition to material flow behaviour, numerous efforts were made to determine the strain and strain rate during the FSW/P. Strain and strain rate values obtained by microstructural [51, 57, 32-67], tracer placement [65, 68, 69] and computational [30, 52, 53, 70-79] techniques in metallic and non-metallic materials are summarized in Table 2.1.

Table 2.1 Summary of the strain and strain rate values obtained using different techniques in the literature.

Techniques used		**Strain and strain rate**	**Materials and processing parameters**
Micro-structural	Chang et al. [51] developed a relationship for strain rate in the processed region by a linear assumption, the average material flow rate (R_m), is considered half of the pin rotational speed (R_p). The strain rate, during FSP, was derived by the torsion typed deformation as. $$\dot{\varepsilon} = \frac{R_m 2\pi r_e}{L_e}$$ where r_e and L_e are the effective (or average) radius and depth of the dynamically recrystallized zone.	5 – 50 s^{-1}	AZ31 Mg 180-1800 rpm, 90 mm min^{-1}
	Jata and Semiatin [62] estimated the strain rate, from measurements of shear strains versus position (of the sheared grains in the TMAZ), which were extrapolated to the weld zone.	10 s^{-1}	Al-Li-Cu alloy,
	Masaki et al. [63] attempted to simulate the recrystallized grains of the stir zone through a combination of the plane-strain compression at various strain rates and the subsequent cooling tracing the cooling cycle of the FSW. In plane-strain compression, the local equivalent plastic strain can be estimated as $$\varepsilon_{eq} = \frac{2}{\sqrt{3}} ln \frac{l_0}{l}$$	1.7-2.7 s^{-1}	1050 Al alloy 600-1200 rpm, 100 mm min^{-1}

	where l_0 and l are the initial intervals of pearlite bands before and after the deformation, respectively. The effective strain rate during the FSW was estimated using the grain size of the stir zone and this relationship.		
	Chen and Cui [64] observed dendritic features which are unaltered in a short distance (the width of a transitional zone) away from rotating sheared material (RSM). The deformed dendrites can be as a traced and thus an attempt has been made to determine the strain and strain rate of material in the transitional zone. $\varepsilon = ln\frac{\Delta l}{\Delta l_0} = ln\left(\frac{\sqrt{\Delta x^2 + \Delta y^2}}{\Delta y}\right)$ A horizontal line (X-axis) can be drawn to approximately represent zero deformation. A vertical line (Y-axis) can also be drawn pointing downward. $\dot{\varepsilon} = \frac{\Delta \varepsilon}{\Delta t}$ Δt calculated from the forward speed of the tool.	3.5 and 85 s^{-1}	A356 cast alloy 740 rpm, 170 mm min^{-1}
Tracer	Mukherjee and Ghosh [65] observed the deformation field around the tool pin by inserting a ductile foil of AA5457 in-between two plates of AA5083. They measured strain by observing the change in thickness of the foil in the process direction. $\varepsilon = ln\left(\frac{d_0}{d}\right)$ where d_0 and d are the un-deformed and deformed foil thickness.	4.6 and 87 s^{-1}	5083 Al alloy 1500 rpm, 50.8 mm min^{-1}
	Liechty and Webb [68] pressed the steel balls between two plasticine layers before the process and after process detects the position of steel balls by radiography. They calculate the strain and strain rate as follow. $Strain\ (\varepsilon) = \frac{\Delta s - \Delta s_0}{\Delta s_0}$ and	4.4 and 1.3 s^{-1}	Plasticine 250 rpm, 65 mm min^{-1}

	$Strain\ rate\ (\dot{\varepsilon}) = \frac{1}{\Delta t}\frac{\Delta s - \Delta s_u}{\Delta s_u}$ where Δt required time for the furthest upstream particle on a streamline to move to the next particle's location. Δs_0 is the initial spacing between the two particles (before process), Δs is the streamwise distance between a pair of adjacent particles after FSP, and Δs_u is the streamwise spacing between a neighbouring pair immediately upstream.		
	Morisada et al. [69] buried the tungsten ball in Al 1050 alloy in a drilled hole. During the process, the position of the tracer were recorded in two high-speed video cameras at a frame rate of 500 fps. They calculated the velocity of the tungsten tracer (V) directly by the change in the space coordinate in two plots simultaneously. $V = \frac{L}{T}$ where L is the distance between the two plots and T is the transit time from one plot to the other plot. The strain rate is calculated as. $\dot{\boldsymbol{\varepsilon}} = \frac{\boldsymbol{l_{n+1}} - \boldsymbol{l_n}}{\boldsymbol{l_n}} \Big/ \boldsymbol{t}$ where l_n is the distance between the two plots and t is the deformation time.	±13.4 s^{-1}	Al 1050 alloy 1000 rpm, 400 mm min^{-1}
Computational	Frigaard et al. [71] developed a numerical 3D heat flow model, based on the method of finite differences for investigation. By combining information about the sub-grain size with outputs from the heat flow model, an estimate of the mean strain rate within this region has been made via the Zener– Holloman equation.	(a) 1.6 - 10.3 s^{-1} (b) 1.7 - 17.3 s^{-1}	a) 6082 Al alloy b) 7108 Al alloy 1500 rpm, 300-720 mm min^{-1}
	Nandan et al. [72], [73], [74] reported results of a 3D material flow and heat transfer modelling results during the	a) 45 s^{-1}	a) AA6061

	FSW of AA6061, SS and MS. They calculated the temperature fields, cooling rates, plastic flow fields and the geometry of the thermos-mechanically affected zone (TMAZ), using spatially variable heat generation rates, non-Newtonian viscosity as a function of local strain rate and temperature, and temperature dependent thermal conductivity, specific heat and yield stress.	b) 35 s^{-1} c) 25 s^{-1}	344 rpm, 95 mm min^{-1} b) SS 300 rpm, 100 mm min^{-1} c) MS 450 rpm, 25 mm min^{-1}
	Malik et al. [75] performed Finite element simulations to justify experimental results of plasticine for different pin profiles. Following relations are used to compute stress-strain rate in deforming the material. $\dot{\varepsilon_{ij}} = \frac{3}{2}\frac{\dot{\bar{\varepsilon}}}{\bar{\sigma}}\sigma'_{ij}$ $\bar{\sigma} = \sqrt{\frac{2}{3}\sigma'_{ij}\sigma'_{ij}}$ and $\dot{\bar{\varepsilon}} = \sqrt{\frac{2}{3}\dot{\varepsilon_{ij}}\dot{\varepsilon_{ij}}}$ where $\bar{\sigma}$, $\dot{\bar{\varepsilon}}$, $\dot{\varepsilon_{ij}}$ and σ'_{ij} are effective stress, effective strain rate, strain rate components and deviatoric stress components respectively.	20-90 and 6-12 s^{-1}	Plasticine
	Buffa et al. [52] proposed a continuum based FE model for FSW, that is 3D Lagrangian implicit, coupled, rigid-viscoplastic. This model is calibrated by comparing with experimental results of force and temperature distribution, then is used to investigate the distribution of temperature and strain in HAZ and NZ.	3-6	AA7075 1000 rpm, 50-200 mm min^{-1}
	In another work, Buffa et al. [30] developed for the FSW based on thermo-mechanically coupled rigid-visco-plastic 3D FEM, and analysis is performed to predict the process variables, as well as material flow pattern in the welded joints at varying pin angles and welding speeds.	4-9 and 4.5-7.3 s^{-1}	AA7075 1000 rpm, 50-200 mm min^{-1}
	Long et al. [76], used in the FSW simulation work is a steady state, Eulerian, CFD model. The solid state FSW	5-10 and	5083-O, 2219-T87

	process is treated as a visco-plastic laminar flow past a rotating cylinder. The accumulated effective strain can then be defined as $\varepsilon = ln\left(\frac{l}{APR}\right) + \left\|ln\left(\frac{l}{APR}\right)\right\|$ and $l = 2rcos^{-1}\left(\frac{r-x}{r}\right)$ where *l* is the maximum deformed length, r is the pin radius and x distance between the streamlines.	20-350 s^{-1}	and 7050-T751 54-844 rpm, 75 mm min^{-1}
	Arora et al. [77] used a visco-plastic flow and heat transfer model to predict the temperature and material flow fields during the FSW of AA2524 in three dimensions using the material properties and experimental conditions reported in the literature [80]. The strain rate is computed from the local velocity gradients. $\dot{\varepsilon_{ij}} = \frac{1}{2}\left(\frac{\partial u_i}{\partial x_j} + \frac{\partial u_j}{\partial x_i}\right)$ where ε_{ij} is the strain rate tensor and $\partial u_i/\partial x_j$ is the velocity gradient. The strain is computed next by integrating the strain rate tensor with time along with a streamline. $\varepsilon_{ij} = \int_0^t \dot{\varepsilon_{ij}}\, dt.$ where ε_{ij} is the strain tensor, and *dt* is the time step for integration.	-10 to 5 and -9 to 9 s^{-1}	AA2524 300 rpm, 126 mm min^{-1}
	Chen et al. [78] investigated both the total amount and the distribution of the heat flux by a fully coupled thermal–mechanical model based on CFD. They improved the constitutive equations in order to predict the flow stress at high temperatures more accurately. Based on the improved constitutive model, the heat generation, material flow pattern and the temperature distribution are simulated.	215-464 s^{-1}	6061 Al alloy 920 rpm, 20 mm min^{-1}

	Ammouri et al. [53] used experimentally verified finite element model to estimate the strain rate and the temperature values which were, consequently, used in calculating the Zener–Holloman parameter, Z-parameter.	25-125 s^{-1}	AZ31B cast alloy 600-2000 rpm, 75-900 mm min^{-1}
	Chen et al. [79], in their study, 3-D numerical simulation is conducted to analyse the heat transfer and plastic deformation behaviours during the FSW. For comparison purposes, both the boundary velocity (BV) and the boundary shear stress (BSS) models are employed in order to assess their performances in predicting the temperature and material deformation in the FSW.	10^2-10^3 s^{-1}	2024-T4 Al alloy 500-1600 rpm, 40 mm min^{-1}

It is evident from these studies that wide variation in strain and strain rate was reported. Variation in strain (3-90) and strain rate (1.3-1000 s^{-1}) values could be due to different techniques, processing parameters, slipping/sticking, processing materials and boundary conditions used.

2.5 Investigation techniques

In literature, generally, two types of technique were adopted for material flow investigation in the FSW process. One is tracer insert technique in metallic or non-metallic materials and another one is a computational method.

2.5.1 Tracer insert technique

In tracer insert technique a tracer of a different material than that of the matrix material is buried or inserted in metallic/non-metallic workpiece before the process. After/during the process, the position of the tracer is detected by different techniques. The change in the tracer position provides information about flow characteristics during the process.

2.5.1.1 Post-process flow visualization

The position of the tracer is detected after the process and the material flow pattern is analysed on the basis of the tracer position. The tracer material is generally different than the matrix material for easy detection.

(a) In metallic material

The material flow behaviour during FSW/P were performed using tracer of dissimilar metals [5, 81-86] and similar metals [60, 65, 87-91] of different composition. It is reported that a thin rotating region was observed around the tool pin of decreasing width from root to tip of the pin. The material inside the rotating region experiences the highest degree of mixing and complex vertical flow, see Figs. 2.12 and 2.13. The material in the rotating region was deposited towards the advancing side, at the back of the pin. The material is pushed downward on the advancing side and retreating side material moved upward toward the top within the pin diameter, see Figs. 2.14 and 2.15.

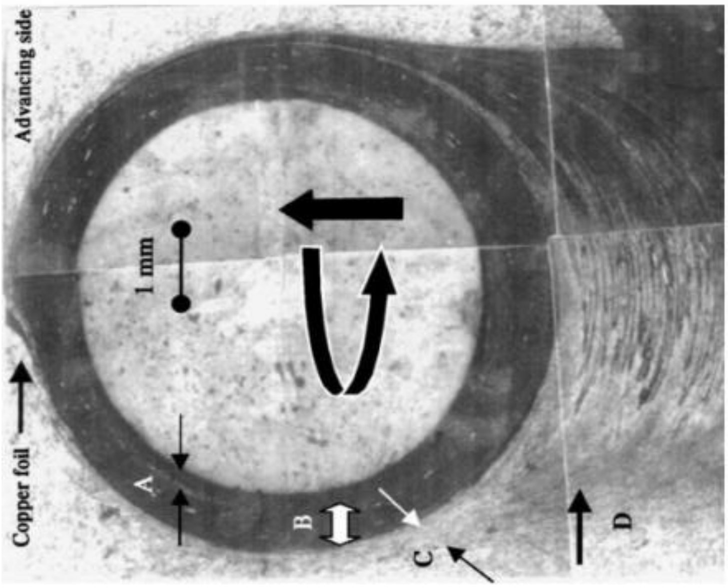

Fig. 2.12: Plan view at mid thickness of weld with a frozen nib. A copper foil marker was on the faying surface of the Al 6061 and is seen at the top. (A) Gap without material. (B) Rotational zone or that rotates with the nib. (C) Transitional zone of material that is entrained by the rotating pin. Small bright particles in B are tracer particles from the copper foil [82].

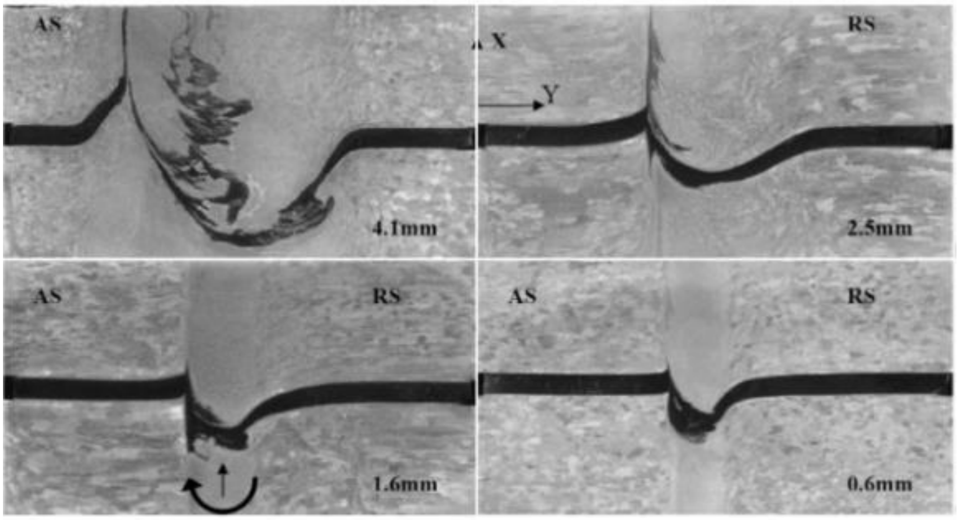

Fig. 2.13: Material flow investigation at different depth (measured from tool pin tip) in 7020 Al base material by inserting Al 2024 tracer [89].

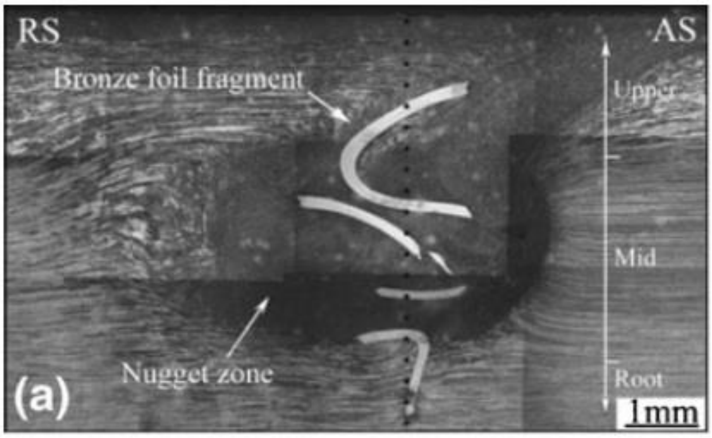

Fig. 2.14: Distribution morphologies of bronze foil in the weld nugget [84].

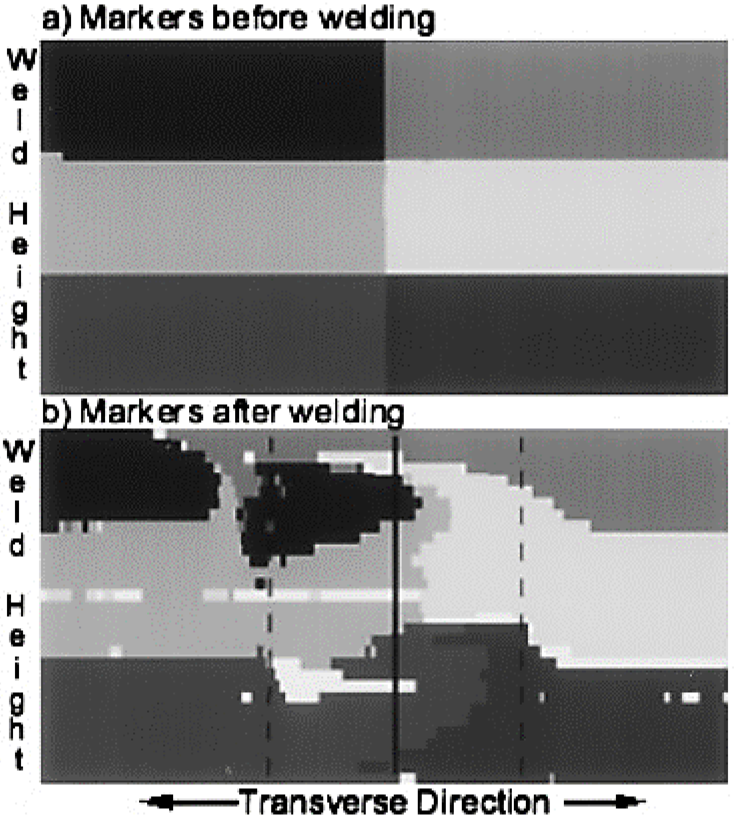

Fig. 2.15: Vertical mixing in weld. The markers are projected in the vertical plane viewing in the welding direction. (a) The un-deformed markers before welding and (b) the vertically mixed six markers after welding. The solid and the dashed lines denote the centerline and pin diameter, respectively [87].

Huang et al. [7] investigate the material flow behaviour by TIT, especially how material deposited on the trailing side of the rotating tool, which influences the joint formation. Schmidt et al. [83] observed a cyclic deposition of copper tracer material in aluminium welds, which is attributed to a slipping/sticking condition. They have estimated the material velocity just outside the rotating region at 10-30% of the tool's rotational speed. Gerlich et al. [57, 66] have demonstrated that the sticking/slipping boundary condition is dependent on the workpiece material. Additionally, Kim et al. [92] showed that downward force contributes greatly to the formation of voids and other defects.

(b) In simulated material

Most of the studies, explained the flow behaviour of metal during the FSW process as visco-plastic in nature [17, 81, 93-96]. Hence, a few researchers used modelling materials, which have similar visco-plastic behaviour and strain rate sensitivity parameter, during FSW [68, 75, 78, 97]. Liechty and Webb [68, 97] used plasticine as an experimental material and small steel balls as the tracer. They pressed steel balls of 1 mm diameter between two layers of plasticine as shown in Fig. 2.16. The X-ray images of steel balls were acquired after processing, see Fig. 2.17 i. The spacing between balls before and after processing was used to calculate velocities, strains, and strain rates along streamlines. In another experiment, they used plasticine layers of different colour to aid in flow visualization. The motion of material was observed by inserting contrasting colour plasticine as markers into the workpiece (Fig. 2.17 ii). Although plasticine has the potential for material flow visualization in FSW process, but the technique may fail if material rotates more than once around the pin and the second drawback is entrapment of plasticine in the threads of the tool pin.

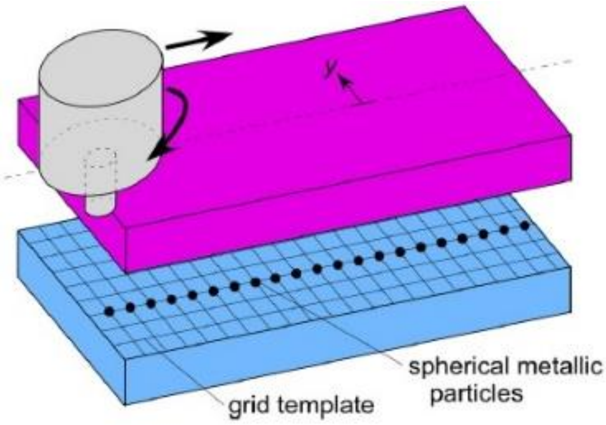

Fig. 2.16: Particle and grid setup sketch [68].

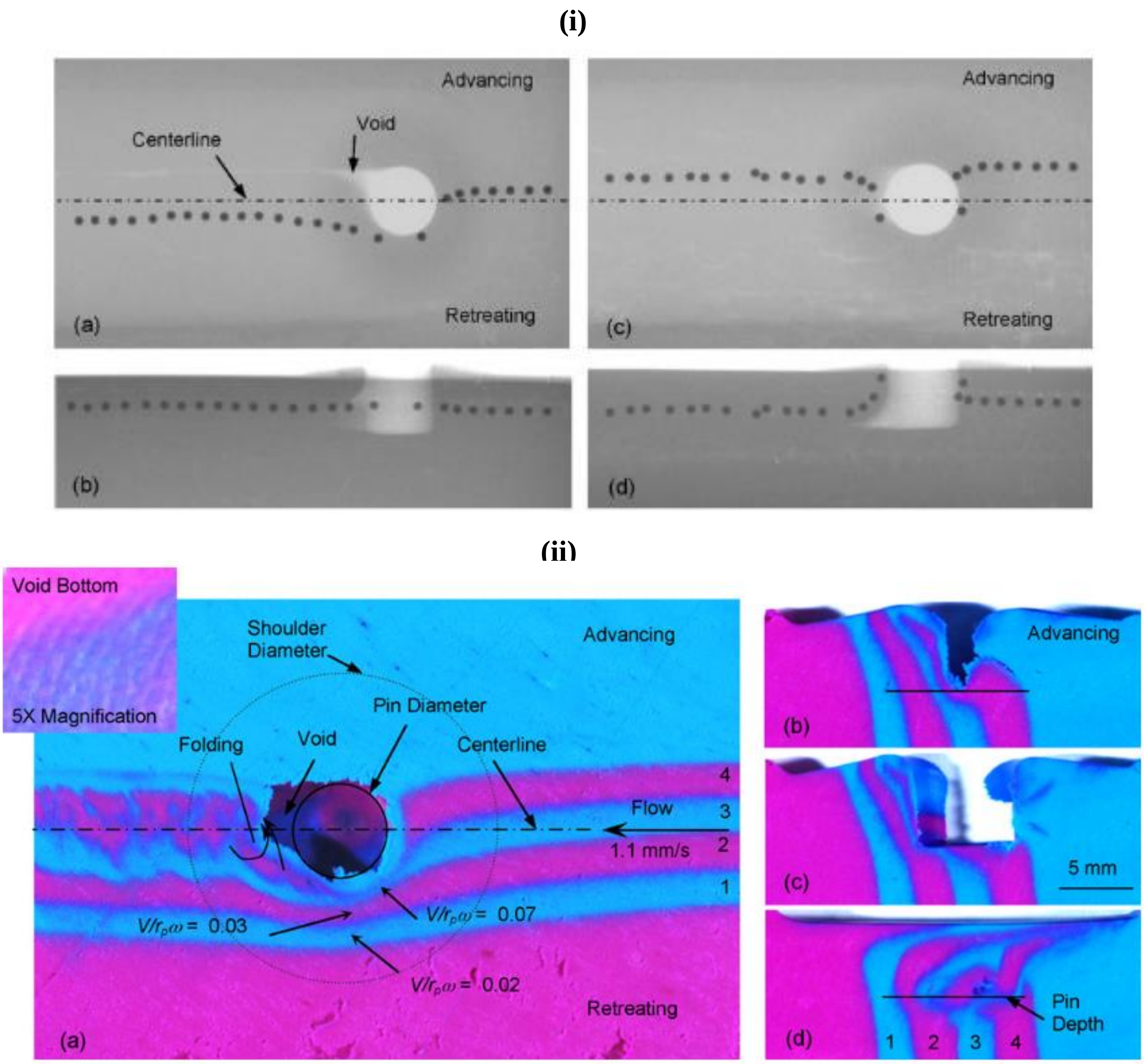

Fig. 2.17: Tracer flow in plasticine, i) Steel particle radiograph plan (x–y plane) and longitudinal views (x–z plane). Initial particle line located at (a), (b) y/r_P =0.37 and (c), (d) y/r_P = 0.90, and ii) Streamline marker (coloured plasticine layers) flow visualization (a) plan section (x–y plane) at the approximate mid-pin depth, (b) transverse section (y–z plane) at the pin leading edge, (c) transverse section through the pin center, and (d) transverse section downstream of the pin [68].

2.5.1.2 In-situ flow visualization

The position of the tracer is detected during the process and on the basis of tracer flow, material flow pattern was analysed. The tracer particle movement was recorded by high speed cameras during the process. Velocities, strains and strain rates were calculated by using the positions of the tracer during the FSW process.

(a) In metallic material

Morisada et al. [50, 69, 98] buried tungsten balls in Al 1050 alloy workpiece and detect the positions of the tracer by using X-ray transmission real-time imaging systems as shown in Fig. 2.18. Use of radiography enabled tracking of the tracer during the process. They showed a rotational zone of uniform width around the pin. The tracer rotates multiple times around the pin before leaving the rotational zone. Furthermore, they obtained strain and strain rate directly from the change in the material flow velocity obtained by three-dimensional visualization of the material flow, shown in Fig. 2.19.

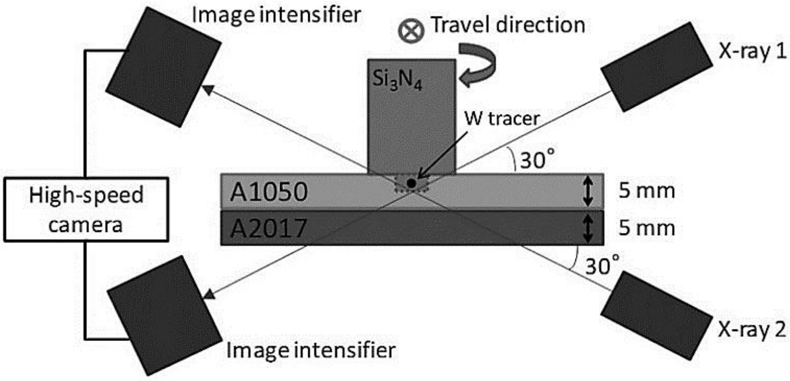

Fig. 2.18: A schematic drawing of the experimental set-up for the X-ray radiography during FSW [50].

Fig. 2.19 shows a three-dimensional graph and various two-dimensional graphs obtained using the coordinates of the tungsten tracer. WD, TD and ND show the welding direction of the FSW, the transverse direction of the A1050 plate, and the normal direction of the A1050 plate, respectively. The material flow around the probe was essentially similar to that reported in previous studies [82, 83, 99]. The flow zone of 2 mm width around the pin could be confirmed on the WD–TD graph. This result implied that the assumption, the material flow was based on the final position of the tracer was not entirely accurate.

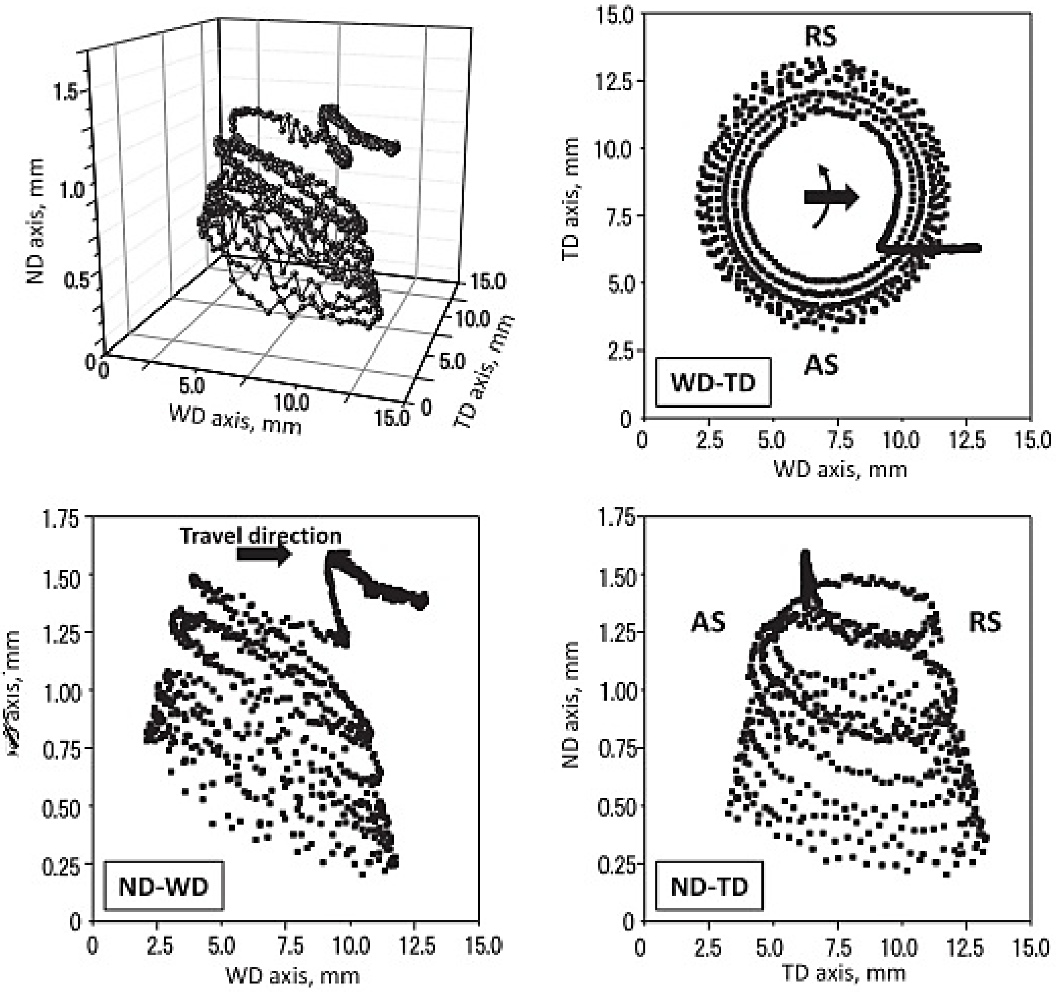

Fig. 2.19: A three-dimensional graph and various two-dimensional graphs obtained using the coordinates of the tungsten tracer [50].

In another experiment [98], they observed that the tungsten tracer gradually moved to the outer side of the stir zone due to centrifugal force. Its velocity near the pin was lower than the peripheral velocity of the pin but on the outer side was higher, as shown in Fig. 2.20.

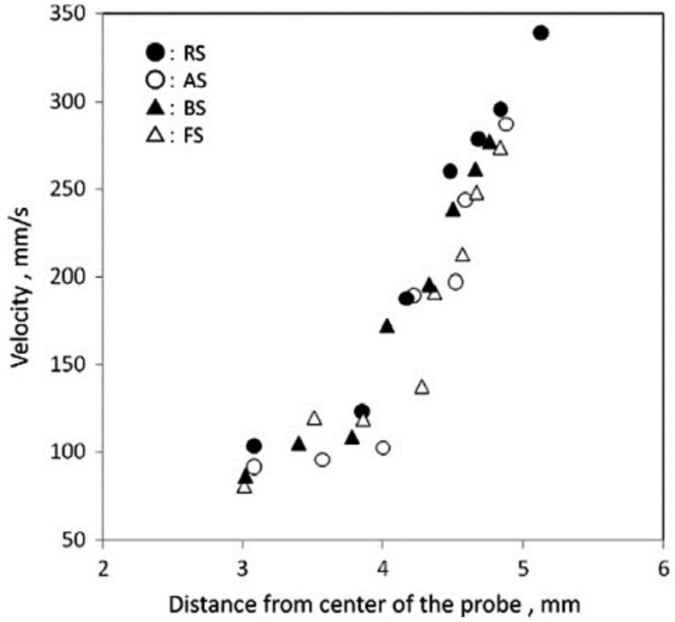

Fig. 2.20: Velocity of tungsten tracer at 1000 rpm and 400 mm min^{-1} [98].

(b) In simulated material

For in-situ flow visualization, physical modelling of the FSW process using transparent polyvinyl chloride (PVC) material has been attempted [100]. In PVC, the material flow direction during welding was investigated using a high speed video camera. Additionally, the material flow velocity was measured by particle image velocimetry method. In PVC, the material flow velocity ranges from 2 to 20 mm s^{-1} at AS and 1 to 5 mm s^{-1} at RS but, in general, the RS material flow velocity is greater than the AS [98, 101]. The second attempt for in-situ flow visualization done by Nowak et al. [102] using a high speed video camera in transparent polycarbonate material. Polycarbonate offers the potential for visualization of material flow during FSW. Some of the general flow characteristics in aluminium were also observed in the polycarbonate weld. However, welding of the polycarbonate with a threaded tool could not be achieved because the threads got clogged with the polymer. Further, it must be acknowledged that the thermo-mechanical properties of polycarbonate are inherently different from metals, and thus, its weld characteristics will depart fundamentally from that expected in FSW of metals.

Comment on tracer material

Table 2.2 shows the physical properties of the tracer and matrix materials used in the various investigations of material flow during the FSW process. The physical (melting point, density and thermal conductivity) and thermo-mechanical (flow stress) properties of tracer material were quite different than that of the workpiece material. The flow stress is the function of temperature, strain, strain rate and material, hence different metals and compositions show different flow behaviour [103-107].

Table 2.2 Physical properties of the tracer and matrix materials used in the investigation of the material flow during the FSW process [108].

Material Tracer/Matrix	Physical properties of the tracer-matrix materials			Refs.
	Melting point (T_m, K) Tracer/Matrix	Density (ρ, kg m^{-3}) Tracer/Matrix	Thermal conductivity (K_t, W/(m·K) Tracer/Matrix	
Cu/Al 6061	1353/923	8940/2700	390/180	[82]
Cu/Al 2024	1353/911	8940/2780	390/121	[83]
Cu/Al 7020	1353/896	8940/2800	390/130	[85]
Cu/Al 6082	1353/923	8940/2700	390/170	[7], [49]
Steel/(Al 6061 and Al 7075)	1773/(923 and 896)	7800/(2700 and 2830)	26/(167 and 130)	[81]
W/Al 1050	3695/928	19320/2705	166/210	[69]
Steel/plasticine	1773/338	7800/1570	26/0.65	[97]
Bronze/Al 7075	1223/896	8700/2830	293/130	[84]
Al 2195/Al 5454	911/918	2800/2690	116/134	[87]
Al 5083/Al 5457	911/928	2660/2690	117/176	[65]
Al 7020/Al 2024	896/911	2800/2780	130/116	[89]

In general, the melting point of tracers used for flow investigation is very high than that of the workpiece material (see Table 2.2). Therefore, it is expected that the two-phase flow field may exist, which will affect the path followed by the tracer material vis-à-vis matrix material. Tracer density is another physical property that affects the material flow. The tracer material being heavier than the matrix material, it has a tendency to flow in a downward direction due to gravity effect and outward due to centrifugal force [50, 98]. Due to the complex dependence of the flow characteristics of material on physical and thermo-mechanical properties, an understanding of material flow by using different tracer material is expected to be challenging [10]. Numerical investigations have also been performed to explore the material flow behaviour and to overcome the challenges faced by the tracer insert techniques.

2.5.2 Numerical simulation

As discussed in the previous section, the experimental measurement of flow velocity, strain and strain rate during FSW in metal or simulated material is very difficult. The numerical methods may offer better understanding by quantifying strain and strain rate under suitable approximations.

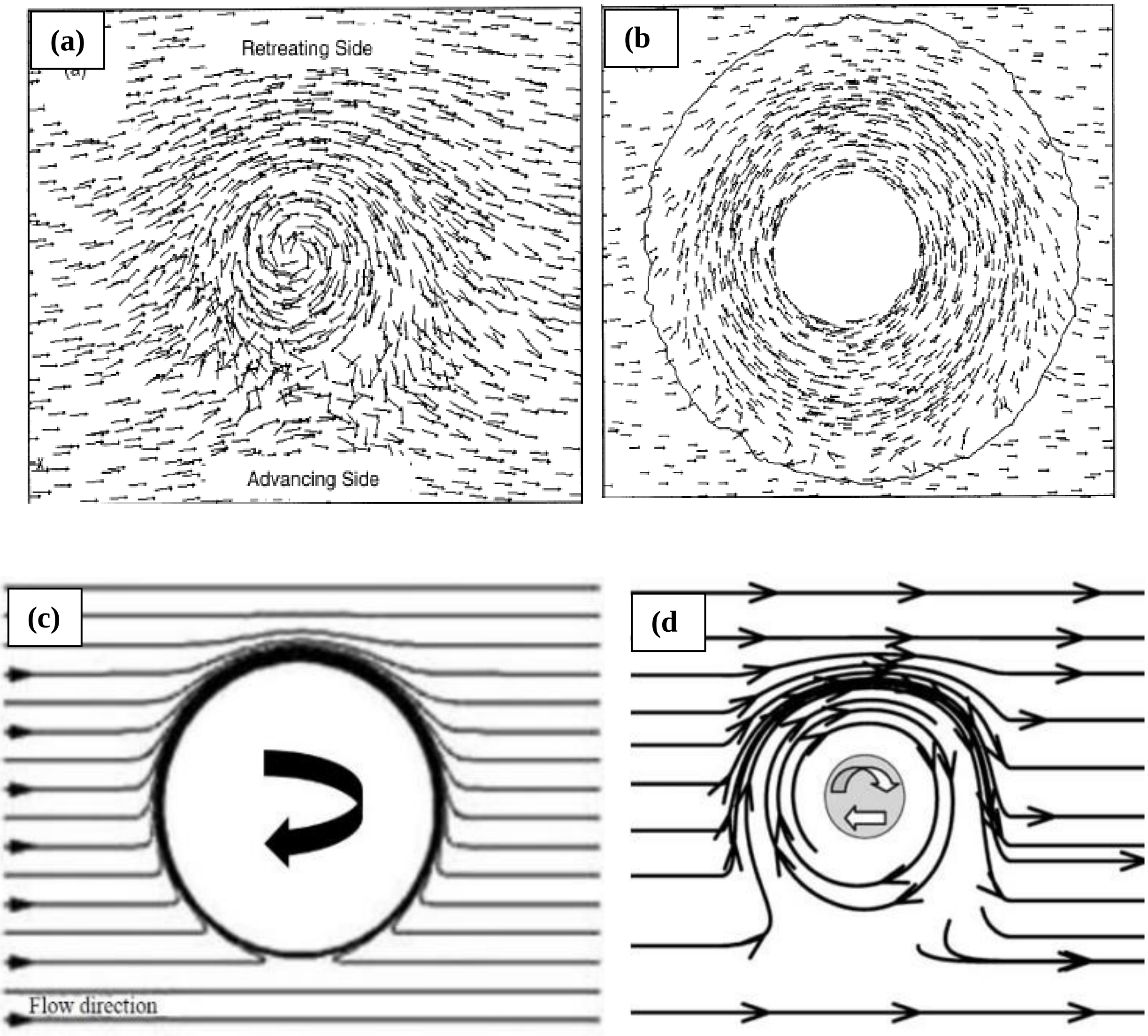

Fig. 2.21: Material flow behavior, a) at the bottom surface of the pin [110], b) at mid-length [110], c) streamlines of material flow[93], and d) streamline of material flow [72].

Computational fluid dynamics (CFD) is one of the most widely applied approaches in the numerical simulation of the FSW process. Reported literature comprises heat generation due to friction, heat transfer from tool to material, temperature distribution in material and plastic flow during welding in metal [31, 35, 72, 78, 93, 110-118] and simulated material [119]. These models have predicted that the material in line with the deformation zone was swept around the retreating side of the pin, as shown in Fig. 2.21. The amount of material swept around the pin increased at locations closer to the shoulder [72]. However, the size of the deformation zone was much larger than that observed experimentally [110].

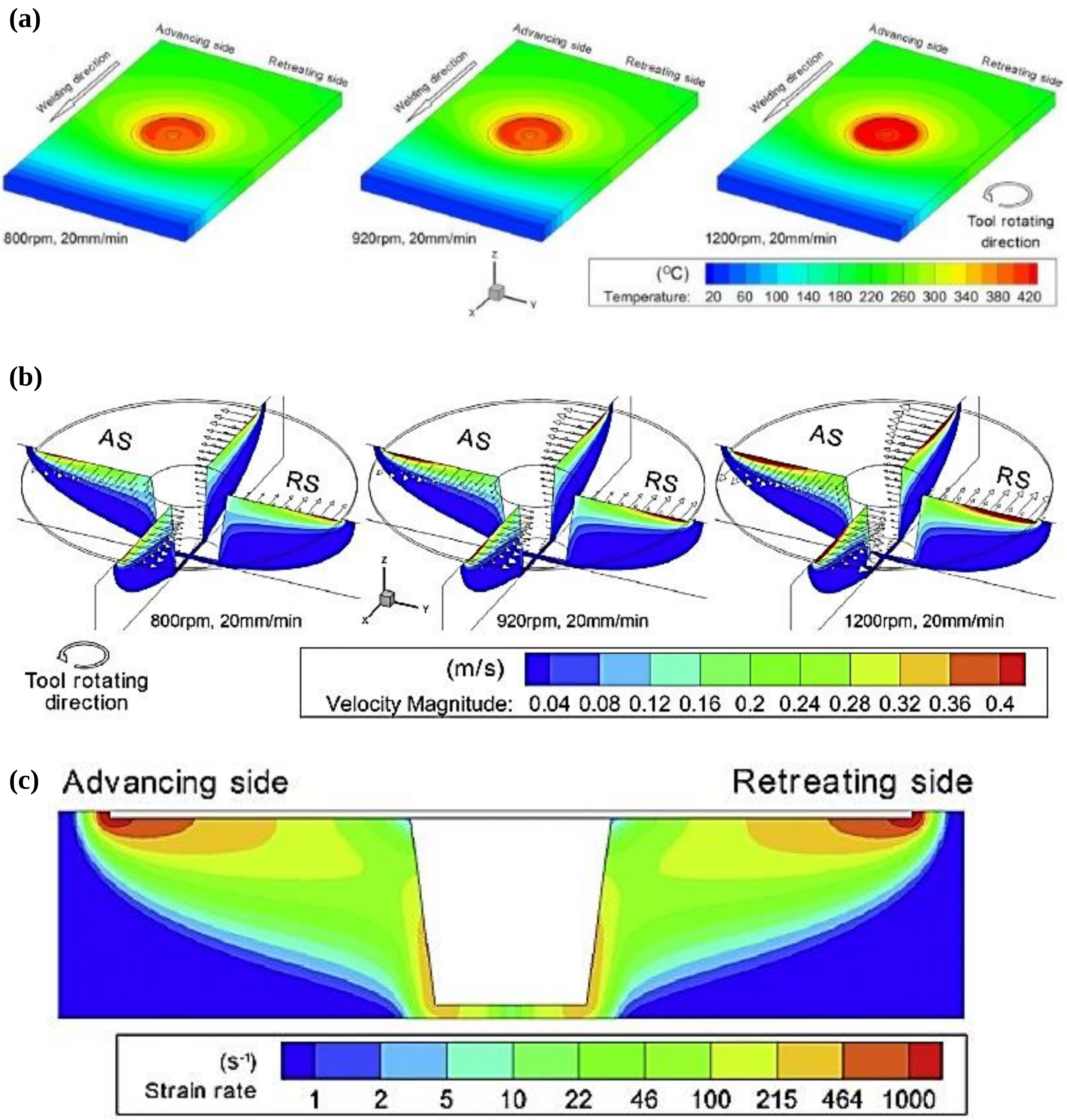

Fig. 2.22: a) Temperature field, b) velocity field and c) strain rate field, around the tool [78].

Recently, CFD simulation is applied successfully in the study of spatial distribution of heat generation flux [78, 112] and the effect of tool profile on the material flow [31, 113, 114]. Heat generation, temperature field, material flow pattern and strain rate were reported, as shown in Fig. 2.22.

Maximum values of the temperature, material flow velocity and strain rate were obtained near the shoulder edge. In the CFD based simulation for FSW, one of the critical issues is the frictional boundary condition between the welding tool and the workpiece [35, 117].

The frictional boundary condition at the tool/workpiece interface can be imposed either as velocity-based or shear stress-based boundary condition. In various studies [78, 79, 110, 114], the sticking contact state was employed via a velocity- based boundary condition, in which the material was assumed to flow at the same velocity as the welding tool at the tool/workpiece interface. Both, the maximum temperature and the deformation zone size were over-predicted using the sticking condition [110]. Others [72-74, 116, 120] have assumed a certain extent of slip between the shoulder and the workpiece in their simulation, and the simulated results are consistent with the experimental data [72-74]. Qian et al. [115] showed the transition between the sliding and sticking could occur at least at certain welding condition. The variation of the contact state over the tool/workpiece interface, as well as its effect on the heat generation and material flow pattern, are discussed by considering the transition between the sliding and sticking states at the tool/workpiece [121], see Fig. 2.23. On the other hand, the shear stress-based boundary condition proved to be closer to reality than the velocity-based boundary condition in the CFD simulation of FSW [122] [79]. In the shear stress- based boundary condition, the

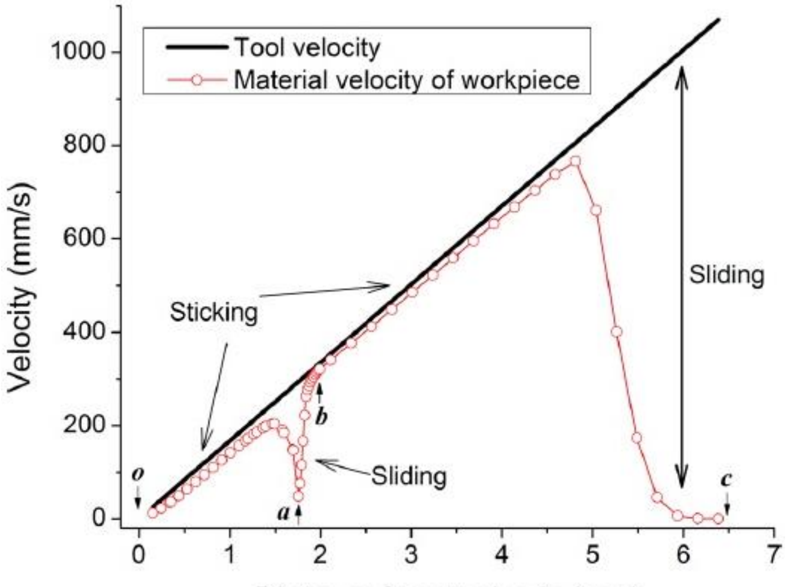

Fig. 2.23: Velocity profile at tool/workpiece interface [121].

interfacial material velocity is calculated based on the balance of interfacial shear stresses, instead of predetermining the interfacial velocity profile. Therefore, the contact condition between the tool and the workpiece is important to understand the FSW process and to build a good model. However, there is no generic method for the quantitative description of the interfacial contact state for various welding parameters, tool geometries, and materials [123].

While the CFD investigation of material flow visualization of FSW process is promising approach due to the possibility of observation points closer to the tool surface, which is not possible with tracer insert techniques, accurate implementation of boundary condition is a critical issue. The literature on flow visualization further suggests another possibility, i.e., particle image velocimetry (PIV) technique, besides tracer insert and computational techniques. While this approach has not been applied for an understanding of material flow during the FSW process, it seems to be the reliable approach widely used in the determination of in-situ flow behaviour [124-132]. It is also expected that the drawbacks noted with tracer insert techniques can also be taken care of this approach. The PIV technique has been briefly discussed in the following section.

2.6 Particle image velocimetry (PIV)

Particle image velocimetry (PIV) is an optical method of flow visualization used to obtain instantaneous velocity measurements and related properties in transparent materials. In short, the working of the PIV system is described here. The experimental transparent material is seeded with small tracer particles which are assumed to faithfully follow the flow dynamics. A laser sheet is passed through the experimental material and seeded tracer particles are illuminated by

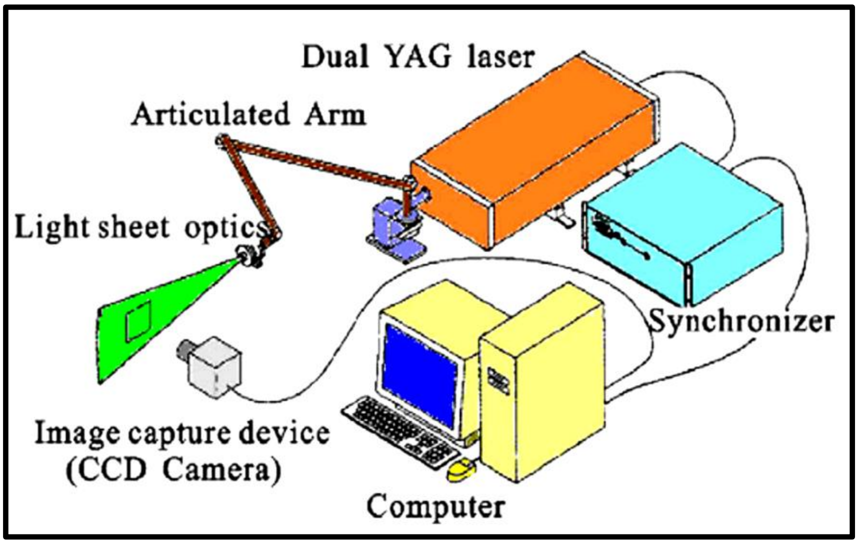

Fig. 2.24: Schematic of PIV system [146].

the laser sheet. The position of tracer particles at different times are recorded on a camera as shown in Fig. 2.24. Then, by measuring the particle displacements, the motion of the fluid can be ascertained.

The term ‘Particle Image Velocimetry’ (PIV) first appeared in the literature in the 1980s [133]. The significant scientific and technical progress achieved in the last three decades in lasers, image recording and evaluation techniques, and computer techniques led to the further development of the PIV technique. Presently, PIV has become a powerful tool for studying flow field in aerodynamics [134-140], fluid dynamics [124-132] and in biological parts [141]. The measurement principle and major developments of the PIV have been reviewed in many papers [142-144] and in a comprehensive book by Raffel et al. [145]. Herein, we introduce the PIV technology focusing on the applications in fluid dynamics. Particle image velocimetry is a technique to obtain a quantitative measurement of instantaneous velocity fields as an extension of qualitative flow visualization. It tracks the tracer particles seeded in the fluid to obtain the whole velocity field of the measurement area. A typical PIV system consists of a multi-pulsed laser system, one or more digital cameras synchronized with the lasers, and a computer to control the system and analyse the data [146]. A two direction-two component (2D-2C) PIV system uses one camera while a two direction-three component (2D-3C) PIV system uses two cameras. As for volumetric PIV system, such as tomographic PIV system, more than three cameras are required. Due to the complicated experimental setup and much more expensive price of a volumetric PIV system, the most common used PIV in fluid flow measurements is 2D-2C. The basic setup of a 2D-2C PIV system is shown in Fig. 2.24.

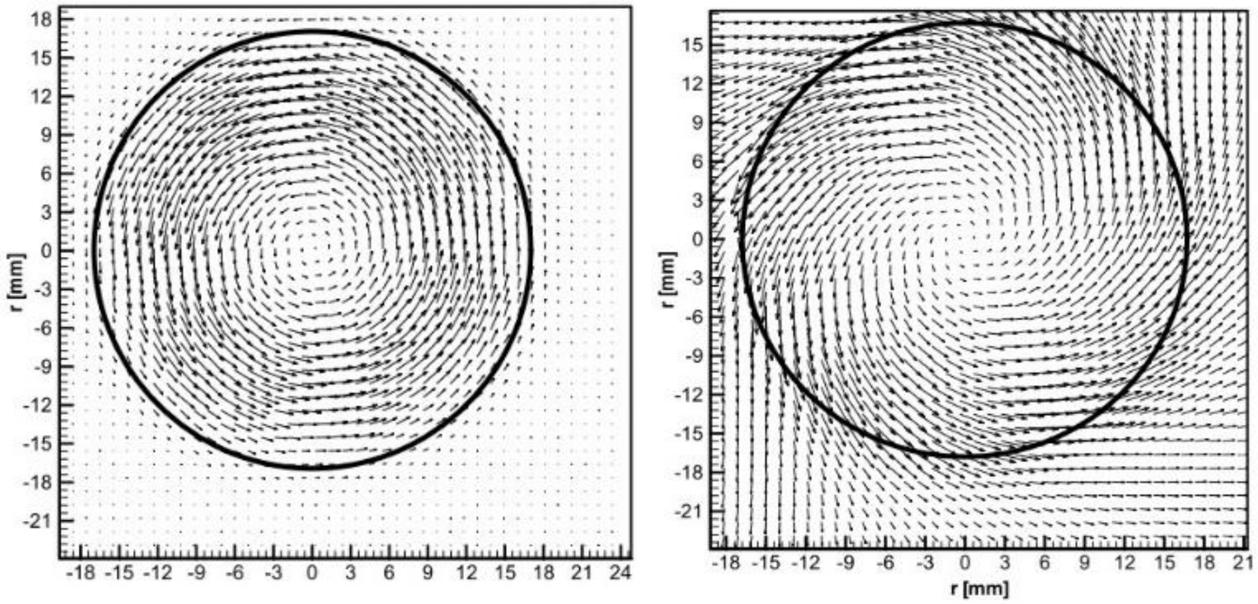

Fig. 2.25: PIV velocity vectors at the surface of the disk in the (r-φ) plane at 30 rpm, (a) water, and (b) non-Newtonian fluid [134].

Fig. 2.25 shows use of particle image velocimetry (PIV) technique for measurement of velocity vectors in a system containing rotating disc submerged in a fluid [134]. The flow properties of the two fluids (water and a non-Newtonian) is quite different. The maximum velocity was observed at r = R and r = R/2, R disc radius, in water and non-Newtonian fluid, respectively. From this, it is clear that the PIV technique was able to capture the effect of fluid properties on flow behaviour.

CHAPTER 3

PROBLEM FORMULATION

3.1 Observations from literature

In general, there is a good understanding of material flow during FSW obtained through tracer insert technique. However, it suffers from the drawback that tracer and workpiece materials are quite different. Few in-situ studies have brought out new insight in the flow characteristics. There is a large scope for application of techniques pertaining to in-situ visualization. Another aspect which requires a lot of attention is a quantification of velocity, strain and strain rate during FSW. There is still considerable variation in the reported values for strain and strain rate at the same processing conditions. There is a strong dependence of the values of strain and strain rate on the method used. Therefore validation of the values obtained from one method has to be verified by another method.

3.2 Objectives of the present work

Following objectives were defined to study the material flow behaviour, strain and strain rate precisely during FSW.

1. To understand material flow behavior during FSW by employing various techniques. A particular technique is not capable to explain material flow completely because each technique has some assumptions and drawbacks. Hence, herein three different techniques were adopted to understand material flow field.
2. To visualized material flow and determine strain experienced by the material during the FSW by inserting tracer of Al 5083 alloy in the workpiece of 5083 Al alloy. In this work, tracer was cut from workpiece material, in order to maintain the similarity between the physical and thermo-mechanical properties of both tracer and workpiece materials. Thus the tracer flow can be treated as the workpiece material flow. Hence this work is become important and different than the previous literature. However, tracer insert technique could only reflect the initial and final state of the tracers, hence rarely detailed material flow information of the material during the FSW process was obtained. To address this issue the third objective of the thesis was defined.
3. A novel approach based on PIV technique was adopted to understand material flow and strain rate measurement during friction stir welding or processing (FSW/FSP). Material flow around the tool pin was visualized by PIV technique using a micro spherical glass

tracer in a transparent visco-plastic fluid. The two dimensional material flow was obtained by following the path of the tracer. Unlike other methods, in this approach an in-situ visualization of material flow was performed by using PIV techniques to claim the uniqueness/novelty of the present work.

4. Numerical simulation of the FSW process using fluid dynamics software. PIV technique was first time used in this field, hence it became necessary to validate the experimental results obtained by PIV technique with the numerical simulation and compare the flow field during FSW.

3.3 Systematic approach

The present thesis is an attempt to understand material flow characteristics during FSW. Both experimental and computation analyses were performed. Following techniques were adopted.

Tracer insert technique is one of the most preferred technique for material flow analysis. However, measurement of velocity, strain and strain rate accurately is a complex problem. Few studies [50, 69, 98] measured the material flow velocity, strain and strain rate during the process, using seven times heavier tracer material than that of workpiece material. Some studies explained the material flow characteristics in the simulated material inserting steel balls as a tracer [68, 97, 122]. Most of the published work was performed by using different tracer material than that of the workpiece material. The presence of the foreign material could result in an inexpedient effect on the properties that control the flow, e.g. the contact condition and flow properties of the base material. Although, a great deal of understanding has been obtained using these techniques, still, two drawbacks are noticed; a) thermo-physical properties of the tracer and matrix materials are quite different, b) information about the intermediate positions of the tracer could not be obtained.

The first drawback was overcome herein by using tracer and workpiece materials of the same composition, physical and thermo-mechanical properties, hence it can be concluded with confidence that actual flow and strain experienced by the material was obtained. But the tracer insert technique could only reflect the initial and final state of the tracers, hence rarely detailed material flow information of the material during the FSW process was obtained.

The second drawback was overcome by physical simulation using particle image velocimetry technique. In this experiment, the tracer particle of micron size and with the almost same density as of the workpiece material was used. The amount of tracer material was negligible in comparison to experimental material, hence the properties of the experimental material were not affected by tracer material. The PIV technique is capable of providing instantaneous velocity field [147]. In metallic materials in-situ material flow visualization and measurement, using tracer and workpiece of the same density is not possible. But PIV technique provides in-situ flow visualization and measurement of material flow velocity and strain rate during the process in a precise manner [133]. Finally, a numerical model of the process is presented and validated with the experimental findings of PIV.

CHAPTER 4

DETAIL OF MATERIAL FLOW INVESTIGATION TECHNIQUES

4.1 Tracer insert technique

The tracer insert technique (TIT) is well established technique for material flow investigation. This technique provides information about flow from the tracer position after the process.

4.1.1 Workpiece and tracer materials

A rolled plate of 5083 aluminium alloy of 6.35 mm thickness was used as workpiece material. The tracer was prepared from the same plate hence physical and chemical properties of tracer were same as the workpiece material.

4.1.2 Tracer preparation

The dimensions of the workpiece were 70×50×6.35 mm^3. For the tracer, a thin strip of 0.5 mm was obtained from the workpiece by electro discharge machining (EDM). The strip thickness was reduced from 0.5 to ~0.36 mm by SiC papers of different grades. The strip was

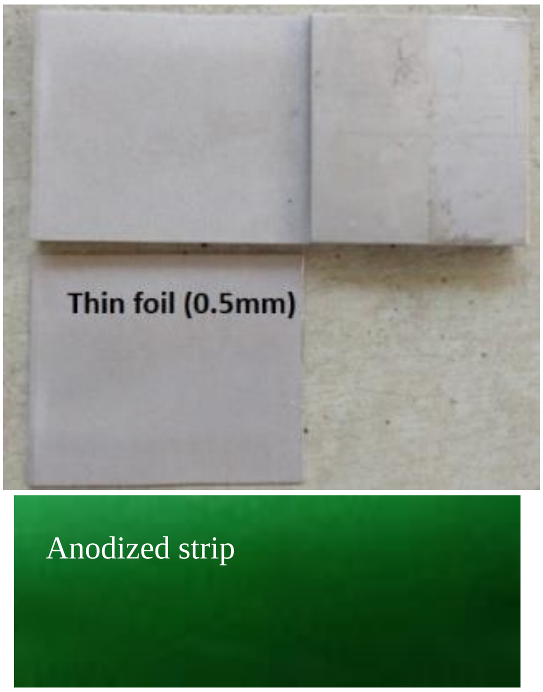

Fig. 4.1: Tracer preparation from workpiece material.

anodized before inserting into the grooves of the workpiece created by EDM as shown in Fig. 4.1. Anodizing is done to identify the position of the tracer in the workpiece after the process.

4.1.3 Tracer placement

The tracers were placed in three orientations, (i) tracer plane normal to tool traverse (parallel to yz plane), see Fig. 4.2a, (ii) tracer parallel to the processing surface (parallel to the xy plane) at different depths from the top surface as shown in Fig. 4.2b, and (iii) tracer plane parallel to the tool traverse (parallel to xz plane) at seven locations with respect to the PCL as shown in Fig. 4.2c. The gap between the tracers was kept at 1 mm and individual experiments were performed for each tracer.

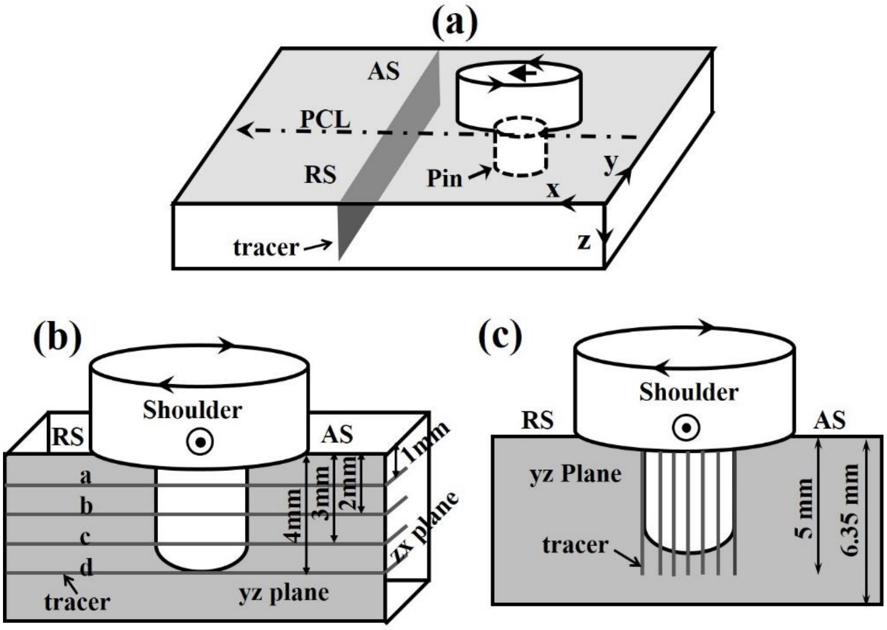

Fig. 4.2: Schematic of tracers placement (shown here as lines) and observed planes (grey color) (a) tracer plane normal to tool traverse (parallel to yz plane), (b) tracer parallel to the processing surface (parallel to the xy plane) at four locations (1 mm gap between tracers and) (c) tracer plane parallel to the tool traverse (parallel to xz plane) at seven locations (1 mm gap between tracers).

4.1.3 FSW process equipment

Fig. 4.3 shows the friction stir welding machine with a 3 HP motor, mounted on the top. The spindle speed varies by shifting the V-belt to the desired groove (mounted on spindle and motor shaft) of four step cone-pulleys. Four high (720-2260 rpm) and four lower (125-410 rpm) spindle speeds were provided. A hydraulic power pack controlled the movement of a semi-automatic adjustable working table.

The workpiece is fixed in the fixture, which is fixed on the working table with an attachment as shown in Fig. 4.3. The workpiece was securely held from the sides, constrained by a steel backup at the bottom and clamped from the top so that the workpiece remains stationary during the process. The working table has three mutually perpendicular movements, in the x-direction (traverse speed), y-direction (across) and z-direction (tool plunge). The vertical and across movements were manually controlled. The vertical spindle head can be swivelled at any desired angle. The tool was firmly held in a collet and plunging of the tool pin was done manually.

Fig. 4.3: FSW machine setup.

4.1.4 FSW operation

Rotating tool pin was plunged into the workpiece until the shoulder comes in contact with the workpiece surface. Before plunging the tool pin into the workpiece it is confirmed that the tool pin was in the desired position with respect to the tracer position by adjusting the working table. After that, the rotating tool pin was plunged manually into the workpiece. The rotating tool was kept stationary for a few seconds (10-20 seconds) and then a traverse motion was provided to the working table.

4.1.4.1 Tool geometry

The FSW tool was prepared with a cylindrical concave shoulder and a concentric cylindrical pin, as shown in Fig. 4.4. The diameter of the tool shoulder was 25 mm and cylindrical pin with 6 mm diameter and 4 mm length was prepared from tool steel.

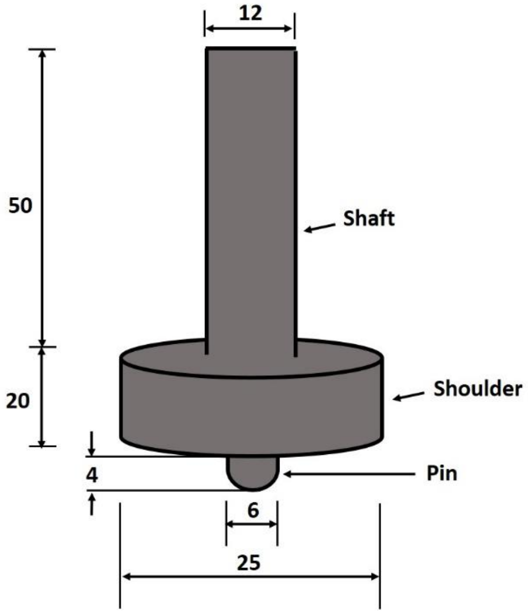

Fig. 4.4: Tool used in friction stir welding (dimensions in mm).

4.1.4.2 Process parameters

During FSW process 1025 (rpm) rotational speed and 67 mm min^{-1} traverse speed was used in all experiments. The tool was tilted at 1.5° towards the trailing edge with respect to the plate surface during the process. At these process parameters the weld was obtained defect free.

4.1.5 Tracer visualization

To visualize tracer position after FSW, samples were sectioned from the workpiece and polished using different grades of SiC papers. The final polishing was performed on cloth. After cloth polishing, the optical image of the region surrounding the tracer was obtained. In the optical image, the workpiece and tracer materials appeared bright, whereas the anodized surfaces of the tracer appeared dark. Metallographic investigation of the position of the tracer provided detail information regarding the material flow.

4.2 Particle image velocimetry technique

Particle image velocimetry (PIV) is a non-intrusive optical imaging technique to capture the instantaneous/ensemble averaged flow field and fluid velocity information of the whole flow fields within fractions of a second [129]. The necessary condition for PIV measurements is that the flow must be embedded with small tracer particles, which can scatter a sufficient amount of light as well as faithfully follow the flow. The ability of whole field measurements with high accuracy, high spatial resolution and without intruding the flow has elevated PIV to a special status in fluid mechanics.

For PIV, the experimental material should be transparent, hence a transparent gel (substitute of metal during the FSW process) is chosen as an appropriate modelling material. Once the experimental material was established it can then be used for material flow visualization and measurement. It is believed that the experimental simulation can be refined to the point that it distinguishes between material flow trends based on input parameters. The intent of this study is to provide a more complete and clear picture of material flow regimes in the FSW. It is recognized that material flow during the FSW depends on workpiece material, tooling, and operating conditions, and hence, studies on the simulated material are suitable to illustrate extreme cases.

4.2.1 Working principle

Fig. 4.5 briefly illustrates a typical experimental arrangement for PIV image acquisition. For PIV measurements, tracer particles are illuminated by employing specialized lasers at least

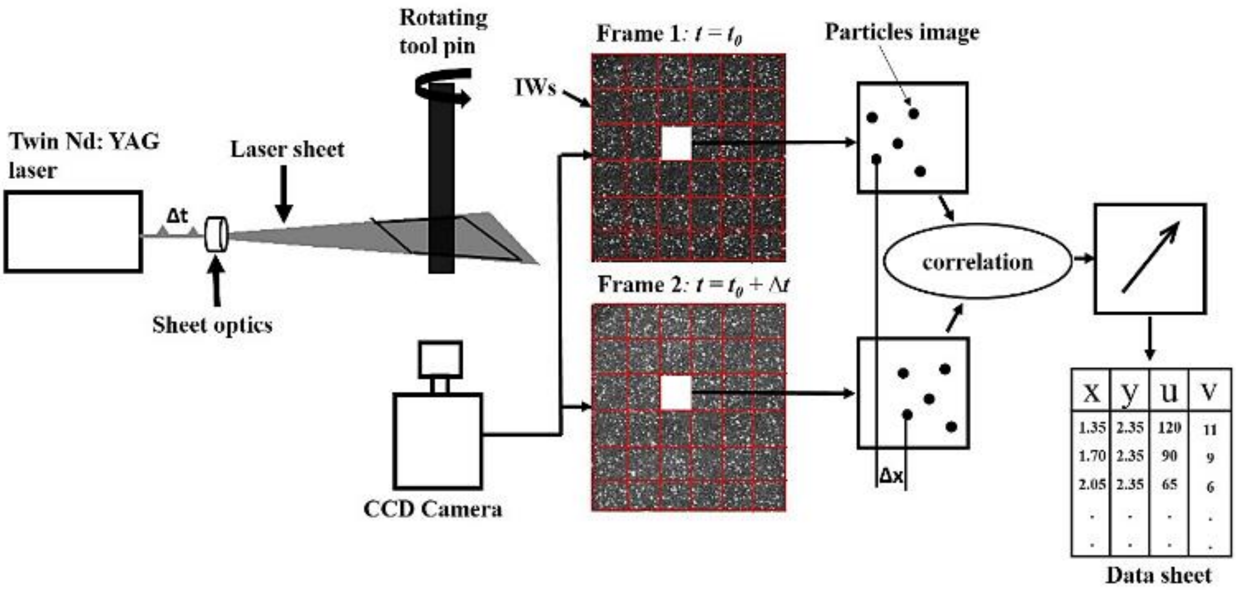

Fig. 4.5: Experimental arrangement for PIV acquisition.

twice within a very short time interval. The time delay between two collinear laser pulses is referred to as pulse separation time (Δt) and is adjustable according to the mean flow velocity.

The positions of the illuminated particles in flow at successive instants are recorded on a high speed CCD camera. These frames are referred to as Frame 1 and Frame 2 corresponding to the particle positions at times $t = t_0$ and $t = t_0+\Delta t$, respectively. To increase the accuracy of the results, hundreds of image pairs are captured. [38]. The spatial resolution, detection rate, accuracy and reliability of a PIV depend critically upon the careful selection of a number of parameters of the PIV system and the fluid motion [143, 147,150, 154]. Detail about the PIV working, designing rules, selection of time (Δt) between two laser fires and operation sequences are given in appendix A.

4.2.2 Required material

To investigate material flow characteristics by PIV technique in the present work, three components are required i.e. experimental material, seeding/tracer particles and FSW machine model.

(a) Experimental material

Fig. 4.6: Experimental material.

Prior to the study of the material flow by PIV technique, the rheological study of the experimental material (shown in Fig. 4.6) was performed. The rheological characteristics, such as shear stress vs shear rate, and viscosity vs shear rate, of the material were measured using a rheometer (Anton Paar, MCR100, shown in Fig. 4.7) with a tool PP-50 and keeping the gap between the plates as 0.5 mm.

Fig. 4.8 shows the rheological curves, obtained from rheometer, of the experimental material at the room temperature. Over a wide range of shearing, the rheogram shows that the viscosity (μ)

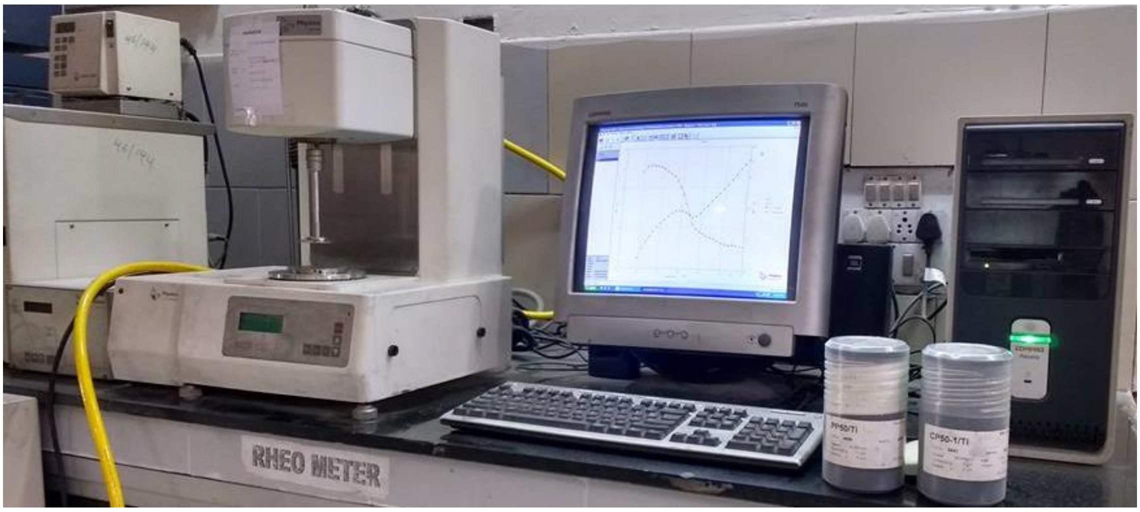

Fig. 4.7: Anton Paar MCR100, Rheometer.

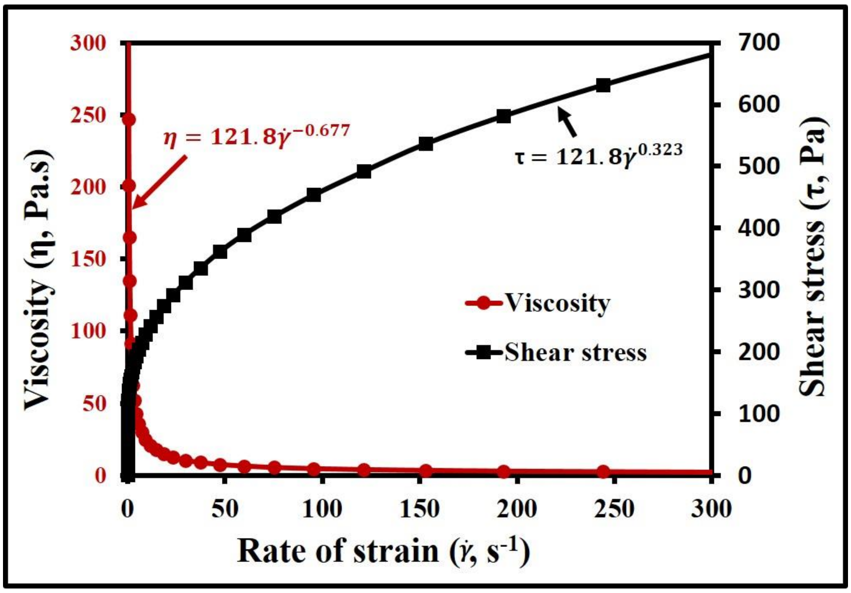

Fig. 4.8: Rheological properties of the physical modelling material, used for flow visualization.

of the material decreases with an increase in the rate of strain ($\dot{\gamma}$). The modelling material, therefore, shows power law flow behaviour [148, 160], as expressed in Eq. (4.1)

$$\eta = m\dot{\gamma}^{n-1} \tag{4.1}$$

where η viscosity, $\dot{\gamma}$ rate of strain, m and n consistency and power-law indexes of the fluid respectively.

(b) Tracer particles

Hollow spherical glass particles were used as a tracer material, shown in Fig. 4.9. The glass particles are non-toxic, non-corrosive, and chemically inert. The tracer particles are in the spherical shape with mean diameter of 8-12 μm. Due to a spherical shape and small size, the tracer particles truly follow the material flow path that required for flow visualization during the process. The refractive index of the tracer material is 1.5, so that, it scattered sufficient light for imaging. The density of the tracer material is 1050-1115 kg m^{-3}, which is near to the processing material density (1000 kg m^{-3}). Due to the negligible amount of tracer particles, in comparison to overall processing material, the density of the processing material remained constant. Therefore, the study was performed without altering the physical properties of the base material.

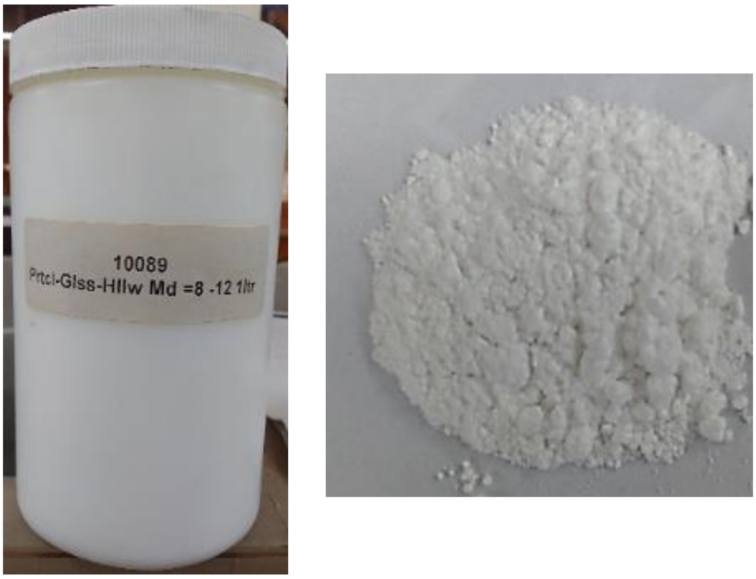

Fig. 4.9: Hollow glass particles, used as a tracer.

(c) FSW machine model

A model of the FSW machine was fabricated for material flow visualization which was connected with PIV setup. The model setup and its components are shown in Fig. 4.10. The model could provide rotational speed in the range of 50-6000 rpm and traverse speed in the range of 50-140 mm min^{-1}. The model was designed to have movements in three directions (similar to FSW machine), in the x-direction (traverse), in the y-direction (across to bring camera in focus) and in the z-direction (rotating head movement, up and down).

The tool was mounted on the shaft of a motor of variable speed (speed controlled by a speed drive) which provide rotational speed to the tool. The traverse movement was provided by a reversible synchronous motor having constant rpm (60 rpm). However, the traverse speed was varied by changing the gear ratio. The driver gear directly was mounted on the motor shaft and driven gear on a lead screw.

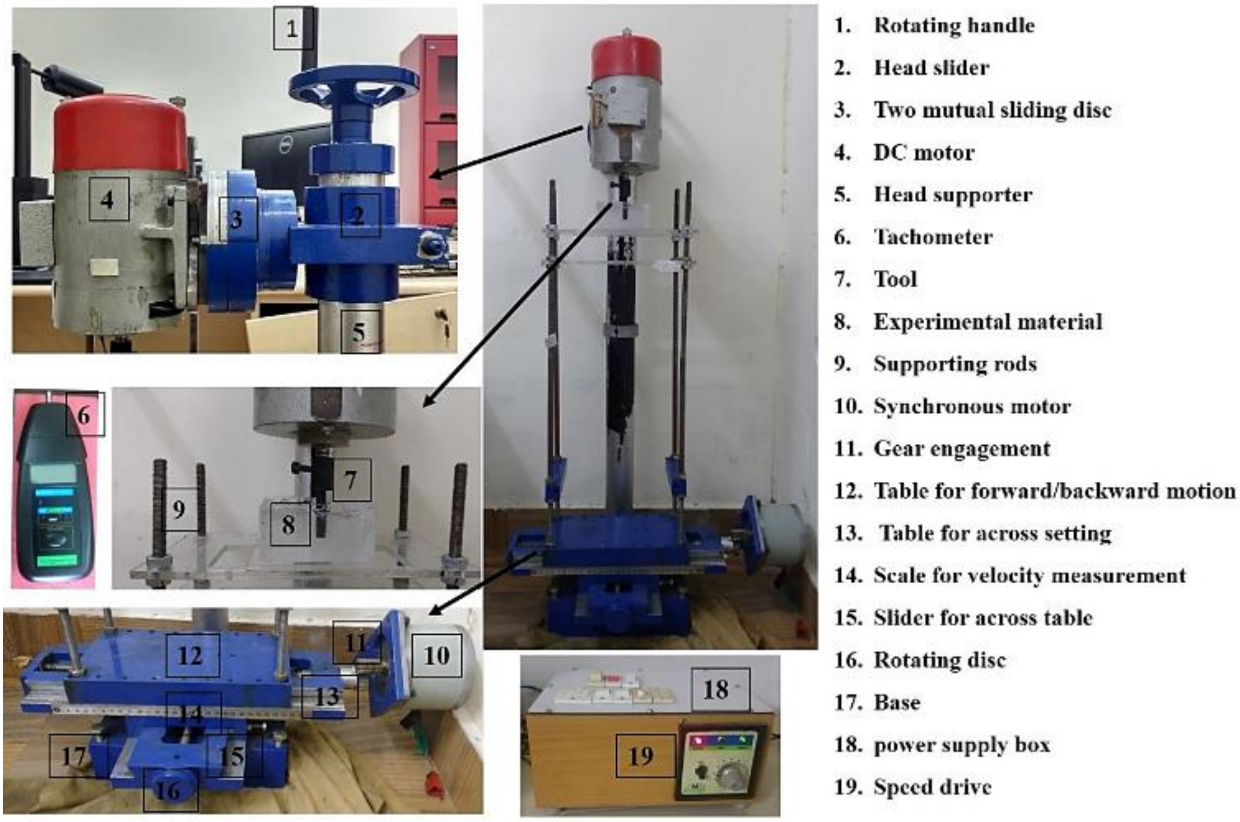

Fig. 4.10: FSW machine model for PIV application.

4.2.3 Image acquisition system

The image acquisition system mainly comprises of a laser source, a light sheet optics, a CCD camera, a synchronizer and a powerful workstation equipped with the frame grabber and the INSIGHT 4G™ software as shown in Fig. 4.11.

Fig. 4.11: PIV system parts: CCD camera, synchronizer, workstation, laser power source, laser head, laser arm and light sheet optics.

4.2.3.1 Laser and light sheet optics

Lasers are typically used as the light source to illuminate the seeded particles in the test section for PIV measurements. However, different laser types are used over the years that include Helium-neon, Copper-vapour, Argon-ion, Neodymium-Yttrium Aluminium Garnet (Nd-YAG), Ruby, and Semiconductor Lasers. The PIV system is equipped with a laser system that comprises a laser power source to control the laser emission and a laser head with attached cylindrical and spherical lenses. A double-pulsed Nd:YAG laser system (Model: EverGreen BIG SKY LASER SERIES (150 mJ @532 nm), Make: Quantel Laser) that emits a light beam with a maximum energy output of 150 mJ/pulse is used in the present investigation. To carry a laser beam from laser head to measuring section, an arm is attached between laser head and light sheet optics (Fig. 4.11). The collimated light beam emitted from laser system is passed through a sheet optics which contain spherical lens of negative focal length to diverge the beam in the horizontal plane and the cylindrical lens of positive focal length to control the thickness of the light sheet [125]. Therefore, a combination of spherical and cylindrical lenses is attached to the laser head, with the help of an integrated laser mount, for converting laser beam to a light sheet of about 1 mm thickness in order to facilitate proper illumination of the selected region of interest.

4.2.3.2 Camera and image acquisition

A commercially available Power View™ Plus 4MP-HS CCD camera (Model: 630091 Power View Plus, Make TSI) exclusively designed for global flow measurements, is used for image acquisition of the illuminated seeded flow field. The camera encompasses a built-in mask for shielding the CCD circuitry from laser light reflections, making it appropriate for imaging laser-illuminated flows. The CCD camera offers high resolution (2048×2048 pixel) with a pixel size of 7.4×7.4 μm, short frame straddling times, functions at a frame rate of 32 fps, and delivers a 12-bit output. The camera is coupled with a standard Nikon 50 mm F1.8 lens for focusing the region of interest, see Fig. 4.11).

4.2.3.3 Synchronizer

The Laser pulse synchronizer is a programmable master timing control unit for use in PIV applications. Acting as the master controller for system components, it automates timing between laser pulses, camera, camera interfaces, and any external device during image acquisition with 1 ns resolution. The synchronizer enables the system to be completely computer-controlled via a serial interface. Signals for the laser flash lamps and Q-switches, the camera, and the frame grabber are generated and automatically synchronized for image acquisition.

4.2.4 Image processing

Typically, PIV recordings are sub-divided into small grid blocks in order to extract the local displacement information [147]. These small grid blocks are referred to as interrogation regions or interrogation areas (IAs). For better results, the number of particles per interrogation area should be at least 5 and the maximum particle displacement in an interrogation area should be equal to ¼ of the size of the interrogation area [149] [150]. The principle of PIV image processing by means of a statistical method i.e. cross-correlation is illustrated in Fig. 4.12. The local displacement vector (Δx) of the particles between the first and the second image in each IA is evaluated using the cross-correlation method. The most portable displacement recognized by the peak in the cross-correlation function is determined numerically by means of efficient Fast Fourier Transform (FFT). By calculating the local particle displacement Δx and Δy over the time Δt, the local velocity and can be estimated within the IA. This process is repeated for all IAs to obtain the velocity vector map of the captured flow-field. However, the processing time of one image pair with several thousand instantaneous velocity vectors is mainly dependent on the size of the image pair, the interrogation area, and on the processing algorithm.

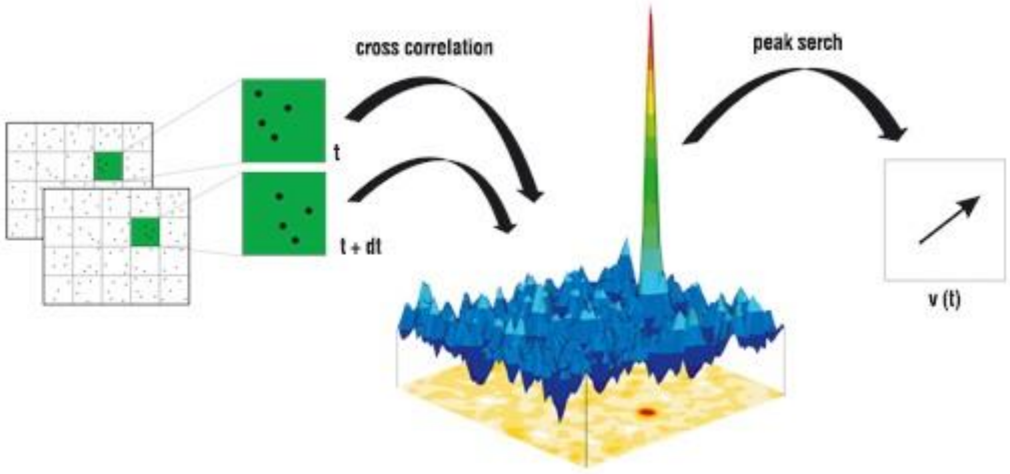

Fig. 4.12: Cross co-relation for PIV image [149].

Calculation of material flow velocity and related properties

Velocity:

PIV provides the spatial coordinates of two subsequent time frames, times t_o and $t = t_o + \Delta t$, respectively. These are then used to calculate the velocity in x and y-directions as expressed in equations (4.2-4.4).

$$u(x, t) = \frac{x_{i+1} - x_i}{\Delta t} \tag{4.2}$$

$$v(y, t) = \frac{y_{i+1} - y_i}{\Delta t} \tag{4.3}$$

$$resultant\ velocity\ (V) = \sqrt{u^2 + v^2} \tag{4.4}$$

Where x_i, y_i and x_{i+1}, y_{i+1} are spatial coordinates at time exposures of t_o and $t_o + \Delta t$. Δt represents the time difference between two captured frames (see Fig. 4.5), u and v are the velocities in x- and y-directions, respectively, and V is the resultant velocity.

Streamlines:

The streamlines show flow behaviour of the material during the process. Therefore, streamline indicates the direction of motion of particles at each point and mathematically, the equation of streamline in 2-D space can be written as Eq. (4.5)

$$tan\theta = \frac{v}{u} = \frac{dy}{dx} \tag{4.5}$$

where u and v are the velocity components in x- and y- directions, respectively.

Strain rate:

The strain rate (rate of strain, $\dot{\gamma}$) was calculated from two-dimensional velocity field obtained from the post-processing of PIV results. Strain rate is expressed in terms of velocity gradients. Mathematically, it is given by Eq. (4.6), [158-160].

$$\dot{\gamma} = \sqrt{2\left(\frac{\partial u}{\partial x}\right)^2 + \left(\frac{\partial u}{\partial y} + \frac{\partial v}{\partial x}\right)^2 + 2\left(\frac{\partial v}{\partial y}\right)^2} \tag{4.6}$$

4.3 Numerical modelling

The numerical simulation of the FSW with the help of computational fluid dynamics (CFD) tool has also been performed in this thesis for detailed understanding of material flow and to ascertain the possibility of overcoming the drawbacks faced by the experimental techniques. Additionally, numerical simulation can incorporate influence of multiple processing parameters on flow field, which is not possible with experimental procedures. Furthermore, the advantages of numerical simulation over experimental investigation include minimisation of experimental trials and faster investigations, with the large number of data points available throughout the domain.

Material flow is an important phenomenon that governs the FSW process. In this thesis, the plasticized material is treated as a high viscosity power-law fluid and the flow field is obtained using computational fluid dynamics.

4.3.1 General assumptions and governing equations

The material is taken as an isothermal, incompressible single-phase fluid with non-Newtonian shear-dependent viscosity. The physical properties of the material remains constant throughout the process. The velocity component in the z-direction (*w*) is negligible as compared to the other two (x and y) direction velocity components (*u* and *v*), hence we consider 2-D flow.

Based on the above approximations, the process is governed by the mathematical statements of the two laws of conservation for the physical system: conservation of mass (i.e., mass continuity equation) and conservation of momentum (Navier-Stokes equation). The continuity and momentum conservation equations for incompressible single-phase flow are given as.

$$\rho \nabla.(u) = 0 \tag{4.7}$$

$$\rho(u.\nabla)u = \nabla.[-p + \eta(\nabla u + (\nabla u)^T)] + \mathrm{F} \tag{4.8}$$

where ρ is the density of the fluid, η is the strain rate-dependent viscosity, p is the pressure, u is the fluid velocity vector and F is the external force (that is zero in this case). The viscosity and density of materials are considered similar to those used in PIV study.

For a power law fluid the viscosity is given by [158-160]

$$\eta = m\dot{\gamma}^{n-1} \quad \text{and} \quad \dot{\gamma} = \sqrt{2I_2} \tag{4.9}$$

where m is the flow consistency index, n is the flow behaviour index of the fluid ($n < 1$, $=1$ and >1 corresponds to a shear-thinning, a Newtonian and a shear-thickening fluid), and I_2 the second invariant of the rate of strain tensor, which is given by

$$I_2 = \left(\epsilon_{xx}{}^2 + \epsilon_{yy}{}^2 + \epsilon_{xy}{}^2 + \epsilon_{yx}{}^2\right) \tag{4.10}$$

The components of the rate of strain tensor are related to the velocity components in Cartesian coordinates as follows:

$$\epsilon_{xx} = \frac{\partial u}{\partial x} \tag{4.11a}$$

$$\epsilon_{yy} = \frac{\partial v}{\partial y} \tag{4.11b}$$

$$\epsilon_{xy} = \epsilon = \frac{1}{2}\left(\frac{\partial u}{\partial y} + \frac{\partial v}{\partial x}\right) \tag{4.11c}$$

Substituting the value of I_2 in Eq. (4.9)

$$\dot{\gamma} = \sqrt{2\left(\frac{\partial u}{\partial x}\right)^2 + \left(\frac{\partial \mathrm{u}}{\partial \mathrm{y}} + \frac{\partial \mathrm{v}}{\partial \mathrm{x}}\right)^2 + 2\left(\frac{\partial \mathrm{v}}{\partial \mathrm{y}}\right)^2} \tag{4.11d}$$

4.3.2 Geometrical model and boundary conditions

Fig. 4.13 illustrates the geometrical model used in the numerical simulation. The dimensions of the workpiece and the geometry of welding tool are taken the same as the experimental setup in PIV. The process material is moving with traverse/welding speed (V_T), i.e. rigid surfaces A, B, C & D are moving with same velocity. At the tool pin surface, a tangential velocity (V_R=ωr) provided with the no-slip condition, as shown in Fig. 4.13.

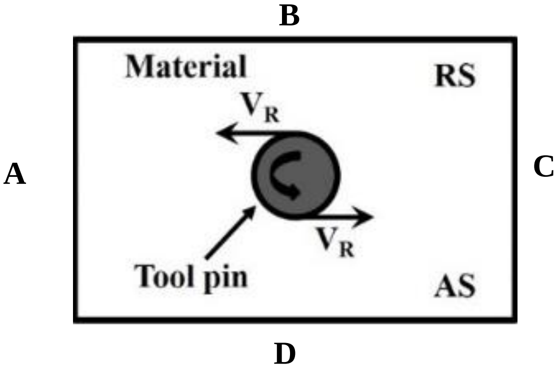

Fig. 4.13: Boundary conditions applied in simulation.

The above governing equations in conjunction with boundary conditions have been solved using the finite element method (FEM) based computational fluid dynamics (CFD) tool COMSOL Multiphysics. The computational domain has been discretised with extremely fine triangular grid structure, as shown in Fig. 4.14. The numerical simulations have been performed for the same ranges of conditions as explored in PIV techniques.

Based on the techniques discussed in this chapter, the results have been validated and new findings are presented in the ensuing chapters.

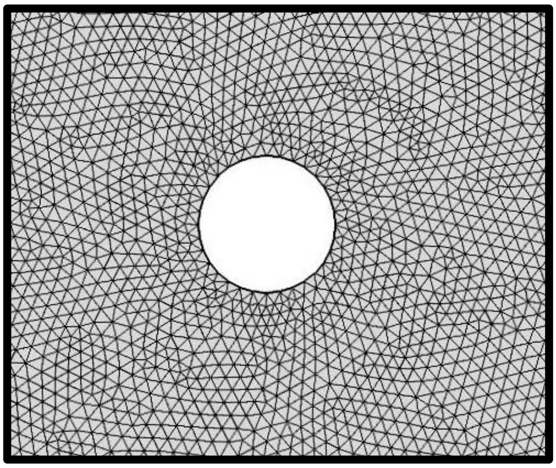

Fig. 4.14: Mesh representation in the computational domain.

CHAPTER 5

MATERIAL FLOW ANALYSIS USING TI TECHNIQUE

5.1 Material flow

In the following sections, the material flow is described by using information from the post-process position of tracers placed at different locations and in different orientations.

5.1.1 Tracer plane normal to tool traverse

Fig. 5.1 shows the flow behaviour of the tracer at different depths (0.7, 1.4, 1.9, 2.6, and 3.7 mm) from top surface to pin tip. In Figure vertical lines represent the mid-plane of the tracer in un-deformed configuration and two horizontal parallel lines represent the edges of the pin.

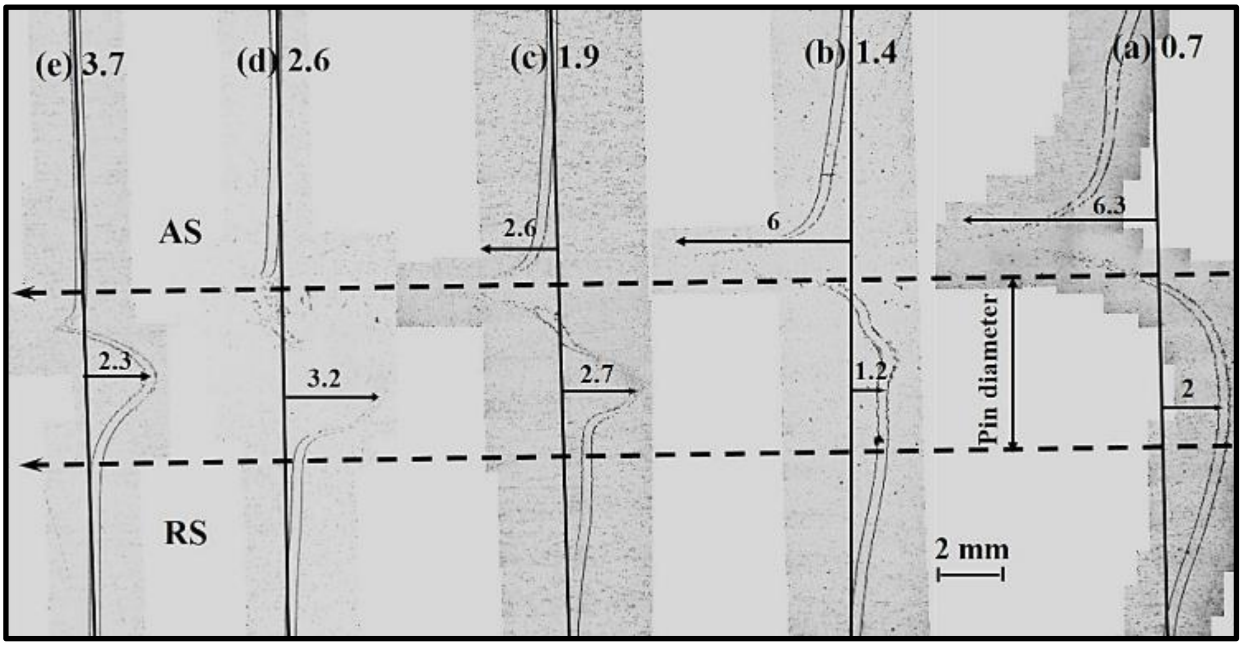

Fig. 5.1: Tracer positions captured after FSW, parallel to the processed plane at different depths, (a) 0.7 mm, (b) 1.4 mm, (c) 1.9 mm, (d) 2.6 mm and (e) 3.7 mm from top surface.

The tracer displacement with respect to pre-process tracer positions is explained in following sub-sections.

i) ***Tracer position at 0.7 mm depth from top surface:*** close to top surface, the tracer followed tool rotation and formed a large curvature compared to pin circumference. Also, the tracer was pushed backwards in the RS and dragged forward in the AS. The deviation of the tracer from its initial position start at 10 mm from PCL in the RS and approximately at 12 mm in AS. The diameter of the shoulder was 25 mm. Therefore at this location, effect of shoulder on material flow appear to be significant. The tracer in the curvature remained continuous from RS to edge of the pin in AS. After that, tracer disintegrated and was pulled in the direction of the tool traverse. The tracer was fragmented due to large strain experienced by the material [82]. The probable reason for stretched tracer at this location is combined motion of rotation and traverse in the same direction.

ii) ***Tracer position at 1.4 mm depth from top surface:*** the tracer at 1.4 mm depth experienced minimum displacement in the backward direction to the tool traverse whereas in the AS it shows almost similar dragging as at 0.7 mm depth. The distance from PCL of the starting point of deviation also reduced probably due to lower influence of shoulder at this depth.

iii) ***Tracer position at 1.9 mm depth from top surface:*** at 1.9 mm depth, the tracer in the RS formed an inverted C type curve with maximum deviation approximately equal to pin radius. Interestingly, dragging of the tracer starts before PCL and fragmentation starts within nugget zone instead of at the edge of the pin. This is contrary to observation made by using Cu or bronze as tracer [83, 84, 85]. Between center to AS edge of the pin tracer got position at PCL. At the AS tracer was dragged in forward direction up to 2.6 mm.

iv) ***Tracer position at 2.6 mm depth from top surface:*** at 2.6 mm depth, tracer deflect in the backward direction to the tool traverse at RS and disintegrates before PCL in the nugget zone. The tracer formed inverted C type curve same as found at 1.9 mm position. At the pin edge in the AS, tracer is fragmented and did not show forward displacement.

v) ***Tracer position at 3.7 mm depth from top surface:*** near tip of the pin or bottom of the nugget zone, the tracer remains continuous and formed the same curve as the top surface with small width and depth. The depth of the curve is less than the pin radius.

Material transport during the process is a result of two tool motions, translation and rotation, and the material flow asymmetry during the process. The bulk of the material moves around the pin to the final position behind its original position. In the AS the material flow in forward and backward directions, but in the RS, the material flow in backward direction only. The figure indicates that the material flow up to 1.5 mm depth from top surface is controlled by tool shoulder known as “shoulder driven flow” and below it by tool pin known as “pin driven flow”.

Fig. 5.2 is 3D plot of the tracer positions extracted from Fig. 5.1. In Fig. 5.2, the process direction is in negative X-direction and tool rotation is clockwise, therefore the negative Y axis is RS. The tracer material deflects in the direction of the process on the advancing side and opposite to the process on the retreating side. It can be seen from the figure that the bulk of the material is transported to a position behind its original position, by a length of not more than one pin diameter. At the RS, the backward displacement from its original position of the tracer is decreased continuously from top to 1.4 depth (minimum tracer displacement i.e. 1.2 mm back of the tool from its original position), below this depth the tracer displacement is equal or more than pin radius. At the AS, near the top surface a substantial amount of the material transport forward (in the process direction) from its original position, by the action of shoulder. At larger depth, where the influence of the shoulder is diminished, only small amount of the tracer material on the AS, was detected in front of its original position, see Fig. 5.1. further, a flow arm is also formed at the AS away from the pin edge and its distance continuously decrease up to mid-length of the pin and near pin tip it formed within pin diameter, due to rounded tip of the tool pin. This indicate that, width of the deformation zone decrease with an increase in depth and supported by [73, 74, 82, 83].

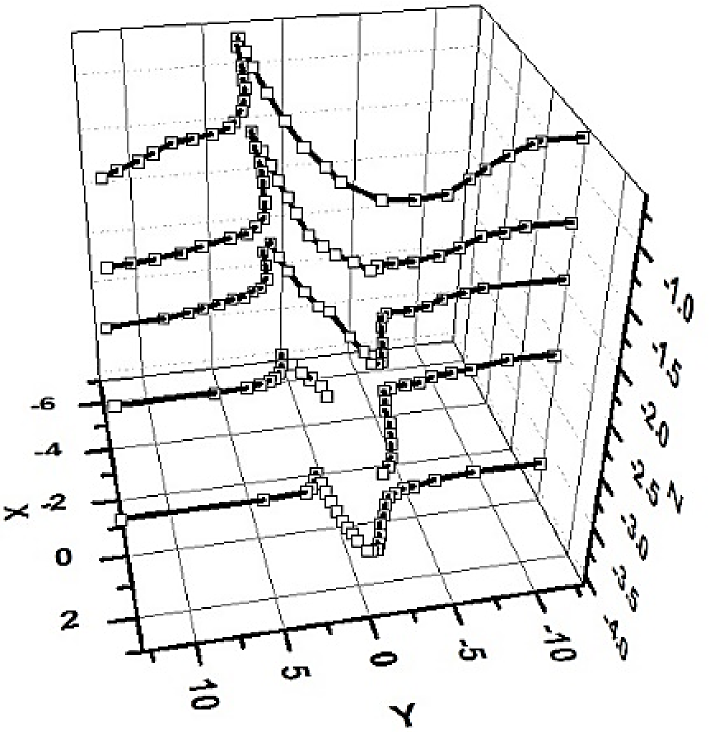

Fig. 5.2: 3D plot of tracer flow.

5.1.2 Tracer parallel to the processing surface

The material flow explained in previous section does not provide any information about the vertical mixing of the material during the FSW process. The tracer parallel to the processing surface is best suited for giving detailed information about the vertical mixing. Fig. 5.3 showed the tracer position after FSW process and brings out vertical material flow.

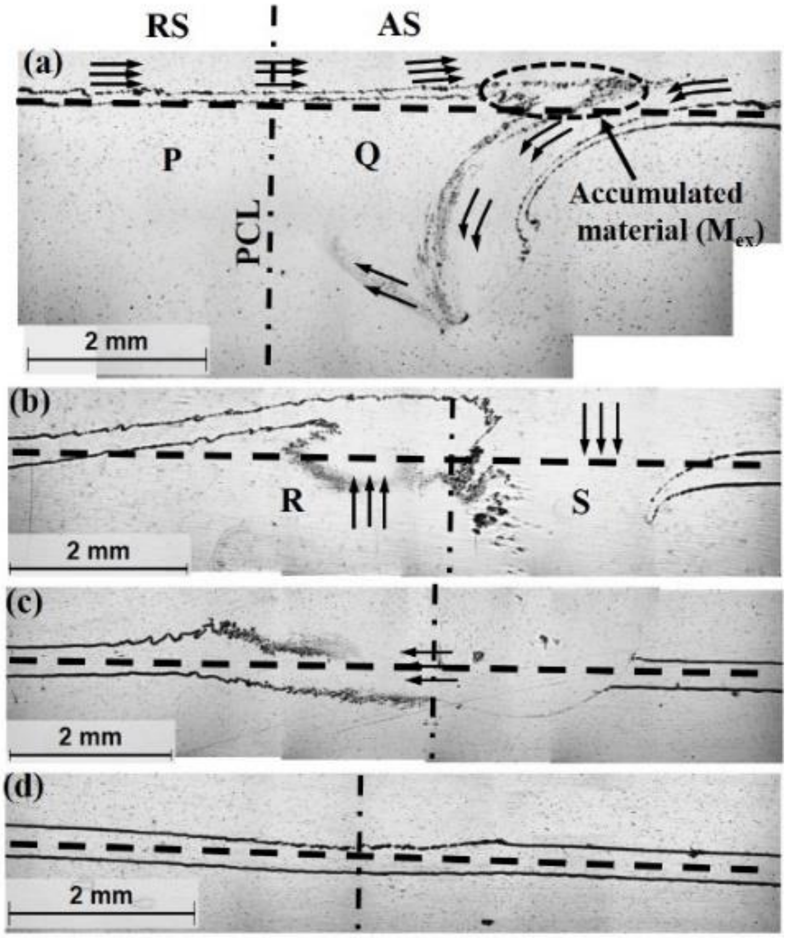

Fig. 5.3: Optical image of tracer flow during the FSW process, for the tracer placed before process at different depths from the top surface; a) 1.18 mm, b) 2.18 mm, c) 3.18 mm and d) 4.18 mm.

Fig. 5.3 shows the material flow in the yz plane (process direction is normal to this plane). The tracers were positioned at 1.18 mm, 2.18 mm, 3.18 mm and 4.18 mm distance from the top surface of the workpiece as shown in Fig. 4.2b. The tracer displacement due to material flow during the FSW process is explained in the following text.

i) ***Tracer placed at 1.18 mm from the top***: The shape of the tracer after the process can be divided into two segments, P and Q. In segment P, the tracer is continuous from RS to AS up to a distance of approximately 2-4 mm from the process centerline (PCL). The thickness of the tracer reduced to 0.12 mm from an initial thickness of 0.36 mm. In the segment Q, at the distance of 2-4 mm from PCL, the tracer broke and was forced downward during the process. In addition to the downward movement, there was inward displacement (towards PCL). The displacement appears to increase as a function of distance from the top. There was also deposition (inside the elliptical part in Fig. 5.2a) of the tracer material at the position where tracer broke into two segments.

ii) ***Tracer placed at 2.18 mm from the top:*** After the process, the tracer at this location can also be divided into two segments, R and S. Segment R is continuous up to some distance, after that the upper and lower surfaces of the tracer broke at two different locations. The upper surface broke approximately at PCL whereas, the lower surface at 2 mm before PCL. The tracer is continuous but appear to be tilted, suggesting lifting of the tracer due to upward flow. Material accumulation is also apparent for this tracer, however, the location now shifted toward RS. In the segment S, the tracer is absent for approximately 2 mm from PCL. After that, the tracer was forced downwards in the AS. It is clear that the downward and inward material flow observed for tracer placed at 1.18 mm broke the tracer placed at 2.18 mm and forced it to accumulate near PCL. The accumulation near PCL at the RS mid-depth is due to material compressed from the top (by shoulder) and material flow in the upward direction from the pin tip (discussed later). The tracer at 1.18 mm does not show this effect, probably due to the dominance of shoulder effect on material flow.

iii) ***Tracer placed at 3.18 mm from the top:*** The upper surface of the tracer is lifted in RS between 3.5 mm to 2 mm from PCL. The tracer disappeared after that up to 2.5 mm from PCL in AS. The lower surface of the tracer, however, is continuous but was forced downward from 3 mm in RS to 2 mm AS, measured from PCL. The effect of the downward material flow observed in the earlier two tracers can be seen on this tracer also.

iv) ***Tracer placed at 4.18 mm from the top:*** the tracer is continuous, however, there is a small downward shift. The upper surface of the tracer is continuous, but serrations were observed due to the effect of the pin tip. However, the lower surface of the tracer remains unaffected and continuous. It is clear that at this location the material flow was almost negligible.

5.1.3 Tracer plane parallel to the tool traverse

Fig. 5.4 shows the position of the tracer in the yz plane within the nugget zone after the welding process. Before processing, the tracers were placed parallel to the pin at seven positions; at 1.18 mm, 2.18 mm, 3.18 mm distances from PCL (or centre of the tool pin) on both the sides (AS and RS) and one tracer was placed at PCL, as shown in Fig. 4.2c. For comparison, the position of the tracers before the process is shown with dashed vertical lines. The material flow direction is shown with solid arrows.

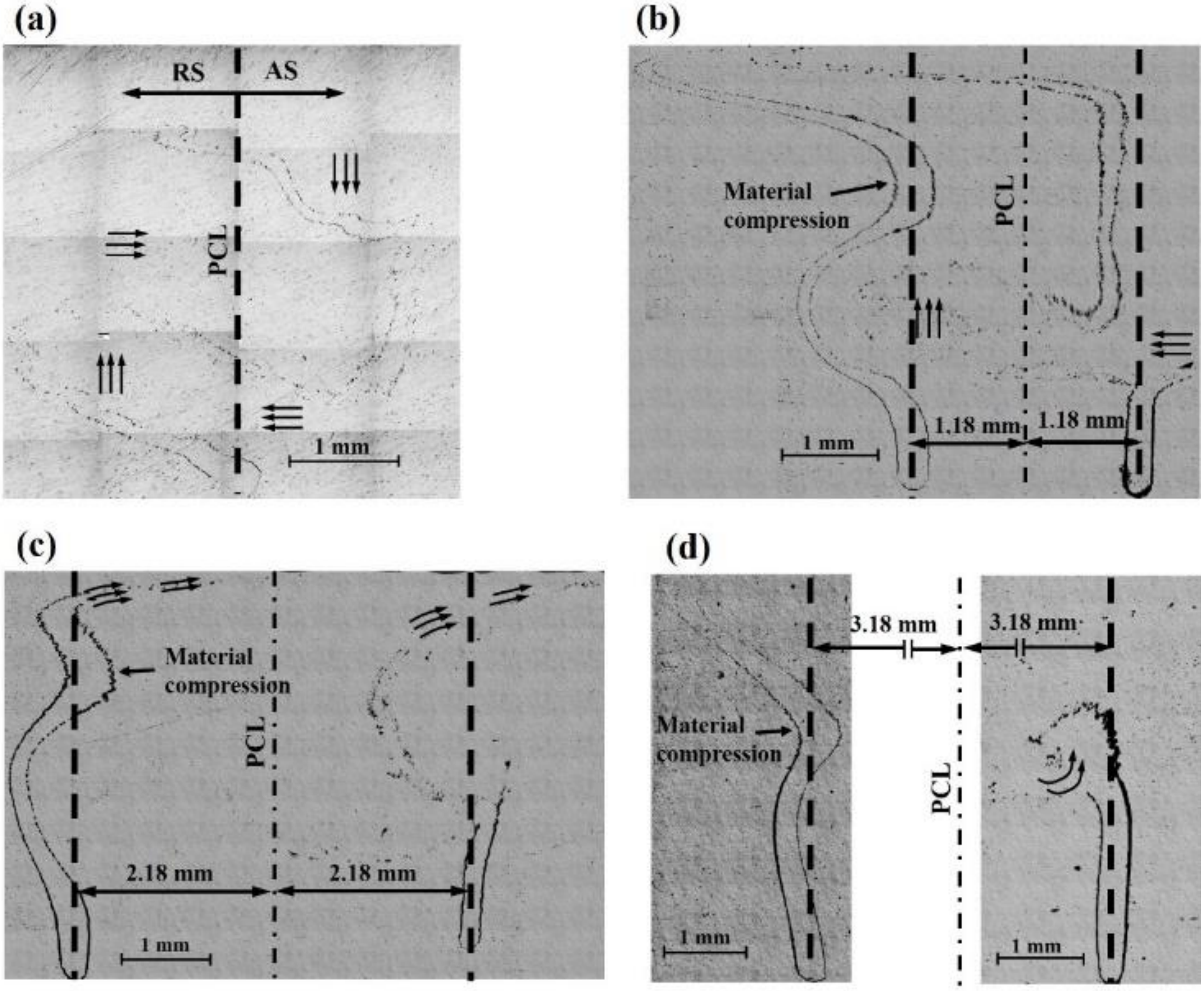

Fig. 5.4: Optical images of the tracer in the nugget zone after the FSW process, the initial position of the tracers were; a) at PCL, b) at 1.18 mm from PCL in AS and RS, c) at 2.18 mm from PCL in AS and RS, and d) at 3.18 mm from PCL in AS and RS.

The tracer displacement with respect to pre-process tracer positions is explained in following sub-sections.

i) ***Tracer placed at PCL:*** tracer is not continuous and broke at multiple locations, which suggest that the material movement was severe at the PCL. In fact, close to the shoulder the tracer almost disappeared. The tracer at PCL formed an inverted S-shaped trace around the PCL. At a distance of 1 mm from the top, the tracer was stretched horizontally in the RS. Between 1 mm and 3 mm from the top, the tracer was pushed downwards and stretched in the AS. Between 2.5 mm and 4 mm from the top, the tracer was lifted up and also stretched in the RS. The tracer was not displaced from its initial position at the tip of the tool pin.

ii) ***Tracer placed at 1.18 mm in the AS and RS from PCL:*** The mid-length of the tracer in the AS was displaced parallel to the pre-process position whereas the top and bottom parts were displaced up to RS. The top part of the tracer made a convoluted shape and the bottom part of the tracer material was fragmented. The RS tracer, however, made an inverted S-shaped curve similar to that at PCL but with smaller curvature. Up to 1 mm from the top, the tracer was stretched away from PCL. After that, the material accumulation can be seen (increment in the tracer thickness from 0.36 mm to 0.43 mm). From 2 mm to 4 mm the tracer was again stretched away from the PCL. This was due to material forced from the AS.

iii) ***Tracer placed at 2.18 mm in the AS and RS from PCL:*** the tracer displacement in the AS was quite different from the one at 1.18 mm. At the top, the tracer was stretched horizontally by the shoulder in the direction of the rotation. Below that the tracer was pushed downward and inward. The same material flow can also be seen in Fig. 5.3a. The tracer in RS, however, showed similar displacement as the tracer placed at PCL and 1.18 mm in RS. Though the curvature is quite small now. The top portion of the tracer got stretched from RS to AS by rotating shoulder.

iv) ***Tracer placed at 3.18 mm in AS and RS from PCL:*** the tracer at 3.18 mm in AS was thoroughly mixed up to 1 mm depth (shoulder affected zone) in the stir zone. The material was pushed downward in the nugget zone. The tracer in RS at the 3.18 mm distance from PCL, was pushed out from the stir zone at two locations. Near the shoulder, the tracer experienced more deviation as compared to the one close to the pin tip. Both tracers (3.18 mm RS and AS) showed one similarity, the material accumulation occurred at the same depth from the top surface. This accumulation occurs at the location where the shoulder flow and pin flow interact [60]. The tracer material flow observed in Fig. 5.4, indicate that the degree of material mixing in the RS is much lower than the PCL and AS material.

Figs. 5.3 and 5.4 provide the information about vertical mixing of the material in the nugget zone. Close to the shoulder, the material from the RS was transported to the AS occupying the space on the AS. FSW is a constant volume process and the shoulder, pin and un-deform base material form an extrusion die and restrict the flow path, the transport of the material from RS to AS by the shoulder cause the movement of the material from the top of the AS to the bottom. When closer to the tip of the pin, the material transport is restricted by un-deformed material therefore, material flow towards RS and then toward top.

Fig. 5.5 summarizes the PCL and RS placed tracer displacement from their original positions after the process. From Fig. 5.4, quantitative displacement of the tracers can be seen and it is observed that the tracer which was placed at PCL showed maximum displacement on both sides (~2 mm on RS and ~1.5 mm on AS) whereas, the tracers positioned at RS did not cross PCL. The momentum of the material displacement should decrease with radial distance from PCL, hence the depth of the curves found to decrease with radial distance from PCL. The topmost position of all tracers experienced large displacement.

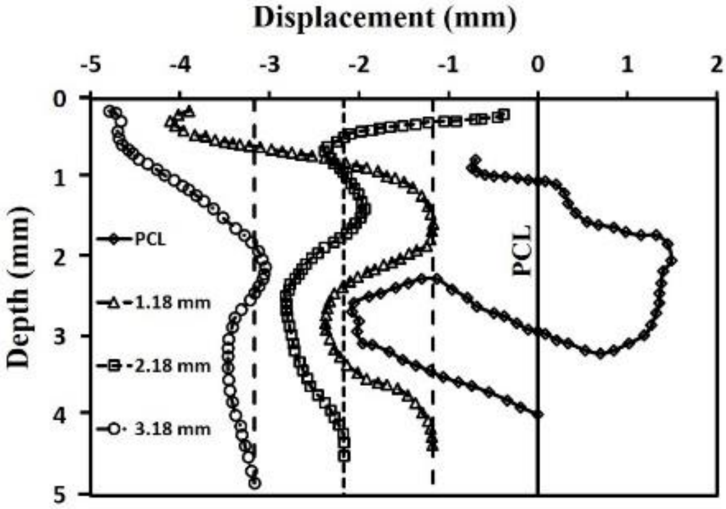

Fig. 5.5: Summarized the tracer displacement as shown in Fig. 5.4, placed at PCL, 1.18, 2.18 and 3.18 mm RS, from their original positions (vertical lines shows the mid-plane of the un-deformed tracer).

5.2 Strain

Fig. 5.6 shows the variation in the thickness strain with the depth of the tracer. Thickness strain (logarithm ratio of tracer thickness) was calculated from the measurements of tracer thickness. The thickness strain is defined by Eq. (5.1).

$$thickness\ strain = ln\left(\frac{d_0}{d}\right) \tag{5.1}$$

where d_o and d are pre-processing and post-process thicknesses of the tracer. Positive and negative values indicate stretching (thinning) and accumulation (thickening) of the tracer material, respectively. Thus, stretching of tracer indicates tensile strain and accumulation of tracer indicate compressive strain.

The processed zone can be divided into three parts, top (up to 1mm depth), middle (1-2 mm depth) and lower (2-4 mm depth). The top part material was highly stretched by the tool shoulder. Thickness strain (tensile) found to decrease from top to 1 mm depth. In the middle, thickness strain (compressive) was found to increase then decrease (in magnitude) with the depth.

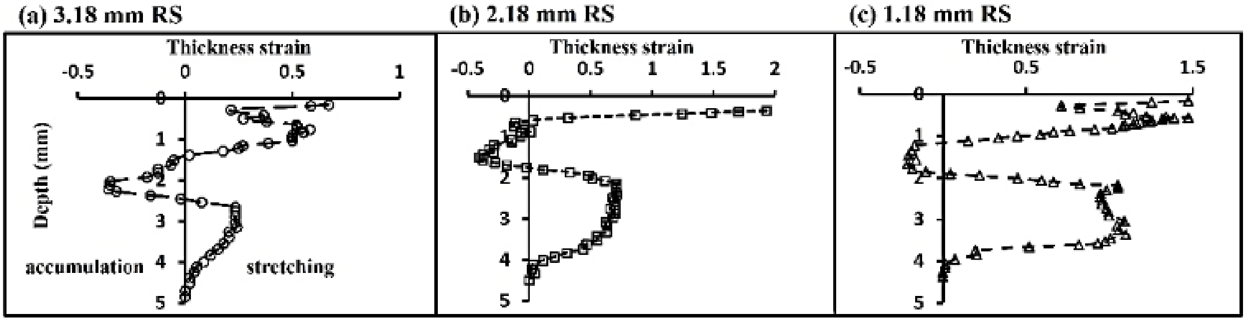
(a) 3.18 mm RS
(b) 2.18 mm RS
(c) 1.18 mm RS

Fig. 5.6: Thickness strain measured from initial and final thicknesses of the tracer. The tracers were placed in RS at a) 3.18 mm from PCL, b) 2.18 mm from PCL and c) 1.18 mm from PCL.

In the middle, the material experienced pressure from the top due to normal force exerted by the shoulder and from the bottom by displaced material (Fig. 5.3b). Hence, in this part, the material accumulated indicating compressive strain. Thickness strain (tensile) in the lower part (2-4 mm depth) was found to increase and then decrease (in magnitude) with depth. The tracer at 2.18 mm in RS from PCL exhibited maximum thickness strain (~2) in the top part. Thickness strain of the AS tracers cannot be measured due to a high degree of mixing in the nugget zone.

5.3 Discussion

From the observations elaborated in the section 5.1, three material flow movements are deduced; i) rotation around tool pin of the material collected from L-A side, ii) the downward push of the material by the tilted shoulder, in the cavity created at the back of the traversing tool, iii) extrusion and deposition of the material layer by layer from leading side via retreating side to trailing side.

To understand material flow, Fig. 5.7 shows resolved forces acting on the plasticized material at the back of the tool. F_d is the tangential force acting on the material due to rotating tool. Needless to say, its direction keeps changing with the location. F_g is normal force applied on the plasticized material in the direction of the tilt. Further, F_g can be resolved into two components, forward force i.e. $F_g \sin\alpha$, and downward force i.e. $F_g \cos\alpha$, as shown in Fig. 5.7. $F_g \cos\alpha$ forces material downward whereas the forward force $F_g \sin\alpha$, forces the rear plasticized material toward the tool pin, AS tracer position in Fig. 5.1. The three material movements are discussed one by one.

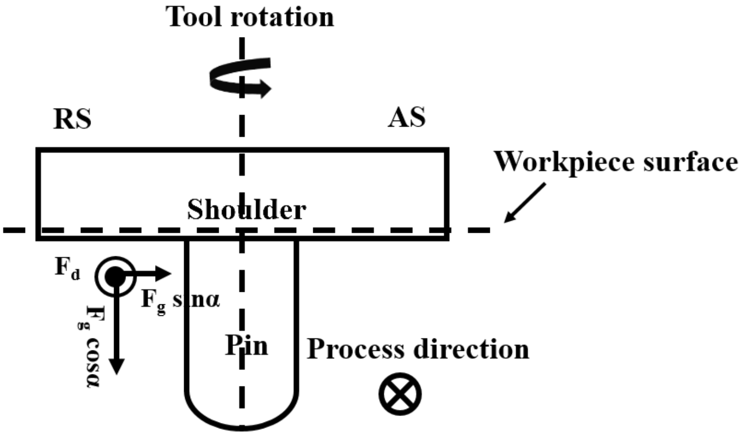

F_d: drag force, perpendicular to the plane of paper
Fg sinα: forward force
Fg sinα: downward force
α: tool tilt angle

Fig. 5.7: Forces acting on the material during the FSW process.

i) ***Rotation around tool pin*****:** material rotation around the tool pin is primarily due to the drag force F_d exerted by rotating shoulder and pin. Before start of the linear traverse of the tool, the material keep rotating with the tool rotation. However, combining rotation with the traverse motions of the tool, forces material entry and exit in the rotational zone [110]. To understand the material flow, the area around the pin is divided into four sides i.e. leading-advancing (L-A), leading-retreating (L-R), trailing-retreating (T-R), trailing-advancing (T-A) sides. The material in L-A side entered in the rotational zone and experienced thorough mixing in the nugget zone

(AS tracer in Fig. 5.4 b, c and d) before its exit from T-A side as shown in Fig. 5.8a and supported [98]. The rotational zone is wider near the top surface due to the effect of the rotating shoulder and its effect decreases with an increase in depth as shown in Fig. 5.8b. Nandan et al. [72] showed the same effect in terms of material viscosity due to higher temperature attained in the rotational zone. In T-A zone, the material exit from the rotational zone in a large amount due to plunged shoulder surface in the TS, as shown in Fig 5.8b. This exited (deposited) soft material from the rotational zone is forced to flow in a vertical motion, as shown in Fig. 5.8c.

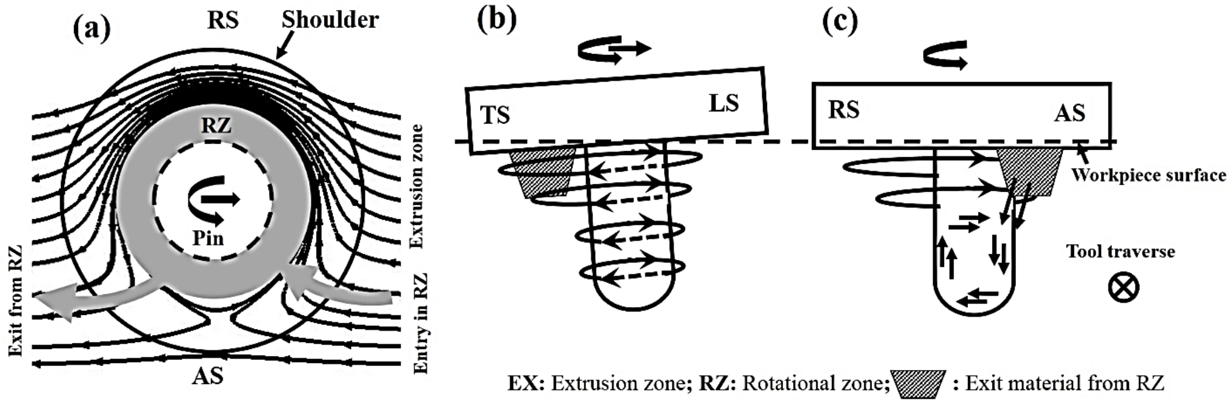

Fig. 5.8: Schematic of material flow during the FSW process; a) material flow around the pin in the horizontal plane, b) material flow around the pin along its length and, c) material flow in vertical plane at the TS.

ii) ***Downward push of the material*****:** one of the most important material flow characteristic is vertical flow which is responsible for filling the cavity at the back of the tool pin. In absence of this flow a defect called tunneling defect may occur. This flow is also responsible for formation of so called onion ring in the nugget zone. The material after exit from the rotational zone (shown in Figs. 5.8b and c) experiences the component $F_g \cos\alpha$ of the normal load and the drag force due to rotating shoulder. However, $F_g \cos\alpha$ alone does not explain the material movement in the vertical plane from the edge of the pin in AS tracers placed Fig. 5.1. The material from rotational zone, experiences drag force from the rotating shoulder which then move toward AS and flow downward in the cavity left behind by the traversing pin. The flow occur under the constraint imposed by the rotating shoulder, pin and relatively hard surroundings. The constraint imposed by different bodies exert a torque on the soft material and forces it to flow downwards in AS and upwards in RS. The surrounding hard material act as a pivot to the vertical rotation. The situation herein can be compared with the coupled bevel gear arrangement, as shown in Fig. 5.9. The extent of vertical movement will be decided by the rotation speed and weld pitch. At lower rpm the vertical motion is expected to be sluggish. It will be interesting to study material flow in the recently developed stationary shoulder friction stir welding [151, 152]. Since there is no contribution of a rotating shoulder on heat generation and drag force, the vertical flow is expected to modify.

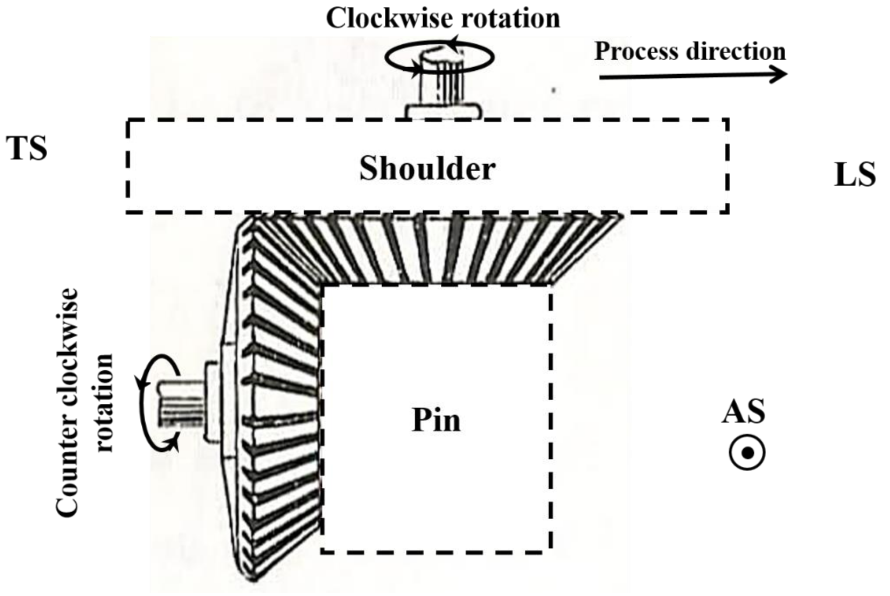

Fig. 5.9: Schematic of material flow in horizontal plane near the top surface and vertical plane at the TS, alike a bevel gear.

iii) ***Extrusion and deposition of the material layer by layer*****:** this is a very well-studied flow characteristic during the FSW. A large number of studies using tracer in metallic materials and plasticine showed layer by layer extrusion of material in the RS. Contrary to the results reported with tracer of high melting point material embedded in Al, in the present work, the backward movement of the tracer was quite different. The curvature of the tracer was equal to that of the pin wherein Cu was used as tracer material in Al [85]. The curve started from pin edge in RS to pin edge in AS. It appears that high melting point tracer material flowed with the initial high rotational drag force but did not follow the plasticized material movement in the wake of traversing pin. Since the tracer in the present work had same mechanical and physical properties the flow was truncated at the PCL. The truncated flow might be due to two reasons, first due to the forward linear motion of the tool pin and second due to vertical flow of the material in the AS, as explained in the previous section. So material dragged from the RS was either pulled with the tool pin or it experienced downward flow in the AS and hence its movement from RS to AS was truncated at PLC.

5.4 Summary

Tracer insert technique was used to study material flow behaviour and strain during the FSW process by using tracers of the same material (5083 aluminium alloy). The material flow was explained by resolving forces acting due to titled shoulder and material confinement due to cold surroundings.

It is observed that shoulder driven flow forced material from retreating to the advancing side at the trailing side of the tool, where material deposition takes place. This deposited material was pushed downward by moving tool shoulder. The downward material flow was pushed toward RS up to the tip of the pin and then it experienced a sharp change in the direction of RS. The material then flowed upward in the RS. This downward and upward flow thoroughly mixed the material in the nugget zone. AS material experienced a high degree of the mixing and RS material did not experience the mixing of the same order. The RS material feels tensile and compressive strain near the top surface of the workpiece and mid-length of the pin, respectively.

In this work, the observed material flow was different from the past literature. In literature it was reported that in the retreating side at the mid-depth of the tool pin, the tracer was deposited behind the tool pin and maximum deviation was approximately equal to pin diameter. However, in the present study the backward deviation was equal to half of the pin diameter. Moreover in the retreating side, the dragging of the tracer with the tool traverse was reported to start from the edge of the pin [83, 84, 85], whereas in present work the tracer showed

CHAPTER 6

MATERIAL FLOW ANALYSIS USING PIV TECHNIQUE

In this chapter, the experimental attempt is made to provide the substantial details of in-situ material flow visualization around the tool pin in FSW using particle image velocimetry (PIV) technique. The experiments were performed for a traverse speed of 50-140 mm min^{-1} and for the rotational speed of 75-425 rpm.

6.1 Material flow characteristics

The detailed procedure and working principle of PIV has been discussed in Chapter 4. A sample of the raw image obtained from PIV system is shown in Fig. 6.1. In this image, white particles are the tracer particles. The displacement of tracer particle at two subsequent times provides the information about the material flow. For material flow and strain rate analysis on an average 150-200 pairs of images were analysed. The analysis of these images yields the time-displacement history of tracer particles. It is further used to obtain the important material flow characteristics such as flow pattern, velocity and strain rate around the tool pin, as discussed flow.

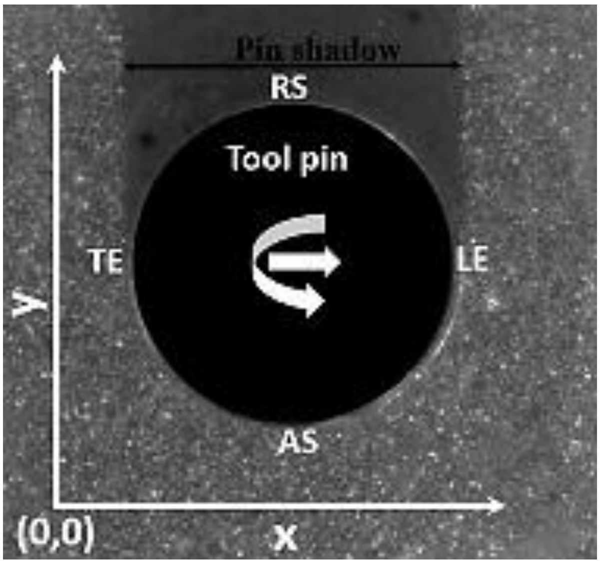

Fig. 6.1: Representative image of PIV at mid-length.

.

6.1.1 Flow pattern

Fig. 6.2 shows the material flow behaviour or streamline patterns at the mid-length of the tool pin at 300 rpm and 50 mm min^{-1}. Due to the movement of the pin in the processing material, a deformation zone is formed around the tool pin. The deformation zone can be divided in two types of flow zones, i) close to the pin surface is rotational zone (RZ, plastic flow regime) and, ii) next to the rotational zone is transitional zone (TZ). The rotational zone (grey colour ring) is symmetric (approximately 1.2±0.1 mm width) around the pin. Fig. 6.2b shows the streamlines in rotational zone around the pin. Due to the rotating pin, material adjacent to pin rotates in a circular motion in the rotational zone. Simultaneously, the translation of pin in leading direction forms a shearing layer around the rotating zone, which detaches from rotational zone in trailing-retreating side during each revolution. Such attachment and detachment of shear layers develop the transitional zone. The material in the rotational zone enters between advancing-leading sides of the pin (shown by green colour streamlines in Fig. 6.2a). The material then rotates around the pin several times (shown in Fig. 6.2b) before its exit between trailing-advancing sides (shown by red colour streamlines in Fig. 6.2a). Furthermore, the size of the rotational zone is expected to be highly dependent on the tool rotational/traverse speeds and measurement location, i.e., higher rotational speed yields larger rotational zone. However, the rise in the size of the rotational zone cannot be monotonic and will depend on change in the flow conditions from sticking mode to slipping mode at higher rotational speeds.

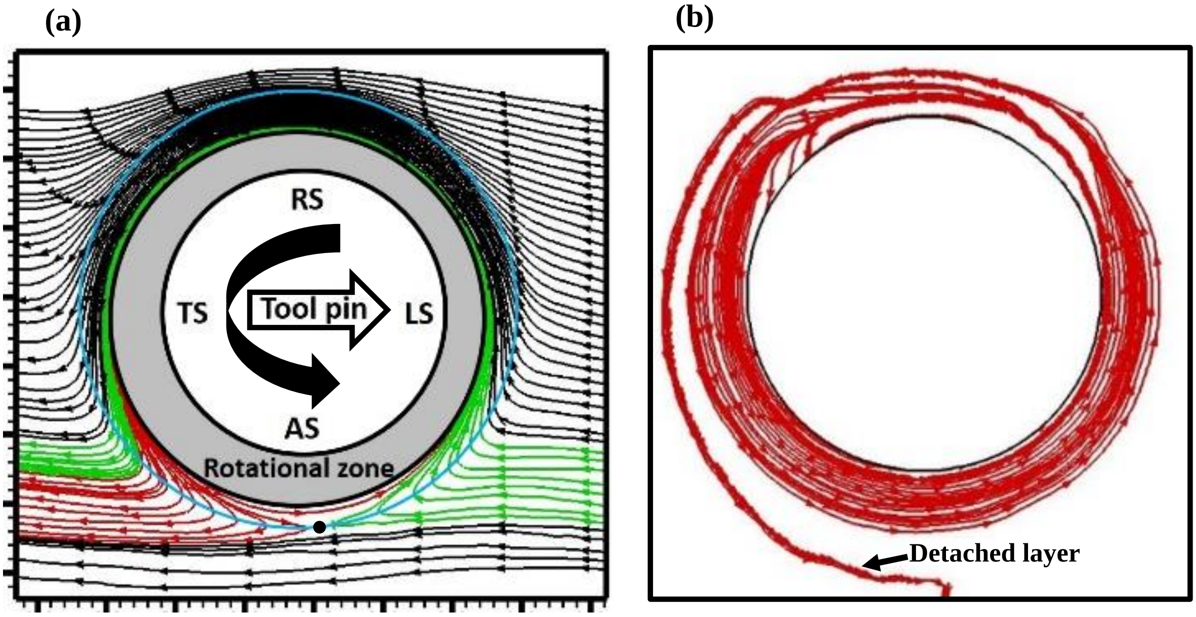

Fig. 6.2: Streamlines around the tool pin, a) in transitional zone, b) in rotational zone.

Outside of the rotational zone, there is transitional zone (outer edge is shown by sky blue colour circle in Fig. 6.2a). It starts from the outer edge of rotational zone and ends with the static material. The static material beyond the transition zone remains unaffected by the pin. In this zone, material flows from LS to TS, as shown by streamlines in Fig. 6.2a. Transitional zone appeared to be non-circular regime. The ratio of radial thickness in RS and AS in the transitional zone, say z_t, is observed to be approximately 1.5. This shape asymmetry is closely consistent ($z_t \sim 2$) with the experimental work of Guerra et al. [82]. Our findings are further qualitatively verified by the computational investigation of Schmidt et al. [83], who computed zero width on AS and wider on RS.

The streamline patterns observed in the transitional zone (Fig. 6.2a) are not symmetrical about the rotational zone. In this zone, the density of green colour streamlines is not same at leading and trailing sides. For example, the streamlines (green colour) are sparse between AS and LS whereas, these are dense/compact between TS and AS (back of the pin). As the streamlines represent the tangent to the local velocity vectors, their density/sparsity, in turn, suggests the nature of the flow. Flow rate is expected to be slower where streamlines are far apart and faster where they are closer. This indicates that material flow velocity at the trailing side of the pin is slightly higher than that of leading side, due to the low pressure zone created at the back of the pin. The red colour streamline are sparse at the trailing-advancing side, where the rotational zone material deposition takes place. Such a material deposition or flow stagnation, was also reported by Morisada et al. [50]. Further, at the AS, opposing material flow, due to rotation and traverse speeds, yields the stagnation point, SP (black colour spot between red and green colour streamlines separation point at the AS in Fig. 6.2a), further described in the next section 6.1.2 (in Fig. 6.7). In contrast to asymmetrical streamlines in present investigation, Long and Reynolds [93] numerically reported that the streamlines are symmetric about the transverse direction around the tool pin. They reported a bifurcation point in the transitional zone on AS. At the bifurcation point, material divides into two streams and give rise to stagnant material. The asymmetry in the flow patterns is clearly expected due to the combined effect of rotation as well traversing of the pin, in addition to the varying viscosity of weld materials. This asymmetry can subsequently be supported by the three-dimensional numerical investigation of Nandan et al. [72, 74]. The contrasting feature shown in numerical results [93] may appear due to various factors, such as two-dimensional geometry, accuracy of results, computational grid and other simulation parameters, approximation of physical boundary conditions, etc.

6.1.2 Flow velocity

Fig. 6.3 show the velocity field of the material around the pin at 300 rpm and 50 mm min^{-1}. The velocity vectors in the interested region around the pin are shown in Fig. 6.3a. Fig. 6.3b shows the velocity vectors in the leading, trailing and advancing sides. Retreating side velocity vectors are not in arranged manner as shown in Figs. 6.3a and 6.3b, because at the backside of the pin, there is shadow of the pin formed by laser light. In shadow region, the tracer particles are not illuminate in proper way, hence CCD camera unable to capture the particles motion.

As observed in Fig. 6.2, various zones of material flow are formed. The analysis of these zones, is further extended in terms of the local flow velocity. Since the rotational speed of pin is a major driving force to create the flow, the local velocity (V) of material flow is scaled with the peripheral velocity (V_R) of the tool pin. The velocity (%) is then calculated as Eq. (6.1).

$$V_{\%} = \frac{V}{V_R} \times 100 \qquad \text{where } V_R = \omega r \qquad (6.1)$$

where, r and ω are the radius and angular velocity of the tool pin, respectively.

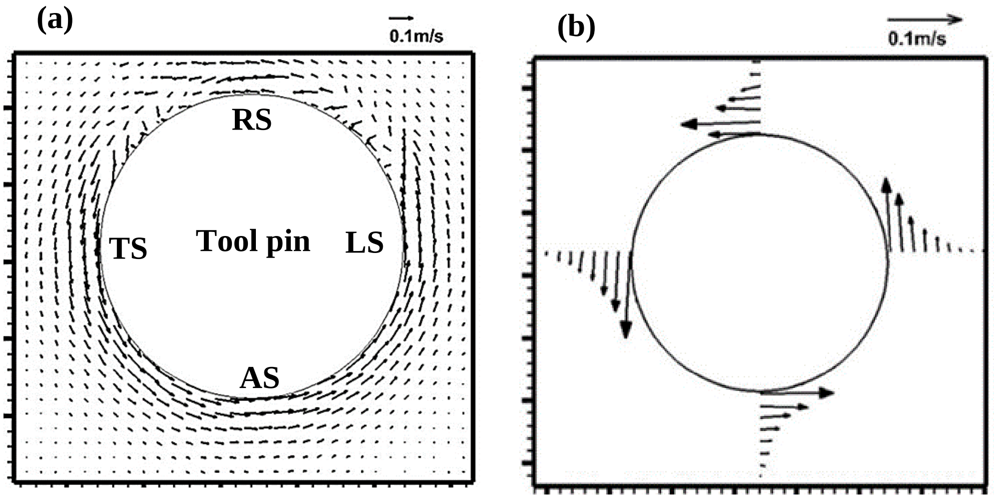

Fig. 6.3: a) Material flow velocity vectors around the pin, b) velocity vectors at AS, RS, LS and TS.

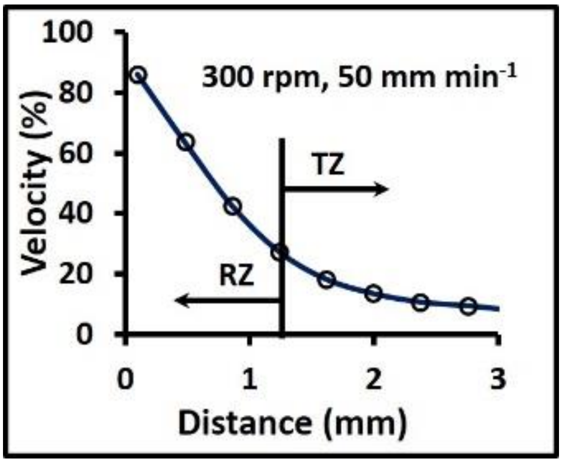

Fig. 6.4: Leading side velocity profile.

Fig. 6.4 shows the leading side material flow velocity (%) profile with the radial distance from the pin surface (0.1 mm from pin surface), for the pin peripheral velocity ($V_R = 0.128$ ms^{-1} corresponding to 300 rpm). The maximum flow velocity is observed in the vicinity of the pin and decreased with increasing distance from the pin surface, due to viscous dissipation. The maximum velocity drop is observed within rotational zone or 1.2 mm from the tool pin periphery. During the post-processing of PIV results obtained from our experimental setup, the closest possible distance from the pin surface is ~0.1 mm to obtain the flow field. The maximum velocity is found to be ~85% of the pin peripheral velocity, closest to the pin surface. Theoretically, the velocity is expected to be ~100% at the surface of the pin. However, it will practically not be possible to achieve the maximum possible velocity of material flow due to frictional and other losses. These losses shall be depending on the rotational and traverse speeds of the tool pin, surface properties of the tool and the type of weld materials, as evident from the previous studies. For instance, the maximum flow velocity was observed to be ~75%, ~60%, ~25%, and ~70% at mid-length of tool pin for the following weld conditions (Al 6061, 344 rpm and 95 mm min^{-1}, 0.65 sticking coefficient), (SS, 300 rpm and 101 mm min^{-1}, 0.7 sticking coefficient), (MS, 450 rpm and 25 mm min^{-1}, 0.8 slipping coefficient), and (Al 1050, 600 rpm and 400 mm min^{-1}) by Nandan et al.[72], Nandan et al.[73], Nandan et al.[74] and Morisada et al.[50], respectively. These works also suggest the strong role of the surface characteristics, i.e., slipping or sticking, between workpiece and tool surface.

Further, the variation of maximum velocity with rotational and traverse speeds of the tool pin is also analysed. Fig. 6.5 depicts the relation of maximum velocity with rotational speed (N = 75 – 425 rpm) at three traverse speeds (50, 90 and 110 mm min^{-1}). A linear variation in the velocity is recorded with increasing rotational speed, irrespective of the traverse speed of the tool.

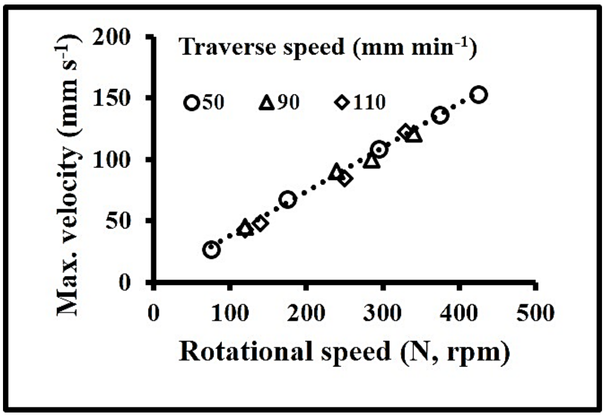

Fig. 6.5: Velocity variation with rotational speed, at different traverse speeds.

Further, the velocity variations along the radial distance on all four sides (RS, LE, TE and AS) have shown in Fig. 6.6. To see the variation in the material flow velocity around the pin, an experiment is performed at low rotational speed and high traverse speed (130 rpm and 140 mm min^{-1}). It is noticed that the material flow velocity around the pin is not uniform. On the RS, the material flow velocity is slightly higher than that of AS at the same distance from the pin surface. Similar behaviour is also reported in the literature [153]. In the present work, the difference in

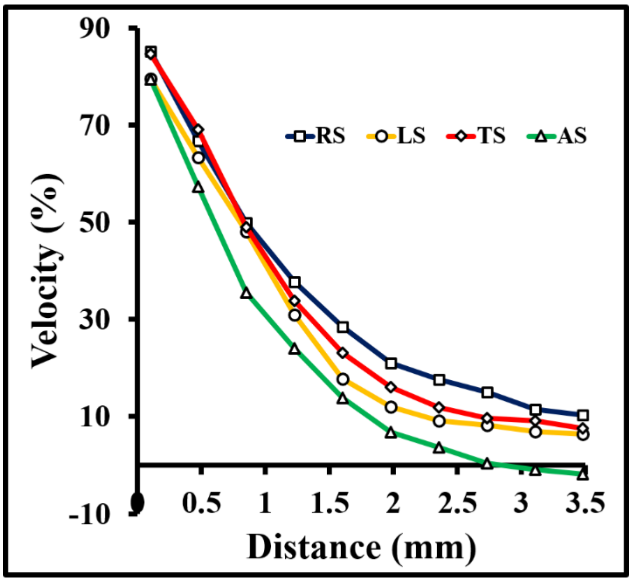

Fig. 6.6: AS, RS, LS and TS velocity profile at 130 rpm and 140 mm min^{-1}.

the velocities in RS and AS is found to be approximately double of the traverse speed. The differences in the RS and AS velocity is explained with the help of schematic shown in Fig. 6.7. In Fig. 6.7a, material traverses (velocity =V_T) from right to left, and the tool pin rotates (velocity = V_R) in anticlockwise direction. The stationary observer (rotating tool) measures the velocities as ($V_R + V_T$) at RS and ($V_R - V_T$) at AS. Hence, the difference in the velocity at RS and AS is $2V_T$. Furthermore, a minor difference in the velocities at LS and TS is also observed. These differences may be attributed to the experimental precision or image capturing directions. The low pressure created at the back of the tool pin by traverse is likely to be one of the reasons for higher velocity at TS than that at LS.

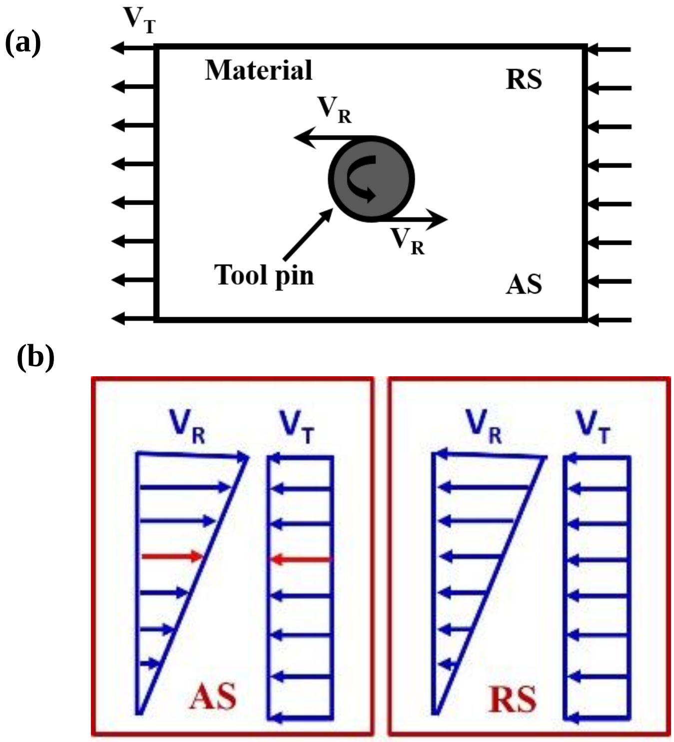

Fig. 6.7: a) Schematic of material flow from right to left, past anticlockwise rotating tool pin and b) schematic of velocity vectors at AS and RS of the tool pin.

It should also be noted that the AS material flow velocity profile is shown negative values after 2.75 mm radial distance from pin surface (Fig 6.6). The rotational velocity (V_R as shown in Fig. 6.7b) is decreased with increase in radial distance and after a certain distance from pin surface, where the magnitude of the both velocities rotational (V_R) as well as traverse (V_T) become equal and opposite, yields the stagnation point, SP, where the resultant material flow velocity is become zero (in Fig. 6.7b, red colour vector represent stagnation point).

6.1.3 Strain rate

The strain rate was calculated from two-dimensional velocity field obtained from the post-processing of PIV images. Fig. 6.8 shows the strain rate profile around the pin in radial direction, at rotational speed of 300 rpm and traverse speed of 50 mm min^{-1}. The strain-rate is found to first increase and then decrease in the rotational zone. In the transitional zone strain rate is found to decrease with distance. The maximum strain rate (i.e., ~100 s^{-1}) is observed at ~0.47 mm distance from the pin surface at AS.

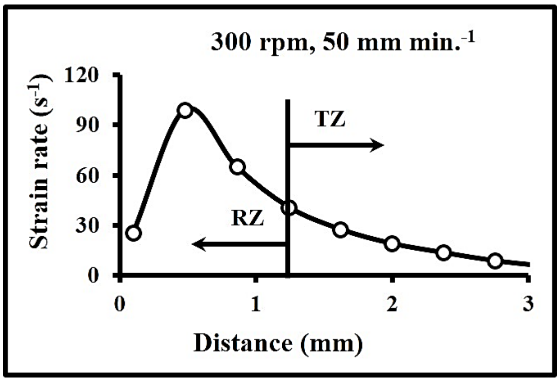

Fig. 6.8: Variation in strain rate with distance from pin surface.

Further, the variation of maximum strain-rate with rotational and traverse speeds of the tool pin is analysed. Fig. 6.9a depicts the relation of maximum strain rate with rotational speed (N = 75 – 425 rpm) at three traverse speeds (50, 90 and 110 mm min^{-1}). A linear variation in the strain rate is recorded with increasing rotational speed, irrespective of the traverse speed of the tool. The present experimental data is fitted into a linear predictive correlation expressed in Eq. (6.2), over the range of conditions covered herein.

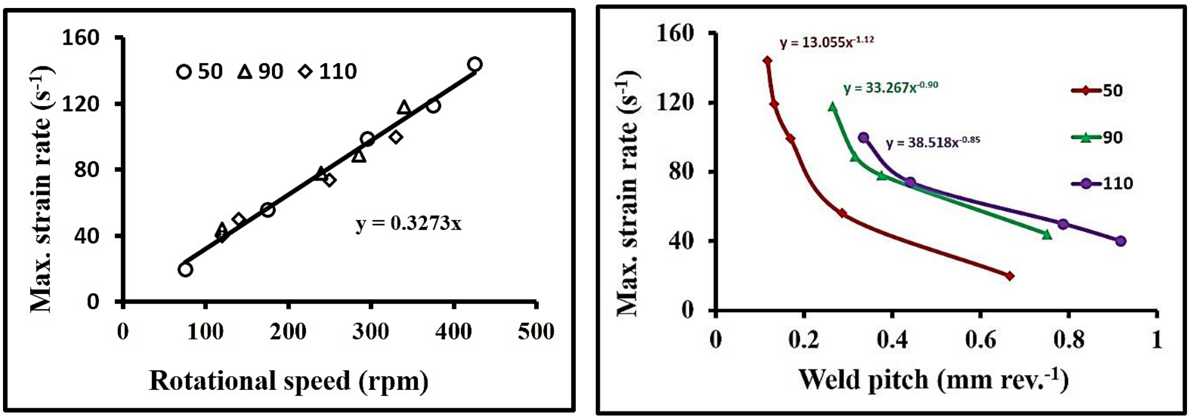
(a)

(b)

Fig. 6.9: Variation in strain rate at 0.47 mm from pin surface, a) with rotational speed and b) with weld-pitch.

$$\dot{\gamma} = 0.3273N \tag{6.2}$$

where $\dot{\gamma}$ and N are the maximum strain rate (at 0.47 mm distance from pin surface) and rotational speed (in rpm) of the tool pin, respectively.

While the experimental values are obtained for intermediate rotational speeds, the relation can be used for the prediction of maximum strain-rate at the larger rotational and/or traverse speeds. Further insights of the strain rate behaviour are presented in terms of weld-pitch (tool traverse per revolution, mm per rev.) in Fig. 6.9b. The strain rate follows power-law relationship with weld- pitch, as expressed in the Eq. (6.3).

$$\dot{\gamma} = kP^{\alpha} \tag{6.3}$$

where k and α are constants and P is weld-pitch. The value of constants k and α increase with increasing traverse speed of the tool pin. The strain rate is decline with increasing weld-pitch, irrespective of the traverse speed of the tool pin. Increasing traverse speed enhances the strain rate for a given weld-pitch. It suggests that for a given traverse speed, the minimum strain rate shall be encountered on increasing the weld-pitch. These behaviours presented herein are qualitatively similar to those reported in the literature [71].

Comparison of strain rate with existing literature

The summary of the existing literature on FSW shown in Table 2.1 suggests the dependence of the maximum strain rate on the welding materials and conditions, methodologies, etc. Keeping in mind such a complex dependencies of strain rate behaviour, a direct comparison of the present experiments with existing results is not possible. However, present results with existing results are plotted in Fig. 6.10 to ascertain the reliability of the present results within the bounds of FSW. Irrespective of the methodology used, the maximum strain rate increases linearly with rotational speed of the tool pin. For the discussion purpose, three trends lines L_1, L_2 and L_3 are shown in the Fig. 6.10 to represent the results of Chang et al. [51], Ammouri et al. [53] and present work, respectively. The present experimental results agrees well with numerical studies reported in the literature [76, 78, 79]. Furthermore, most of the computational data, except that of Frigaard et al. [71], lies close to the lines L_2 and L_3. The possible reason of the deviation of the values of Frigaard et al. (2001) may be high traverse speed used in their work.

On the microstructural basis, Chang et al. [51] observed that strain rate linearly increase with rotational speed (line L_1). On the other hand, relatively lower values of effective strain rate, i.e. 1.7 - 2.7 s^{-1}, are obtained by Masaki et al. [63] through simulation of the stir zone microstructure of 1050 Al using a combination of plane strain compression test and subsequent cooling. These lower values are probably due to difference in deformation conditions i.e. shear deformation present during FSW and plane strain compression. The studies based on the tracer techniques have shown wide range of the strain rates due to different weld materials used and different measurement locations, etc.

All in all, few general observations can be made as follows. The strain rates predicted in present study are very close to the reported computational results. The strain rate predicted from microstructural studies also follow linear relationship, however, the slope of the line is lower. On the other hand, studies based on plasticine show weak dependence of strain rate on the rotational speed [68]. Although strain rates achieved during FSW exhibit linear dependence on rotational speed, it is expected that at higher rotational speed, the rise in the strain rate will be low. Since at higher rotational speed, slipping between the tool pin and material or rise in the temperature may lead to lower strain rates. This is evident from the reported work on plasticine wherein high amount of slipping resulted in very low strain rates. In particular, the strain-rate is seen to be dependent on the types of the welding materials, rotational and traverse speeds of the tool pin, geometry and dimensionality of the analysis, techniques adapted, and surface characteristics of the tool pin, etc.

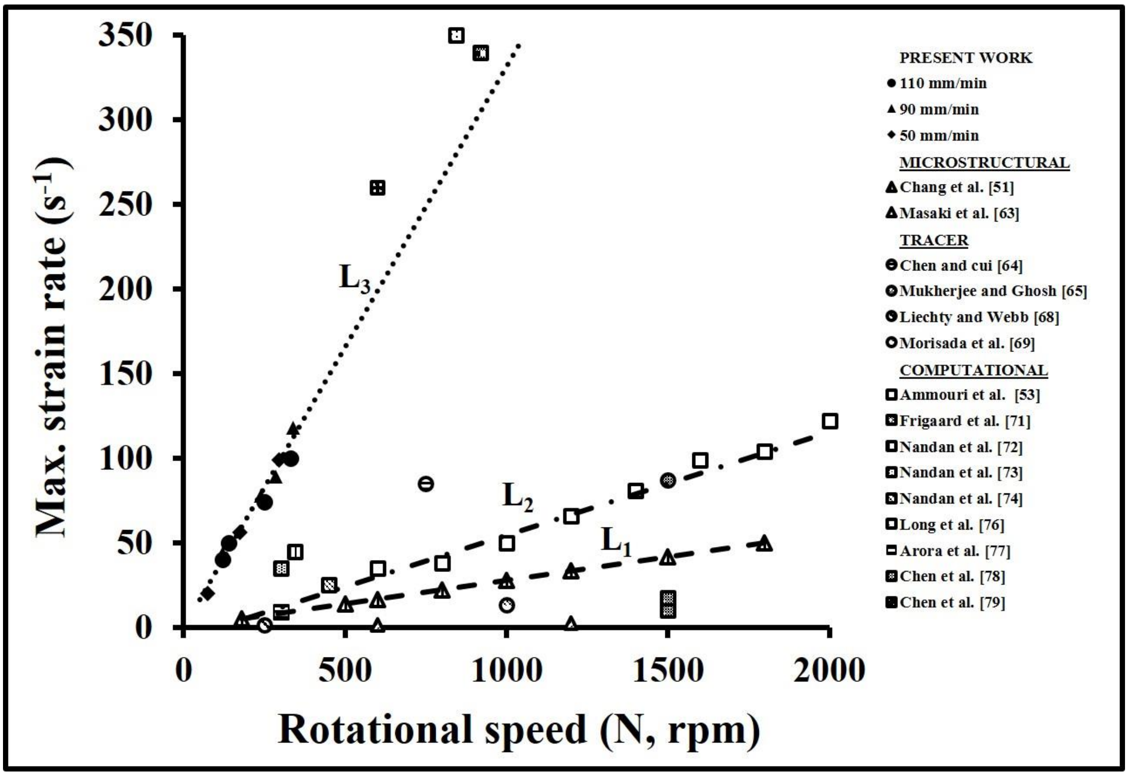

Fig. 6.10: Comparison of present values of maximum strain rate with the existing literature for various welding conditions.

Based on the outcome of the work and comparison of present results with the existing literature (Table 2.1 and Fig. 6.10), a novel approach of in-situ visualization by PIV technique can be utilized for the in-depth understanding of the material flow and strain behaviour during the FSW. It may prove to be useful in comparing material flow behaviour between tools with complex geometries.

6.2 Summary

The material flow and strain rate during the FSW was successfully visualized by PIV technique. The importance of the work lies in the fact that an instantaneous evaluation of the material flow during the FSW can be performed. The thermal behaviour of the process is considered as isothermally, without any heat generation or heat loss. The proposed method offers great potential in the development of different tool geometries and processing parameters by effective visualization of the material flow patterns. Two dimensional flow patterns were obtained using glass tracers in a transparent non-Newtonian fluid. The rotational zone was observed around the pin, leading-advancing side material entered in rotational zone. The material rotated around the pin several times before exit between trailing side (TS) and advancing side. The velocity was found to decrease from its maximum (85%) near the tool pin to stagnated material. The maximum strain rate around the pin periphery found to increase linearly with rotational speed, irrespective of the traverse speed. Predictive relations were developed to quantify strain rate variation as a function of rotation speed and weld-pitch.

MATERIAL FLOW ANALYSIS USING COMPUTATIONAL TECHIQUE

This chapter presents work on numerical simulation of friction stir welding process as two dimensional flow field. The numerical results were compared with PIV results presented in Chapter 6. A two-dimensional model was developed to conduct the numerical simulation of material flow around the tool pin in the FSW process. A commercial CFD code, COMSOL MULTIPHYSICS software was adopted to simulate FSW process for traverse speed in the range of 50-110 mm min^{-1} and rotational speed in the range of 75-425 rpm.

Since the rheological behaviour of the process materials plays an important role in the material flow during FSW, as discussed earlier, the experimenally obtained rheological parameters of the processing material were used as input in COMSOL. To ascertain the relaibility of the process input parameters, the viscosity profile obtained by using rheometer was compared with that obtained computationally by using COMSOL software in the Fig. 7.1. A good agreemnt between the two viscosity profiles gave confidence to gain more insights of the material flow during FSW process.

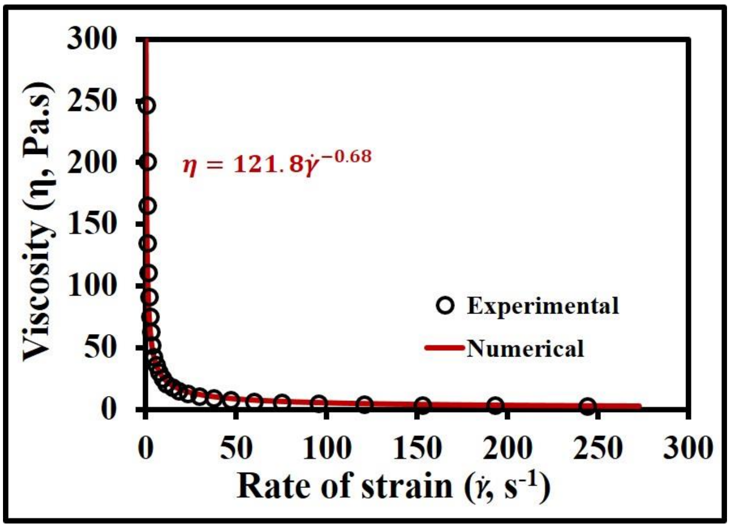

Fig. 7.1: Processing material rheology compared with numerical.

7.1 Velocity measurement

Fig. 7.2 shows the leading side velocity profiles at rotational speed in range of 75-425 rpm and traverse speed of 50-110 mm min^{-1}. At the pin surface, the material flow velocity is equal to the pin peripheral velocity which confirms that the material sticks at pin surface. The maximum velocity occurs at pin surface and decrease with an increase in the radial distance. The maximum drop in the velocity is observed within 1 mm distance from pin surface. It is observed that the tool rotation speed has significant effect on the velocity field.

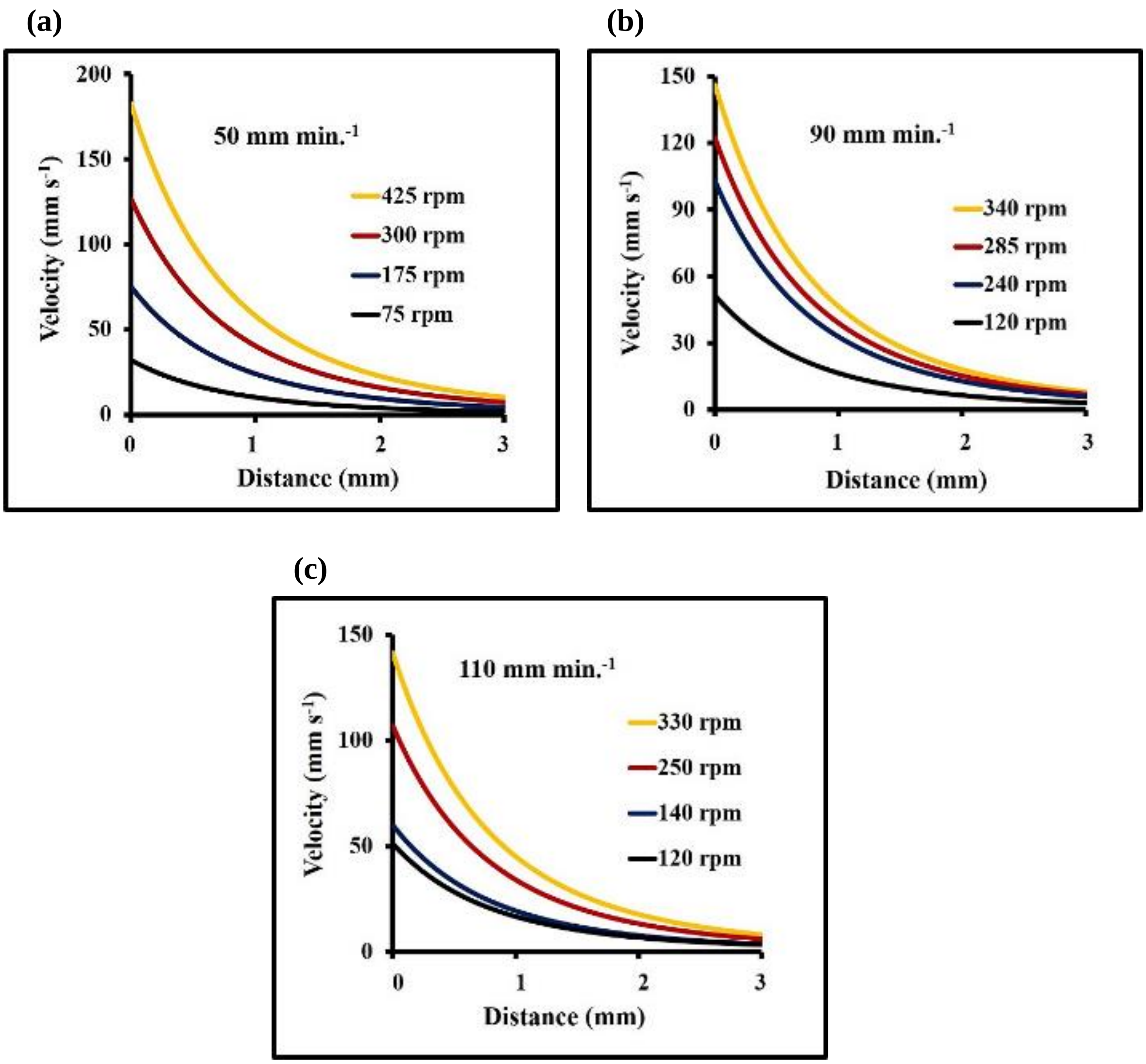

Fig. 7.2: Material flow velocity variation with rpm and radial distance from pin surface in the leading side of the pin at (a) 50 mm min^{-1}, (b) 90 mm min^{-1} and (c) 110 mm min^{-1}.

7.2 Strain rate

Fig. 7.3 shows the variation of strain rate with rotational and traverse speeds of the tool during the process. Close to the pin surface, a high strain rate was induced due to the high strain at the beginning of the material flow near the tool pin. In contrast, the drop in strain rate close to the pin surface (within 1mm from pin surface) was more, due to existence of large velocity gradients. After that, the strain rate decreases at slower rate. Further, the strain rate increases with increase in rotational speed similar to flow velocity.

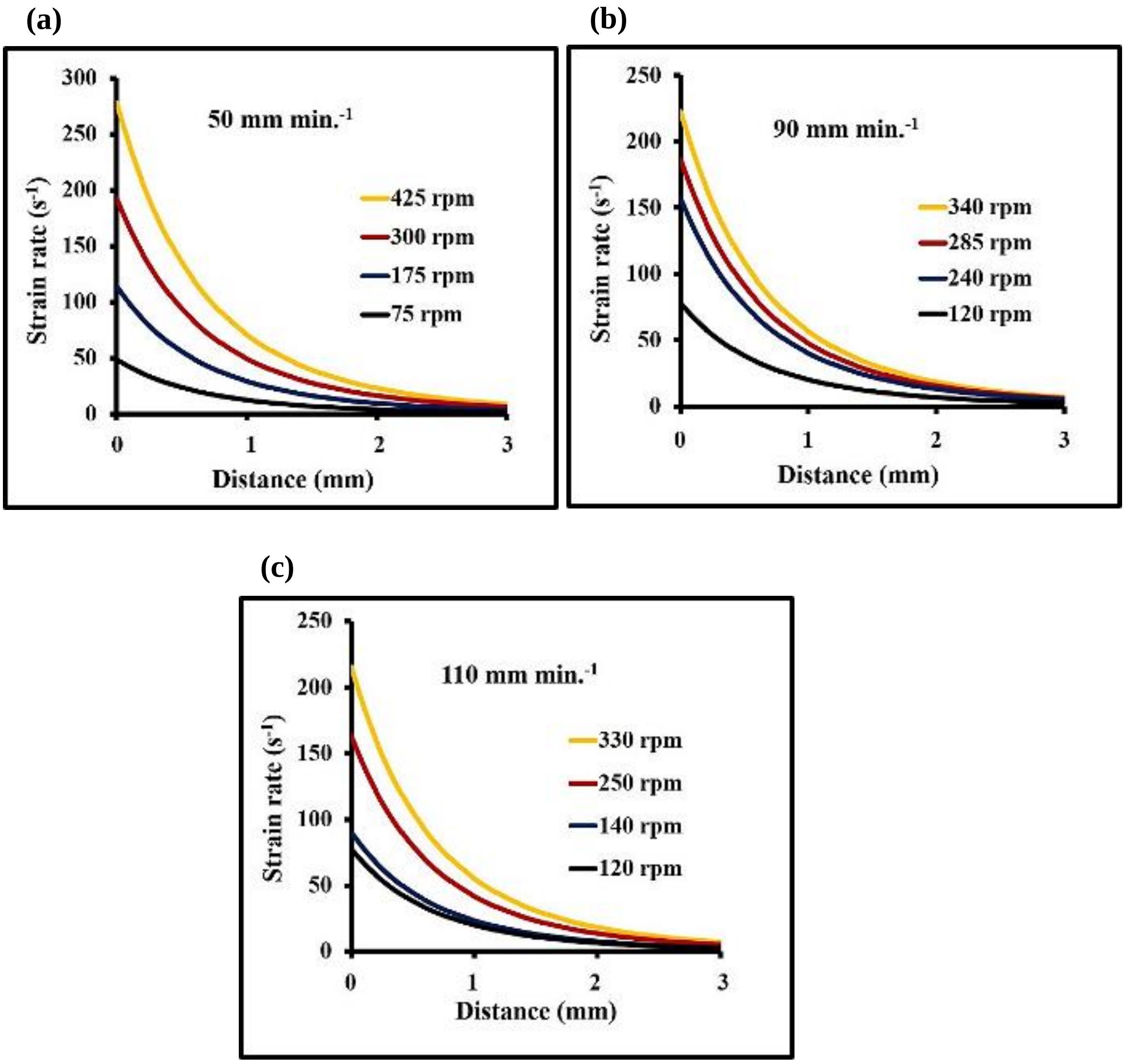

Fig. 7.3: Strain rate variation with rpm and radial distance from pin surface in the leading side of the pin at (a) 50 mm min^{-1}, (b) 90 mm min^{-1} and (c) 110 mm min^{-1}.

7.3 Comparison of PIV results

In this section, the results obtained from the PIV technique are compared with numerical simulation results.

7.3.1 Flow pattern

In Fig. 7.4, the comparison of computational and experiment flow fields around the pin surface is shown. It is noteworthy here that the experimental results have similarity in flow structure with the simulation work. In the numerical work, the rotational and transitional zones around the pin are wider compared to experimental. Furthermore, the stagnation point is slightly far away from the pin surface relative to experimental observations. The model quite accurately captured many real process characteristics such as velocity and strain rate, but it shows deformation zone slightly wider around the pin as compare to the experimental. In numerical simulation, extremely fine grid correctly captures the gradients developed around the surface and thus it may be one of the reason for wide deformation zone. Another possibility may the use of surface to fluid boundary condition based on the constant rotational velocity. Nonetheless, due to the stronger resolution in the numerical simulation, this aspect of wider deformation zone also seems to be correctly captured.

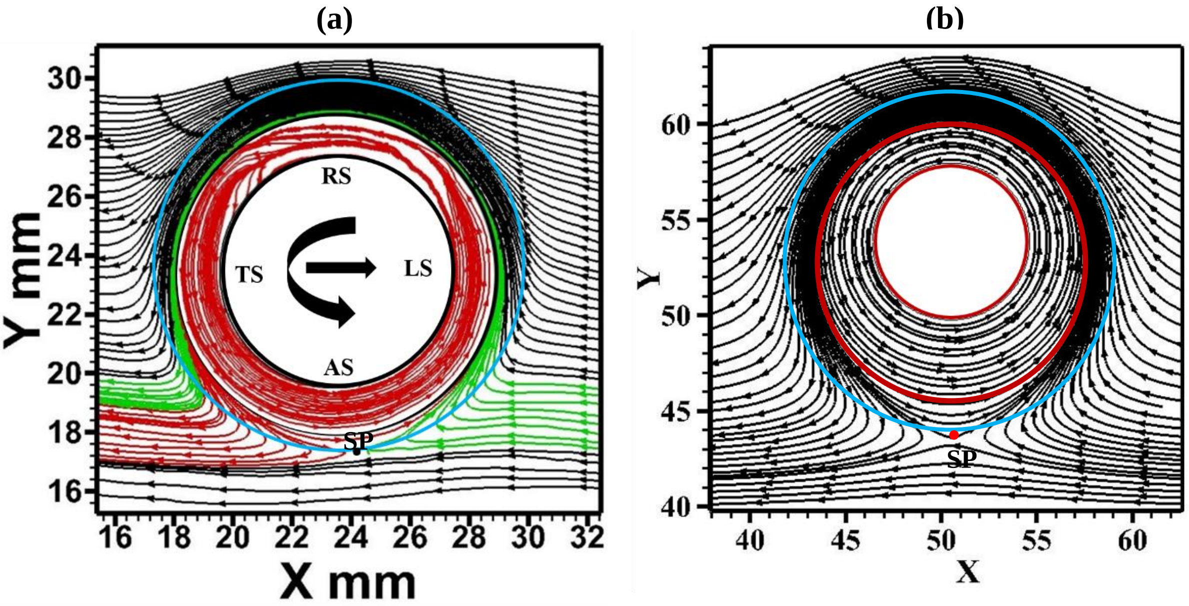

Fig. 7.4: Material flow field around the tool pin a) Experimental and b) Numerical.

7.3.2 Flow velocity

Fig. 7.5 compares the numerical with experimental values of flow velocity at 75-425 rpm and 50-110 mm min^{-1}. In general, both experimental and numerical observations show the similar

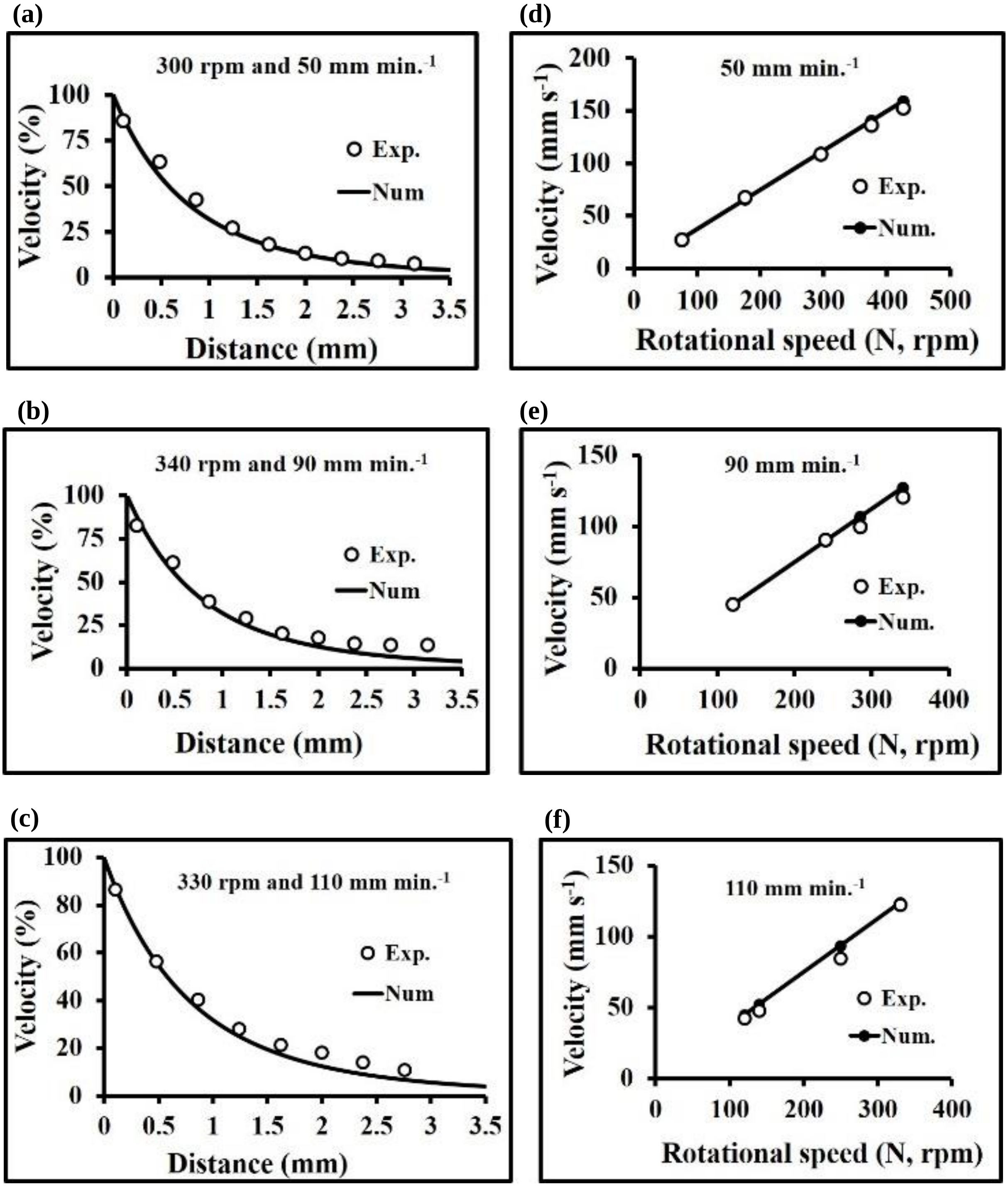

Fig. 7.5: Velocity variation with, a) radial distance at 300 rpm and 50 mm min^{-1}, b) radial distance at 340 rpm and 90 mm min^{-1}, c) radial distance at 330 rpm and 110 mm min^{-1}, d) rotational speed at 50 mm min^{-1}, e) rotational speed at 90 mm min^{-1}, and f) rotational speed at 110 mm min^{-1}.

trend of variation of velocity with processing parameters. The experimental results are seen to be very close to the numerical results.

Figs. 7.5 a-c show the velocity variation with radial distance from the pin surface at 300 rpm 50 mm min^{-1}, 340 rpm 90 mm min^{-1} and 330 rpm 110 mm min^{-1} respectively. The velocity continuously drops from 100% to 20% within 2 mm distance from pin surface, and maximum drop occur close to the pin surface. The insignificant variations in the experimental values are due to the experimental errors/precisions in PIV measurement [143], [147], [154].

Figs. 7.5 d-f show the variation in velocity at ~0.1 mm distance from pin surface with rotational speeds, rpm, at a given traverse speed, i.e., 50, 90 and 110 mm min^{-1}, respectively. The velocity increase linearly with rotational speed. All experimental points lies close to the numerical values.

Fig. 7.6 summarised the experimental flow velocity for all processing parameters (three traverse speeds and four rotational speeds) with numerical values. The filled symbols represent the numerical value whereas open symbols represent experimental values. We can clearly see excellent agreement between the numerical and experimental values.

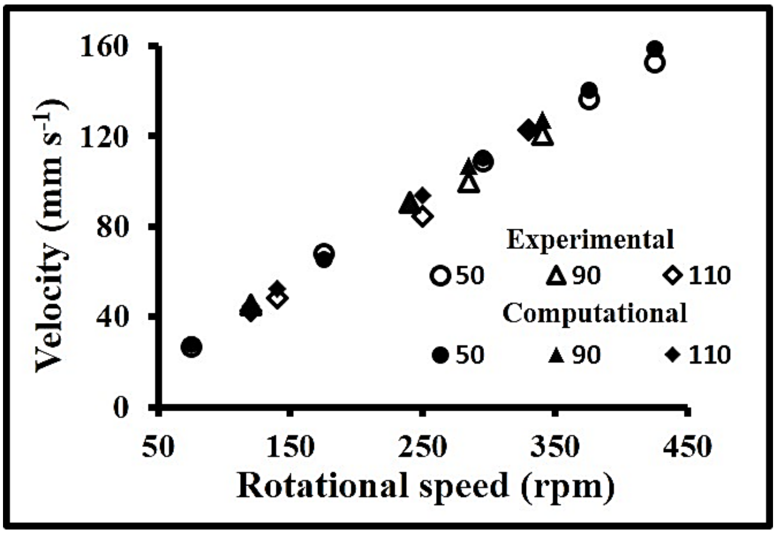

Fig. 7.6: Experimental and numerical velocities comparison at 50-110 mm min^{-1} and 75-425 rpm.

7.3.3 Strain rate

Figs. 7.7 a-c show the variation of strain rate value with radial distance at 300 rpm 50 mm min^{-1}, 340 rpm 90 mm min^{-1} and 330 rpm 110 mm min^{-1}, respectively. Both experimental and

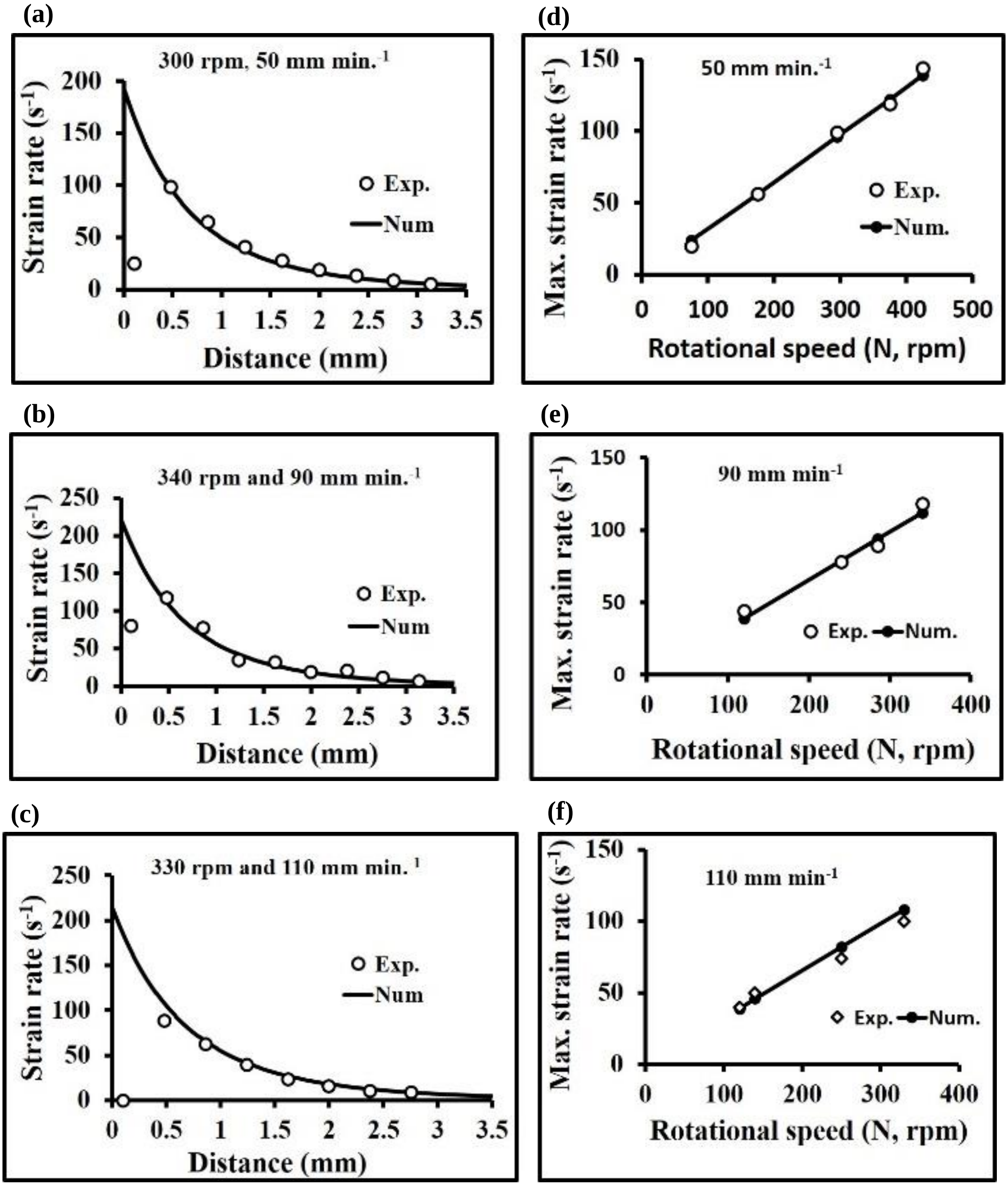

Fig. 7.7: Strain rate variation with, a) radial distance at 300 rpm and 50 mm min^{-1}, b) radial distance at 340 rpm and 90 mm min^{-1}, c) radial distance at 330 rpm and 110 mm min^{-1}, d) rotational speed at 50 mm min^{-1}, e) rotational speed at 90 mm min^{-1}, and f) rotational speed at 110 mm min^{-1}.

numerical values have been plotted for the comparison purpose. An excellent agreement between the two values is observed for the ranges of parameters investigated, except near the pin surface value (0.1 mm from pin surface). Since the strain rate field is derived from the velocity field, differentiation schemes must be used to determine the derivatives. Such schemes, however, are susceptible to errors resulting from different grid spacing as well as noise within the velocity data, detailed is given in appendix B. Since the distance between two successive measuring points is 35×10^{-2} mm and $\sim1.7\times10^{-4}$ mm in experimental and numerical methods, respectively, it is clear that the strain rate obtained numerically is more accurate compared to that obtained from the experimental data of PIV, due to large number of points.

Figs. 7.7 d-f show the variation in strain rate at ~0.47 mm distance from pin surface (as discussed in experimental part) with rotational speeds, rpm, at a given traverse speed, i.e., 50, 90 and 110 mm min^{-1}, respectively. Both numerical as well as experimental values of the strain rate show excellent linear correspondence with increasing rotational speed (rpm).

Further, the experimental values of strain rate are compared with numerical values at 0.47 mm distance for different rotational and traverse speeds in Fig. 7.8. Over the ranges of parameters, both values overlap, thereby suggesting that the experimental results are very well predicted with the computational model.

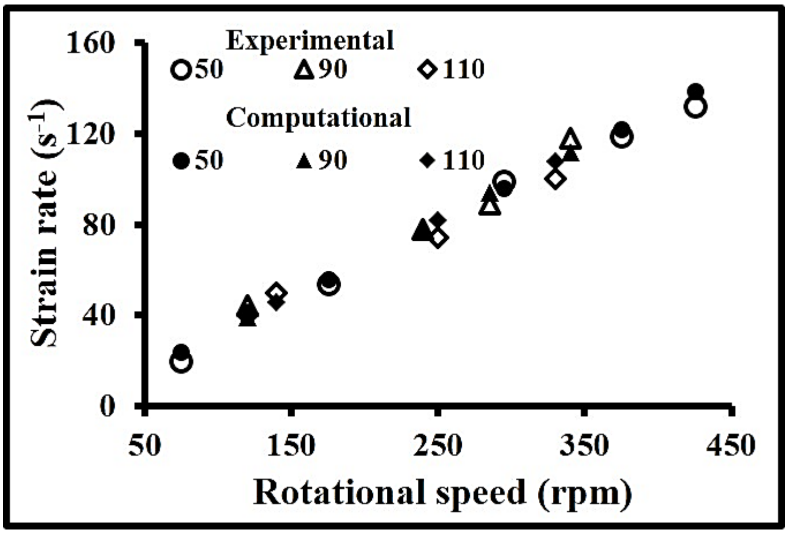

Fig. 7.8: Experimental and numerical strain rates comparison at 50-110 mm min^{-1} and 75-425 rpm.

7.4 Summary

The computational results for material flow around the tool pin have shown the similar behaviour to those obtained through the PIV experiments. In particular, the predicted as well as derived quantities have shown greater level of correspondence between experimental and numerical values. However, the numerical results can be said to be more accurate, due to the precision limitation of PIV setup. Overall, both experimental and numerical techniques have successfully predicted the material flow visualization around the tool with the best accuracy under the given conditions/approximations. Both procedures can reliably be used to understand such behaviour of FSW processes.

CHAPTER 8

SUMMARY AND CONCLUSIONS

This chapter concludes the results obtained in this thesis. Further, the scope of the future possibilities of exploration of this problem has been suggested.

8.1 Summary

From the observations elaborated in the Chapters 5, 6 and 7, following three material flow movements were observed.

i) Rotation of the material around tool pin.

ii) Downward push of the material

Rotation around the tool pin: modelling and simulation, as well as experimental works, showed that material rotates multiple times around tool pin [50, 69, 73, 74, 98]. However, Liu et al. [161] proposed that the material rotates around the pin only once. Material rotation around the tool pin is primarily due to the drag force F_d exerted by the rotating shoulder and the pin. In absence of a traverse motion, the material should keep rotating with the rotating tool. However, combining traverse with the rotation motion of the tool is expected to force the material to enter and exit the rotational zone [110]. The material enters in the rotational zone from leading-advancing side and experiences thorough mixing in the nugget zone. However by TIT, it is not clear whether the material rotates more than once before it exit from trailing-advancing side. Chapter 6 (PIV technique) and chapter 7 (Numerical simulation) were represented that the material rotate multiple times around the tool pin. The width of the rotational zone was observed to be approximately 1.2 mm at 300 rpm around the pin by PIV technique. Furthermore, the size of the rotational zone depends on the tool rotational/traverse speeds and measurement location, i.e., higher rotational speed yields a larger rotational zone. However, the rise in the size of the rotational zone cannot be monotonic and will depend on the change in flow conditions from sticking mode to slipping mode at higher rpm. The rotational zone is wider near the top surface due to the effect of the rotating shoulder and its effect decreases with an increase in depth. Further, the translation of tool in leading direction forms a shearing layer around the rotating zone, which detached from the rotational zone in trailing side during each revolution. Such attachment and detachment of shear layer develops the extrusion/transitional zone. Extrusion zone appeared to be non-circular region (chapter 6). The ratio of radial thickness in RS and AS in the transitional zone, say z_t, is observed to be approximately 1.5. This shape asymmetry is closely consistent with the experimental work of Guerra et al. [82] and Schmidt et al. [83].

Downward push of the material: one of the most important material flow characteristic during the FSW process is vertical flow, which is responsible for filling the cavity at the back of the tool pin. The material after exit from the rotational zone experiences the normal load due to tilted shoulder flows downward in the cavity left behind by the traversing pin. The flow occurs under the constraint imposed by the rotating shoulder, pin, and relatively hard surroundings. The extent of vertical movement will be decided by the rotation speed, weld-pitch, and tilt angle. It will be interesting, however, to study material flow in the recently developed stationary shoulder friction stir welding [151, 152]. Since there is no contribution of a rotating shoulder on heat generation and drag force, the vertical flow is expected to modify.

8.2 Conclusions

The important conclusions from the various techniques were used to understand material flow behaviour during friction stir welding or processing, are summarized.

Tracer insert techniques: tracer insert technique was used to study three dimensional material flow behaviour and strain achieved during the FSW process by using tracer and workpiece of 5083 aluminium alloy. The material flow was explained by resolving forces acting due to titled shoulder and material confinement due to cold surroundings.

1) The material rotate around the tool pin was primarily due to the drag force exerted by the rotating shoulder and the pin. The rotational zone was wider near the top surface due to the effect of the rotating shoulder and effect decreases with an increase in depth. The material enters in the rotational zone from L-A side and experiences thorough mixing in the nugget zone. However, it is not clear whether the material rotated more than once before its exit from T-A side.
2) The material exited from the rotational zone, moved toward AS and flowed downward in the cavity left behind by the traversing pin, due to drag and forging forces exerted by the rotating shoulder. The flow occurred under the constraint imposed by the rotating shoulder, pin, and relatively hard surroundings. The constraint imposed by different bodies exerted a torque on the soft material and forced it to flow downwards in AS and upwards in RS. The surrounding hard material acted as a pivot to the vertical rotation.
3) The tracer close to shoulder flowed in a similar fashion as observed by others. However, the tracers below the shoulder showed that the flow was truncated at the PCL. The

truncated flow was either due to exit of material from rotational zone or vertical flow of the material in the AS.

4) The tracer placed at process centerline (PCL) showed inverted S shape material flow. The maximum displacement was ~2 mm on the retreating side and ~1.5 mm in the advancing side. It was thoroughly mixed in the nugget zone. In the AS, material experienced the highest degree of mixing (very high strain). RS material remained in RS and did not experience the mixing of the same order. In the RS, the material flowed from the tip of the pin toward the shoulder. However, it encountered a counterflow from the shoulder which resulted in material accumulation at a distance of 1.5 mm from the top.

5) The maximum tensile strain of 2 was measured close to the top surface (near shoulder) and maximum compressive strain of 0.4 was measured at 1.5 mm depth from the top surface in the retreating side. From process centerline to advancing side strain could not be measured due to vigorous mixing. Near the top surface the material was stretched and at the mid-length of the pin, the material was compressed.

Particle image velocimetry technique: the material flow and strain rate during the FSW process was successfully visualized by PIV technique. The importance of the work lies in the fact that an instantaneous evaluation of the material flow during the FSW can be performed. The proposed method offers great potential in the development of different tool geometries and processing parameters by effective visualization of the material flow patterns. Specific outcomes of the work are as follows.

1) Two-dimensional flow patterns around the pin at mid-length were obtained using glass tracers in a transparent non-Newtonian material.
2) The rotational zone of approximately 1.2±0.1 mm width was observed around the pin. The material in the rotational zone entered between AS and LS of the pin. The material than rotated around the tool pin several times before its exit between TS and AS.
3) In the transitional zone, the streamlines were uniform at LS (front of the tool pin) whereas, these were dense and sparse between TS and AS (back of the tool pin). This indicates that the material flow velocity more where dense and less where sparse. There was an accumulation of the material at the back of AS due to the low-pressure zone created at the back of the pin.

4) The maximum velocity is found 85% of the pin peripheral velocity close to the pin surface and decrease from its maximum near the tool pin to stagnant material. The velocity at RS was found to be higher than that at AS.

5) The maximum strain rate at 300 rpm and 50 mm min^{-1} traverse speed was 100 s^{-1} at 0.47 mm distance from pin surface. The maximum strain rate around the pin periphery found to increase linearly with rotational speed, irrespective of the traverse speed. Predictive relations were developed to quantify strain rate variation as a function of rotation speed and weld-pitch.

Numerical simulation: the experimental results of PIV studies were compared with numerical simulation results of the experimental material. Specific outcomes of the work are as follows.

1) The maximum material flow velocity at the pin surface was found to be equal to the pin peripheral velocity. The velocity decreased with radial distance from pin surface. Maximum velocity was found to increase linearly with increase in the rotational speed. The model predicted no slip condition between the material and tool pin interface.
2) The maximum strain-rate was observed at pin surface. The strain rate was found to decrease with radial distance. Maximum strain rate was found to increase from 48 s^{-1} to 275 s^{-1} with increase in rotation speed from 75 rpm to 425 rpm.
3) The computational results for material flow around the tool pin have shown the similar behavior to those obtained through the PIV experiments. Both experimental and numerical techniques have successfully predicted the material flow visualization around the tool with the best accuracy under the given conditions/approximations. Both procedures can reliably be used to understand such behavior in FSW process.

8.3 Future scope

- The changes in flow behavior and strain during FSW with different tool geometries and processing parameters in metallic material by using same tracer and workpiece material.
- In-situ flow visualization of FSW/FSP process with different tool geometries.
- In-situ flow visualization using PIV technique for the tool with shoulder, to bring out effect of shoulder on material flow behavior.

PUBLICATIONS

1. **Rahul kumar**, V. Pancholi, R. P. Bharti, “Material flow visualization and determination of strain rate during friction stir welding”, Journal of Material Processing Technology, vol. 255, pp. 470–476, 2018.

2. **Rahul Kumar**, V. Pancholi, “Three-dimensional material flow during FSW of AA5083 – analysis-using tracer of the same material” (to be communicated).

3. **Rahul kumar**, Abhishek kumar Lal, R. P. Bharti, V. Pancholi, “Experimental and numerical investigation of material flow characteristics around the tool pin in FSW process” (to be communicated).

REFERENCES.

[1] C. J. D. M. W. Thomas, J. Nicholas, J. C. Needham, M. G. Murch, P. Templesmith, “Friction stir butt welding,” *G.B. Pat. Appl. No. 9125978.8,* 1991.

[2] P. L. Threadgill, A. J. Leonard, H. R. Shercliff, and P. J. Withers, “Friction stir welding of aluminium alloys,” *Int. Mater. Rev.*, vol. 54, pp. 49–93, 2009.

[3] J. A. Esparza, W. C. Davis, E. A. Trillo, and L. E. Murr, “Friction-stir welding of magnesium alloy AZ31B,” *J. Mater. Sci. Lett.*, vol. 21, pp. 917–920, 2002.

[4] W. Yuan, S. K. Panigrahi, and R. S. Mishra, “Achieving high strength and high ductility in friction stir-processed cast magnesium alloy,” *Metall. Mater. Trans. A*, vol. 44A, pp. 3675–3684, 2013.

[5] R. S. Mishra and Z. Y. Ma, “Friction stir welding and processing,” *Mater. Sci. Eng. R Reports*, vol. 50, pp. 1–78, 2005.

[6] R. S. Mishra and M. W. Mahoney, “Friction Stir Welding and Processing,” in *ASM International*, pp. 1–5, 2007

[7] Y. Huang, Y. Wang, L. Wan, H. Liu, and J. Shen, “Material-flow behavior during friction-stir welding of 6082-T6 aluminum alloy,” *Int. J. Adv. Manuf. Technol.*, vol. 87, pp. 1115–1123, 2016.

[8] M. F Khan, G. Racineux, S. Marya, and S. K. Panigrahi, “Influence of Friction Stir Processing on Material Flow Behavior and Microstructural Modification of a Al-Si cast alloy,” *Int. Conf. Frict. based Process.*, pp. 1–6, 2014.

[9] L. Cui, X. Yang, G. Zhou, X. Xu, and Z. Shen, “Characteristics of defects and tensile behaviors on friction stir welded AA6061-T4,” *Mater. Sci. Eng. A,* vol. 543, pp. 58–68, 2012.

[10] H. Zhang, S. B. Lin, L. Wu, J. C. Feng, and S. L. Ma, “Defects formation procedure and mathematic model for defect free friction stir welding of magnesium alloy,” *Mater. Des.*, vol. 27, pp. 805–809, 2006.

[11] A. S. Adadande, A. M. Naniwadekar, and S. P. Gaikwad, “An overview of Friction stir welded alloys : Microstructure and properties,” *IOSR J. Mech. Civ. Eng. ISSN 2278-1684,* pp. 1–6.

[12] R. Padmanaban, V. Ratna Kishore, and V. Balusamy, “Numerical simulation of temperature distribution and material flow during friction stir welding of dissimilar aluminum alloys,” *Procedia Eng.*, vol. 97, pp. 854–863, 2014.

[13] R. S. Mishra, M. W. Mahoney, and R. Grimes, “High strain rate superplasticity in

friction stir processed Al Á Mg Á Zr alloy," *Mater. Sci. Eng. A*, vol. 351, pp. 148–153, 2003.

[14] M. W. Mahoney, C. G. Rhodes, J. G. Flintoff, R. A. Spurling, and W. H. Bingel, "Properties of Friction-Stir-Welded 7075 T651 Aluminum," *Metall. Mater. Trans. A*, vol. 29A, pp. 1955–1964, 1998.

[15] Y. M. Hwang, Z. W. Kang, Y. C. Chiou, and H. H. Hsu, "Experimental study on temperature distributions within the workpiece during friction stir welding of aluminum alloys," *Int. J. Mach. Tools Manuf.*, vol. 48, pp. 778–787, 2008.

[16] W. Tang, X. Guo, J. C. McClure, L. E. Murr, and A. Nunes, "Heat input and temperature distribution in friction stir welding," *J. Mater. Process. Manuf. Sci.*, vol. 7, pp. 163–172, 1998.

[17] M. Mijajlovic´, D. Milcˇic´, and M. Milcˇic´, "Numerical simulation of friction stir welding," *Therm. Sci.*, vol. 18, pp. 967–978, 2014.

[18] C. G. Rhodes, M. W. Mahoney, W. H. Bingel, R. a. Spurling, and C. C. Bampton, "Effects of friction stir welding on microstructure of 7075 aluminum," *Scr. Mater.*, vol. 36, pp. 69–75, 1997.

[19] L. E. Murr, G. Liu, and J. C. Mcclure, "A TEM study of precipitation and related microstructures in friction-stir-welded 6061 aluminium," *J. Mater. Sci.*, vol. 33, pp. 1243–1251, 1998.

[20] Y. S. Sato, H. Kokawa, M. Enomoto, and S. Jogan, "Microstructural evolution of 6063 aluminum during friction-stir welding," *Metall. Mater. Trans. A*, vol. 30, pp. 2429–2437, 1999.

[21] P. Heurtier, M. J. Jones, C. Desrayaud, J. H. Driver, F. Montheillet, and D. Allehaux, "Mechanical and thermal modelling of Friction Stir Welding," *J. Mater. Process. Technol.*, vol. 171, pp. 348–357, 2006.

[22] W. J. A. and P. J. Hartley, "Friction stir weld technology development at Lockheed Martin Michoud space system-an overview," in *Proceedings in Fifth internation conferrences on trends in welding research*, 1998, pp. 541–546.

[23] H. Fujii, Y. G. Kim, T. Tsumura, T. Komazaki, and K. Nakata, "Estimation of Material Flow in Stir Zone during Friction Stir Welding by Distribution Measurement of Si Particles," *Mater. Trans.*, vol. 47, pp. 224–232, 2006.

[24] P. Biswas, D. A. Kumar, and N. R. Mandal, "Friction stir welding of aluminum alloy with varying tool geometry and process parameters," *Proc. Inst. Mech. Eng. , Part B J. Eng. Manuf.*, vol. 226, pp. 641–648, 2012.

[25] A. K. Kadian and P. Biswas, “A Comparative Study of Material Flow Behavior in Friction Stir Welding Using Laminar and Turbulent Models,” *J. Mater. Eng. Perform.*, vol. 24, pp. 4119–4127, 2015.

[26] A. Arora, A. De, and T. Debroy, “Toward optimum friction stir welding tool shoulder diameter,” *Scr. Mater.*, vol. 64, pp. 9–12, 2011.

[27] M. Mehta, A. Arora, A. De, and T. Debroy, “Tool geometry for friction stir welding - Optimum shoulder diameter,” *Metall. Mater. Trans. A*, vol. 42, pp. 2716–2722, 2011.

[28] M. Grujicic *et al.*, “Computational analysis of material flow during friction stir welding of AA5059 aluminum alloys,” *J. Mater. Eng. Perform.*, vol. 21, pp. 1824–1840, 2012.

[29] M. Azizieh, A. H. Kokabi, and P. Abachi, “Effect of rotational speed and probe profile on microstructure and hardness of AZ31 / Al 2 O 3 nanocomposites fabricated by friction stir processing,” *Mater. Des.*, vol. 32, pp. 2034–2041, 2011.

[30] G. Buffa, J. Hua, R. Shivpuri, and L. Fratini, “Design of the friction stir welding tool using the continuum based FEM model,” *Mater. Sci. Eng. A*, vol. 419, pp. 381–388, 2006.

[31] H. Su, C. S. Wu, M. Bachmann, and M. Rethmeier, “Numerical modeling for the effect of pin profiles on thermal and material flow characteristics in friction stir welding,” *Mater. Des.*, vol. 77, pp. 114–125, 2015.

[32] H. K. Mohanty, M. M. Mahapatra, P. Kumar, P. Biswas, and N. R. Mandal, “Effect of tool shoulder and pin probe profiles on friction stirred aluminum welds - a comparative study,” *J. Mar. Sci. Appl.*, vol. 11, pp. 200–207, 2012.

[33] N. R. Mandal, M. M. Mahapatra, and S. P. Harsh, “Tool Design Effects for FSW of AA7039,” *Weld. J.*, vol. 92, pp. 41–47, 2013.

[34] S. R. Prasad, A. Kumar, C. Sridhar, and L. S. Raju, “Influence of tool shoulder geometry on microstructure and mechanical properties of friction stir welded 2014-T6 Aluminium Alloy,” *Mater. Today Proc.*, vol. 4, pp. 10207–10211, 2017.

[35] H. Schmidt, J. Hattel, and J. Wert, “An analytical model for the heat generation in friction stir welding,” *Model. Simul. Mater. Sci. Eng.*, vol. 12, pp. 143–157, 2004.

[36] K. Ullegaddi, V. Murthy, and R. N. Harsha, “Friction Stir Welding Tool Design and Their Effect on Welding of AA6082-T6,” *Mater. Today Proc.*, vol. 4, pp. 7962–7970, 2017.

[37] I. Galvão, R. M. Leal, D. M. Rodrigues, and A. Loureiro, “Influence of tool shoulder geometry on properties of friction stir welds in thin copper sheets,” *J. Mater. Process. Technol.*, vol. 213, pp. 129–135, 2013.

[38] L. Cederqvist, C. D. Sorensen, A. P. Reynolds, and T. Öberg, “Improved process stability during friction stir welding of 5 cm thick copper canisters through shoulder geometry and parameter studies,” *Sceince Technol. Weld. Join.*, vol. 14, pp. 178–184, 2009.

[39] A. Scialpi, L. A. C. De Filippis, and P. Cavaliere, “Influence of shoulder geometry on microstructure and mechanical properties of friction stir welded 6082 aluminium alloy,” *Mater. Des.*, vol. 28, pp. 1124–1129, 2007.

[40] R. M. Leal, C. Leitão, A. Loureiro, D. M. Rodrigues, and P. Vilac, “Material flow in heterogeneous friction stir welding of thin aluminium sheets : Effect of shoulder geometry,” *Mater. Sci. Eng. A*, vol. 498, pp. 384–391, 2008.

[41] K. Elangovan and V. Balasubramanian, “Influences of tool pin profile and tool shoulder diameter on the formation of friction stir processing zone in AA6061 aluminium alloy,” *Mater. Des.*, vol. 29, pp. 362–373, 2008.

[42] K. Elangovan, V. Balasubramanian, and M. Valliappan, “Effect of Tool Pin Profile and Tool Rotational Speed on Mechanical Properties of Friction Stir Welded AA6061 Aluminium Alloy Effect of Tool Pin Profile and Tool Rotational Speed on Mechanical Properties of Friction Stir Welded AA6061 Aluminium Alloy,” *Mater. Manuf. Process.*, vol. 23, pp. 251–260, 2008.

[43] H. Khodaverdizadeh, A. Heidarzadeh, and T. Saeid, “Effect of tool pin profile on microstructure and mechanical properties of friction stir welded pure copper joints,” *Mater. Des.*, vol. 45, pp. 265–270, 2013.

[44] M. Imam, K. Biswas, and V. Racherla, “Effect of weld morphology on mechanical response and failure of friction stir welds in a naturally aged aluminium alloy,” *Mater. Des.*, vol. 44, pp. 23–34, 2013.

[45] D. A. Mehta M and T. Debroy, “Material adhesion and stresses on friction stir welding tool pins Material adhesion and stresses on friction stir welding tool pins,” *Sceince Technol. Weld. Join.*, vol. 19, pp. 534–540, 2014.

[46] M. Mehta, G. M. Reddy, A. V Rao, and A. De, “Numerical modeling of friction stir welding using the tools with polygonal pins,” *Def. Technol.*, vol. 11, pp. 229–236, 2015.

[47] C. Venkata, G. M. Reddy, and K. S. Rao, “Microstructure and pitting corrosion resistance of AA2219 Al e Cu alloy friction stir welds e Effect of tool profile,” *Def. Technol.*, vol. 11, pp. 123–131, 2015.

[48] A. Amirafshar and H. Pouraliakbar, “Effect of tool pin design on the microstructural evolutions and tribological characteristics of friction stir processed structural steel,”

Measurement, vol. 68, pp. 111–116, 2015.

[49] K. K. Mugada and K. Adepu, “Influence of ridges shoulder with polygonal pins on material flow and friction stir weld characteristics of 6082 aluminum alloy,” *J. Manuf. Process.*, vol. 32, pp. 625–634, 2018.

[50] Y. Morisada, T. Imaizumi, and H. Fujii, “Clarification of material flow and defect formation during friction stir welding,” *Sci. Technol. Weld. Join.*, vol. 20, pp. 130–137, 2015.

[51] C. I. Chang, C. J. Lee, and J. C. Huang, “Relationship between grain size and Zener-Holloman parameter during friction stir processing in AZ31 Mg alloys,” *Scr. Mater.*, vol. 51, pp. 509–514, 2004.

[52] G. Buffa, J. Hua, R. Shivpuri, and L. Fratini, “A continuum based fem model for friction stir welding — model development,” *Mater. Sci. Eng. A*, vol. 419, pp. 389–396, 2006.

[53] A. H. Ammouri, G. Kridli, G. Ayoub, and R. F. Hamade, “Relating grain size to the Zener-Hollomon parameter for twin-roll-cast AZ31B alloy refined by friction stir processing,” *J. Mater. Process. Technol.*, vol. 222, pp. 301–306, 2015.

[54] W. Liu, H. Zhao, D. Li, Z. Zhang, G. Huang, and Q. Liu, “Hot deformaation behavior of AA7085 aluminum alloy during compression at elevated temperatures,” *Mater. Sci. Eng. A*, vol. 596, pp. 176–182, 2014.

[55] A. Kumar, M. M. Mahapatra, P. K. Jha, N. R. Mandal, and V. Devuri, “Influence of tool geometries and process variables on friction stir butt welding of Al-4.5%Cu/TiC in situ metal matrix composites,” *Mater. Des.*, vol. 59, pp. 406–414, 2014.

[56] D. A. Rai, R, H. K. D. H. Bhadeshia, and T. Debroy, “Review : friction stir welding tools Review : friction stir welding tools,” *Sceince Technol. Weld. Join.*, vol. 16, pp. 325–342, 2011.

[57] A. Gerlich, G. Avramovic-Cingara, and T. H. North, “Stir zone microstructure and strain rate during Al 7075-T6 friction stir spot welding,” *Metall. Mater. Trans. A*, vol. 37, pp. 2773–2786, 2006.

[58] L. Long, G. Chen, S. Zhang, T. Liu, and Q. Shi, “Finite-element analysis of the tool tilt angle effect on the formation of friction stir welds,” *J. Manuf. Process.*, vol. 30, pp. 562–569, 2017.

[59] T. Sheppard and D. S. Wright, “Determination of flow stress: part1 constitutive equation for aluminum alloys at elevated temperatures,” *Met. Technol.*, pp. 215–223, 1979.

[60] K. Kumar and S. V. Kailas, “The role of friction stir welding tool on material flow and weld formation,” *Mater. Sci. Eng. A*, vol. 485, pp. 367–374, 2008.

[61] H. W. Zhang, Z. Zhang, and J. T. Chen, “3D modeling of material flow in friction stir welding under different process parameters,” *J. Mater. Process. Technol.*, vol. 183, pp. 62–70, 2007.

[62] K. V Jata and S. L. Semiatin, “Continuous dynamic recrystallization during friction stir welding of high strength aluminum alloys,” *Scripta. Mater*, vol. 43, pp. 743–749, 2000.

[63] K. Masaki, Y. S. Sato, M. Maeda, and H. Kokawa, “Experimental simulation of recrystallized microstructure in friction stir welded Al alloy using a plane-strain compression test,” *Scr. Mater.*, vol. 58, pp. 355–360, 2008.

[64] Z. W. Chen and S. Cui, “Strain and strain rate during friction stir welding/processing of Al-7Si-0.3Mg alloy,” *IOP Conf. Ser. Mater. Sci. Eng.*, vol. 4, pp. 012026, 2009.

[65] S. Mukherjee and A. K. Ghosh, “Flow visualization and estimation of strain and strain-rate during friction stir process,” *Mater. Sci. Eng. A*, vol. 527, pp. 5130–5135, 2010.

[66] A. Gerlich, M. Yamamoto, and T. H. North, “Strain rates and grain growth in Al 5754 and Al 6061 friction stir spot welds,” *Metall. Mater. Trans. A Phys. Metall. Mater. Sci.*, vol. 38, pp. 1291–1302, 2007.

[67] A. Mohan, S. K. Panigrahi, R. S. Mishra, and R. Verma, “Influence of strain and strain rate on microstructural evolution during superplasticity of Mg-Al-Zn sheet,” *J. Mater. Sci.*, vol. 48, pp. 5633–5644, 2013.

[68] B. C. Liechty and B. W. Webb, “Flow field characterization of friction stir processing using a particle-grid method,” *J. Mater. Process. Technol.*, vol. 208, pp. 431–443, 2008.

[69] Y. Morisada, T. Imaizumi, and H. Fujii, “Determination of strain rate in Friction Stir Welding by three-dimensional visualization of material flow using X-ray radiography,” *Scr. Mater.*, vol. 106, pp. 57–60, 2015.

[70] H. W. Zhang, Z. Zhang, and J. T. Chen, “3D modeling of material flow in friction stir welding under different process parameters,” *J. Mater. Process. Technol.*, vol. 183, pp. 62–70, 2007.

[71] Ø. Frigaard, Ø. Grong, and O. T. Midling, “A process model for friction stir welding of age hardening aluminum alloys,” *Metall. Mater. Trans. A*, vol. 32, pp. 1189–1200, 2001.

[72] R. Nandan, G. G. Roy, T. Debroy, and I. Introduction, “Numerical Simulation of Three-Dimensional Heat Transfer and Plastic Flow During Friction Stir Welding,” *Metall. Mater. Trans. A*, vol. 37, pp. 1247–1259, 2006.

[73] R. Nandan, G. G. Roy, T. J. Lienert, and T. DebRoy, “Numerical modelling of 3D plastic flow and heat transfer during friction stir welding of stainless steel,” *Sci. Technol. Weld. Join.*, vol. 11, pp. 526–537, 2006.

[74] R. Nandan, G. G. Roy, T. J. Lienert, and T. Debroy, “Three-dimensional heat and material flow during friction stir welding of mild steel,” *Acta Mater.*, vol. 55, pp. 883–895, 2007.

[75] V. Malik and S. V Kailas, “Plasticine Modeling of Material Mixing in Friction Stir Welding,” *J. Mater. Process. Tech.*, vol. 258, pp. 80–88, 2018.

[76] T. Long, W. Tang, and A. P. Reynolds, “Process response parameter relationships in aluminium alloy friction stir welds,” *Sci. Technol. Weld. Join.*, vol. 12, pp. 311–317, 2007.

[77] A. Arora, Z. Zhang, A. De, and T. DebRoy, “Strains and strain rates during friction stir welding,” *Scr. Mater.*, vol. 61, pp. 863–866, 2009.

[78] G. Chen *et al.*, “Computational fluid dynamics studies on heat generation during friction stir welding of aluminum alloy,” *Comput. Mater. Sci.*, vol. 79, pp. 540–546, 2013.

[79] G. Chen, Q. Ma, S. Zhang, J. Wu, G. Zhang, and Q. Shi, “Computational fluid dynamics simulation of friction stir welding: A comparative study on different frictional boundary conditions,” *J. Mater. Sci. Technol.*, vol. 34, pp. 128–134, 2017.

[80] A. Arora, R. Nandan, A. P. Reynolds, and T. Debroy, “Torque , power requirement and stir zone geometry in friction stir welding through modeling and experiments,” *Scr. Mater.*, vol. 60, pp. 13–16, 2009.

[81] K. J. Colligan, “Material Flow Behavior during Friction Stir Welding of Aluminum,” *Weld. Res. Suppl.*, vol. 78, pp. 229–237, 1999.

[82] M. Guerra, C. Schmidt, J. C. McClure, L. E. Murr, and A. C. Nunes, “Flow patterns during friction stir welding,” *Mater. Charact.*, vol. 49, pp. 95–101, 2003.

[83] H. N. B. Schmidt, T. L. Dickerson, and J. H. Hattel, “Material flow in butt friction stir welds in AA2024-T3,” *Acta Mater.*, vol. 54, pp. 1199–1209, 2006.

[84] W. Li, J. Li, Z. Zhang, D. Gao, and Y. Chao, “Metal Flow during Friction Stir Welding of 7075-T651 Aluminum Alloy,” *Exp. Mech.*, pp. 1573–1582, 2013.

[85] O. Lorrain, V. Favier, H. Zahrouni, and D. Lawrjaniec, “Understanding the material flow path of friction stir welding process using unthreaded tools,” *J. Mater. Process. Technol.*, vol. 210, pp. 603–609, 2010.

[86] A. A. M. da Silva, E. Arruti, G. Janeiro, E. Aldanondo, P. Alvarez, and A. Echeverria, “Material flow and mechanical behaviour of dissimilar AA2024-T3 and AA7075-T6 aluminium alloys friction stir welds,” *Mater. Des.*, vol. 32, pp. 2021–2027, 2011.

[87] T. U. Seidel and A. P. Reynolds, “Visualization of the material flow in AA2195 friction-stir welds using a marker insert technique,” *Metall. Mater. Trans. A*, vol. 32, pp. 2879–

2884, 2001.

[88] J. F. Guo, H. C. Chen, C. N. Sun, G. Bi, Z. Sun, and J. Wei, “Friction stir welding of dissimilar materials between AA6061 and AA7075 Al alloys effects of process parameters,” *Mater. Des.*, vol. 56, pp. 185-192, 2014.

[89] K. Kumar, S. V Kailas, K. Kumar, and S. V Kailas, “Positional dependence of material flow in friction stir welding : analysis of joint line remnant and its relevance to dissimilar metal welding Positional dependence of material flow in friction stir welding : analysis of joint line remnant and its relevan,” *Sci. Technol. Weld. Join.*, vol. 15, pp. 305–311, 2010.

[90] X. C. Liu, Y. F. Sun, Y. Morisada, and H. Fujii, “Dynamics of rotational flow in friction stir welding of aluminium alloys,” *J. Mater. Process. Technol.*, vol. 252, pp. 643–651, 2018.

[91] P. Alvarez, G. Janeiro, A. A. M. da Silva, E. Aldanondo, and A. Echeverría, “Material flow and mixing patterns during dissimilar FSW,” *Sci. Technol. Weld. Join.*, vol. 15, pp. 648–653, 2010.

[92] Y. G. Kim, H. Fujii, T. Tsumura, T. Komazaki, and K. Nakata, “Three defect types in friction stir welding of aluminum die casting alloy,” *Mater. Sci. Eng. A*, vol. 415, pp. 250–254, 2006.

[93] T. Long and A. P. Reynolds, “Parametric studies of friction stir welding by commercial fluid dynamics simulation,” *Sci. Technol. Weld. Join.*, vol. 11, pp. 200–208, 2006.

[94] R. Padmanaban, V. R. Kishore, and V. Balusamy, “Numerical Simulation of Temperature Distribution and Material Flow During Friction Stir Welding of Dissimilar Aluminum Alloys,” *Procedia Eng.*, vol. 97, pp. 854–863, 2014.

[95] M. Nourani, A. S. Milani, and S. Yannacopoulos, “On the Experimental and Numerical Predictions of Strain during Friction Stir Welding : A Case Study on 7050 Aluminum Alloy,” *Trans. Control Mech. Syst.*, vol. 1, pp. 259–263, 2012.

[96] P. Ulysse, “Three-dimensional modeling of the friction stir-welding process,” *Int. J. Mach. Tools Manuf.*, vol. 42, pp. 1549–1557, 2002.

[97] B. C. Liechty and B. W. Webb, “The use of plasticine as an analog to explore material flow in friction stir welding,” *J. Mater. Process. Technol.*, vol. 184, pp. 240-250, 2007.

[98] Y. Morisada, H. Fujii, Y. Kawahito, K. Nakata, and M. Tanaka, “Three-dimensional visualization of material flow during friction stir welding by two pairs of X-ray transmission systems,” *Scr. Mater.*, vol. 65, pp. 1085–1088, 2011.

[99] R. Nandan, T. DebRoy, and H. K. D. H. Bhadeshia, “Recent advances in friction-stir

welding - Process, weldment structure and properties," *Prog. Mater. Sci.*, vol. 53, pp. 980–1023, 2008.

[100] Y. T. and F. M. SHIMODA Yoichiro, TSUBAKI Masami, "Experimental and numerical studies of material flow during welding by friction stirring," *Qurat j Jpn weld Soc*, vol. 29, pp. 114–118, 2011.

[101] R. Kumar, V. Pancholi, and R. P. Bharti, "Material flow visualization and determination of strain rate during friction stir welding," *J. Mater. Process. Tech.*, vol. 255, pp. 470–476, 2018.

[102] G. A. Nowak, B. M., Hall, A. C., Knorovsky, "High-Speed Video Flow Visualization in Friction Stir Welds of Polycarbonate," *ASM International*, 2002.

[103] O. Aluko and M. B. Adeyemi, "Warm Compression Tests of Aluminum Alloy," *J. Mater. Eng. Perform.*, vol. 7, pp. 474–478, 1998.

[104] Z. Y. Chen, S. Q. Xu, and X. H. Dong, "Deformation behavior of aa6063 aluminium alloy after removing friction effect under hot working conditions," *Acta Metall. Sin.*, vol. 21, pp. 451–458, 2008.

[105] W. E. I. Xiu-yu, Z. Zi-qiao, F. U. Xin, and C. Qiu-ni, "Flow stress of 2197 Al-Li alloy during hot compression deformation," *Trans. Nonferrous Met. Soc. China*, vol. 17, pp. 280–284, 2007.

[106] H. Zhang, N. P. Jin, and J. H. Chen, "Hot deformation behavior of 7150 aluminum alloy during compression at elevated temperature," *Mater. Charact.*, vol. 60, pp. 530–536, 2009.

[107] Z. Q. Sheng and R. Shivpuri, "Modeling flow stress of magnesium alloys at elevated temperature," *Mater. Sci. Eng. A*, vol. 419, pp. 202–208, 2006.

[108] Handbook Committee, "Properties of wrought aluminum alloys," in *Properties and selection: Nonferrous allos and special-purpose materials*, Vol. 2., California: ASM International, 1990, pp. 177–187.

[109] C. Hamilton, S. Dymek, and M. Blicharski, "A model of material flow during friction stir welding," *Mater. Charact.*, vol. 59, pp. 1206–1214, 2008.

[110] P. A. Colegrove and H. R. Shercliff, "3-Dimensional CFD modelling of flow round a threaded friction stir welding tool profile," *J. Mater. Process. Tech.*, vol. 169, pp. 320–327, 2005.

[111] P. A. Colegrove and H. R. Shercliff, "Experimental and numerical analysis of aluminium alloy 7075-T7351 friction stir welds," *Sci. Technol. Weld. Join.*, vol. 8, pp. 360–368, 2003.

[112] H. Su, C. S. Wu, A. Pittner, and M. Rethmeier, “Thermal energy generation and distribution in friction stir welding of aluminum alloys,” *Energy,* vol. 77, pp. 720–731, 2014.

[113] S. D. Ji, Q. Y. Shi, L. G. Zhang, A. L. Zou, S. S. Gao, and L. V. Zan, “Numerical simulation of material flow behavior of friction stir welding influenced by rotational tool geometry,” *Comput. Mater. Sci.,* vol. 63, pp. 218–226, 2012.

[114] Z. Yu, W. Zhang, H. Choo, and Z. Feng, “Transient heat and material flow modeling of friction stir processing of magnesium alloy using threaded tool,” *Metall. Mater. Trans. A Phys. Metall. Mater. Sci.,* vol. 43, pp. 724–737, 2012.

[115] J. W. Qian, J. L. Li, J. T. Xiong, F. S. Zhang, W. Y. Li, and X. Lin, “Periodic variation of torque and its relations to interfacial sticking and slipping during friction stir welding,” *Sci. Technol. Weld. Join.*, vol. 17, pp. 338–341, 2012.

[116] H. Atharifar, D. Lin, and R. Kovacevic, “Numerical and experimental investigations on the loads carried by the tool during friction stir welding,” *J. Mater. Eng. Perform.*, vol. 18, pp. 339–350, 2009.

[117] H. Wang, P. A. Colegrove, and J. F. Dos Santos, “Numerical investigation of the tool contact condition during friction stir welding of aerospace aluminium alloy,” *Comput. Mater. Sci.*, vol. 71, pp. 101–108, 2013.

[118] D. Kim *et al.*, “Numerical simulation of friction stir butt welding process for AA5083-H18 sheets,” *Eur. J. Mech. A/Solids*, vol. 29, pp. 204–215, 2010.

[119] B. C. Liechty and B. W. Webb, “Modeling the frictional boundary condition in friction stir welding,” *Int. J. Mach. Tools Manuf.*, vol. 48, pp. 1474–1485, 2008.

[120] Y. Zhu, G. Chen, Q. Chen, G. Zhang, and Q. Shi, “Simulation of material plastic flow driven by non-uniform friction force during friction stir welding and related defect prediction,” *Mater. Des.*, vol. 108, pp. 400–410, 2016.

[121] G. Chen, Z. Feng, Y. Zhu, and Q. Shi, “An Alternative Frictional Boundary Condition for Computational Fluid Dynamics Simulation of Friction Stir Welding,” *J. Mater. Eng. Perform.*, vol. 25, pp. 4016–4023, 2016.

[122] B. C. Liechty and B. W. Webb, “Modeling the frictional boundary condition in friction stir welding,” *Int. J. Mach. Tools Manuf.*, vol. 48, pp. 1474–1485, 2008.

[123] A. P. Reynolds, “Flow visualization and simulation in FSW,” *Scr. Mater.*, vol. 58, pp. 338–342, 2008.

[124] Y. Zhang, M. Yang, D. Ni, N. Zhang, and B. Gao, “Particle image velocimetry measurement of complex fl ow structures in the diffuser and spherical casing of a reactor

coolant pump," *Nucl. Eng. Technol.*, pp. 1–11, 2018.

[125] K. P. K. Panigrahi, "PIV investigation of flow behind surface mounted permeable ribs," *Exp. Fluids*, vol. 40, pp. 277–300, 2006.

[126] F. Coletti, I. Cresci, and T. Arts, "Spatio-temporal analysis of the turbulent flow in a ribbed channel," *Int. J. heat fluid flow,* vol. xxx, pp. xxx–xxx, 2013.

[127] R. Maiti, G. Das, and P. Kumar, "Experiments on eccentric granular discharge from a quasi-two-dimensional silo," *Powder Technol.*, vol. 301, pp. 1054–1066, 2016.

[128] P. R. Kukutla and B. V. S. S. Prasad, "Secondary flow visualization on stagnation row of a combined impingement and film cooled high- pressure gas turbine nozzle guide vane using PIV technique," *J. Vis.*, vol. 20, pp. 817–832, 2017.

[129] A. K. Prasad, "Particle Image Velocimetry Measurements in a Model Proton Exchange Membrane Fuel Cell," vol. 4, pp. 328–335, 2007.

[130] J. Meadows and A. K. Agrawal, "Time-resolved PIV of lean premixed combustion without and with porous inert media for acoustic control," *Combust. Flame*, vol. 162, pp. 1063–1077, 2015.

[131] L. Jiang and A. K. Agrawal, "Spray features in the near field of a flow blurring injector investigated by high -speed visualization and time- resolved PIV," *Exp. Fluids*, vol. 56, pp. 1–13, 2015.

[132] I. Ashraf and A. Agrawal, "Thrust generation and wake structure for flow across a pitching airfoil at low Reynolds number," vol. 40, pp. 2367–2379, 2015.

[133] R. J. Adrian, "Twenty years of particle image velocimetry," *Exp. Fluids*, vol. 39, pp. 159–169, 2005.

[134] A. A. Rashaida, "Flow of a Non-Newtonian Bingham Plastic Fluid Over a Rotating Disk," 2005.

[135] X. Cao, J. Liu, and N. Jiang, "Particle image velocimetry measurement of Indore airflow field: A review of technology and applications," *Energy Build.*, vol. 69, pp. 367–380, 2014.

[136] A. Cotroni, F. Di Felice, G. P. Romano, and M. Elefante, "Investigation of the near wake of a propeller using particle image velocimetry," *Exp. Fluids*, pp. 227–236, 2000.

[137] M. Schnick, M. Dreher, J. Zschetzsche, and U. Fuessel, " Visualization and optimization of shielding gas flows in arc welding," Welding in the world, vol. 56, pp. 54-61, 2012.

[138] L. Wang, M. Salewski, and B. Sundén, "Turbulent flow in a ribbed channel: Flow structures in the vicinity of a rib," *Exp. Therm. Fluid Sci.*, vol. 34, no. 2, pp. 165–176, 2010.

[139] N. Sharma, A. Tariq, and M. Mishra, “Experimental Investigation of Flow Structure due to Truncated Prismatic Rib Turbulators using Particle Image Velocimetry,” *Exp. Therm. Fluid Sci.*, vol. 91, pp. 479-508, 2018.

[140] N. Sharma, A. Tariq, and M. Mishra, “Detailed heat transfer and fluid flow investigation in a rectangular duct with truncated prismatic ribs,” *Exp. Therm. Fluid Sci.*, vol. 96, pp. 383–396, 2018.

[141] A. K. Prasad, “Flow and Particle Dispersion in a Pulmonary Alveolus — Part I : Velocity Measurements and Convective Particle Transport,” *J. Biomech. Eng.*, vol. 132, pp. 051009, 1–12, 2010.

[142] I. Grant, “Particle image velocimetry: a review,” *J. Mech. Eng. Sci.*, vol. 211 (1), pp. 55–76, 1997.

[143] D. P. Hart, “PIV error correction,” *Exp. Fluids*, vol. 29, pp. 13–22, 2000.

[144] R. J. Adrian, K. T. Christensen, and Z. Liu, “Analysis and interpretation of instantaneous turbulent velocity fields,” *Exp. Fluids*, vol. 29, pp. 275–290, 2000.

[145] M. Raffel, C. E. Willert, and J. Kompenhans, *Particle Image Velocimetry: A practical guide*, 1998.

[146] X. Cao, J. Liu, and N. Jiang, “An overview of the applications of particle image velocimetry for indoor airflow field measurement,” *Energy Build.*, vol. 69, pp. 367–380, 2014.

[147] J. D. Bugg and K. S. Rezkallah, “An analysis of noise in PIV images,” *J. Vis.*, vol. 1, pp. 217–226, 1998.

[148] R. Chhabra and J. F. Richardson, “Non-Newtonian fluid Behaviour,” in *Non-Newtonian Flow and Applied Rheology*, Second., Amsterdam: Elsevier, pp. 1–54, 2008.

[149] B. Wieneke, “PIV Uncertainty Quantification and Beyond,” 2017.

[150] R. D. Keane and R. J. Adrian, “Optimization of particle image veIocimeters. Part I : Double pulsed systems,” *Meas. Sci. Technol.*, vol. 1, pp. 1202–1215, 1990.

[151] S. D. Ji, X. C. Meng, J. G. Liu, L. G. Zhang, and S. S. Gao, “Formation and mechanical properties of stationary shoulder friction stir welded 6005A-T6 aluminum alloy,” *Mater. Des.*, vol. 62, pp. 113–117, 2014.

[152] D. Li, X. Yang, L. Cui, F. He, and X. Zhang, “Investigation of stationary shoulder friction stir welding of aluminum alloy 7075-T651,” *J. Mater. Process. Tech.*, vol. 222, pp. 391–398, 2015.

[153] H. W. Zhang, Z. Zhang, J. Bie, L. Zhou, and J. T. Chen, “Effect of viscosity on material behavior in friction stir welding process,” *Trans. Nonferrous Met. Soc. China*, vol. 16,

pp. 1045–1052, 2006.

[154] D. J. Forliti, P. J. Strykowski, and K. Debatin, “Bias and precision errors of digital particle image velocimetry,” *Exp. Fluids*, vol. 28, pp. 436–447, 2000.

[155] L. Casarsa and T. Arts, “Experimental Investigation of the Aerothermal Performance of a High Blockage Rib-Roughened Cooling Channel,” *J. Turbomach.*, vol. 127, pp. 580, 2005.

[156] A. Md Shaukat Ali, Tariq and B. K. Gandhi, “Role of Chamfering Angles and Flow Through Slit on Heat Transfer Augmentation Behind a Surface-Mounted Rib,” *J. Heat Transfer*, vol. 138, pp. 111901–1–16, 2016.

[157] Dushina, O. A., Molochnikov, V. M., Paereliy, A. A., Mikheev, N. I., & Lemanov, V., “Structure of the channel flow behind a surface-mounted rib under conditions of laminar-turbulent transition”, *Thermophysics and Aeromechanics, vol. 17*(3), pp. 323–335, 2010.

[158] R. P. Bharti and R. P. Chhabra, “Two-Dimensional Steady Poiseuille Flow of Power-Law Fluids Across a Circular Cylinder in a Plane Confined Channel : Wall Effects and Drag Coefficients,” *Ind. Eng. Chem. Res.*, vol. 46, pp. 3820–3840, 2007.

[159] Rahul C. Patil, Ram P. Bharti, Raj P. Chhabra," Study flow of power law fluids over a pairs of cylinder in tendam arrangement", *Ind. Eng. Chem. Res.*, vol. 47, pp. 1660–1683, 2008.

[160] R. Byron Bird, Robert C. Armstrong, Hassager Ole, “The Generalized Newtonian Fluid,” in *Dynamics of Polymer Liquids*, Second., JOWN WILEY & SONS, 1987, pp. 190–275.

[161] F.C. Liu, T.W. Nelson, In-situ material flow pattern around probe during friction stir welding of austenitic stainless steel, Mater. Des. 110 (2016) 354–364.

Appendix A

TWO-DIMENSIONAL PARTICLE IMAGE VELOCIMETRY (2D PIV)

Particle Image Velocimetry (PIV) measure instantaneous flow fields by recording images of suspended seed particles in flows at successive instants in time. In PIV, fluid velocity information at an “interrogation region” is obtained from many tracer particles, and it is obtained as the most probable statistical value. A typical interrogation region may contain images of 10-20 particles.

A.1 Working of PIV

Fig. A1 briefly illustrates a typical experimental arrangement for PIV image acquisition. For PIV measurements, tracer particles have to be added to the flow, which are further illuminated in a planar region within the flow-field by employing specialized lasers with spherical and cylindrical lenses, at least twice within a very short time interval. The time delay between two collinear laser pulses is referred to as pulse separation time, and is adjustable according to the mean flow velocity and the magnification at imaging. The pulse separation time between the laser pulses should be long enough to determine the displacement of particle images with sufficient resolution. However, it should be short enough to avoid particles with an out-of-plane velocity component leaving the light sheet between subsequent illuminations, as shown in Fig. A3 (b). The positions of the illuminated seeded particles are recorded on a single/sequence of frames using high-resolution CCD cameras. These frames are referred to as Frame 1 and Frame 2 corresponding to the particle positions at times and, respectively.

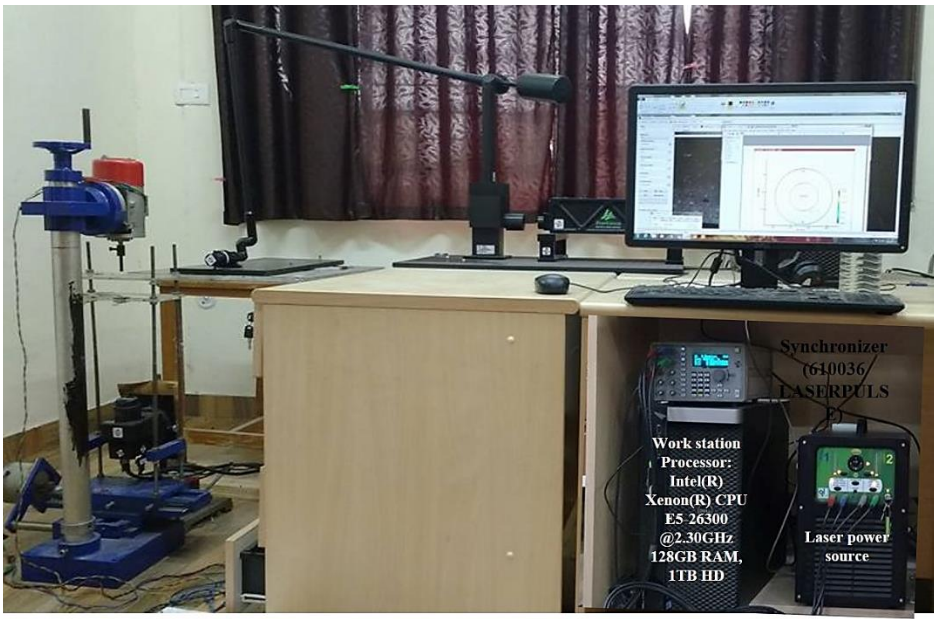

Fig. A1: Experimental arrangement for PIV image acquisition

Typically, PIV recordings are subdivided into small grid blocks in order to extract the local displacement information. These small grid blocks are referred as interrogation regions or interrogation areas (IAs) or interrogation windows (IWs). The principle of PIV image processing by means of statistical method i.e. cross-correlation is illustrated in Fig. A2. The local displacement vector (Δx) of the particles between first and second image in each IA is evaluated using the cross-correlation method. The most portable displacement recognized by the peak in the cross-correlation function is determined numerically by means of efficient Fast Fourier Transform (FFT). By calculating the local particle displacement and over the time, the local velocity and can be estimated within the IA. This process is repeated for all IAs to obtain the velocity vector map of the captured flow-field. However, the processing time of one image pair with several thousand instantaneous velocity vectors is mainly dependent on the size of the image pair, the interrogation area, and on the processing algorithm.

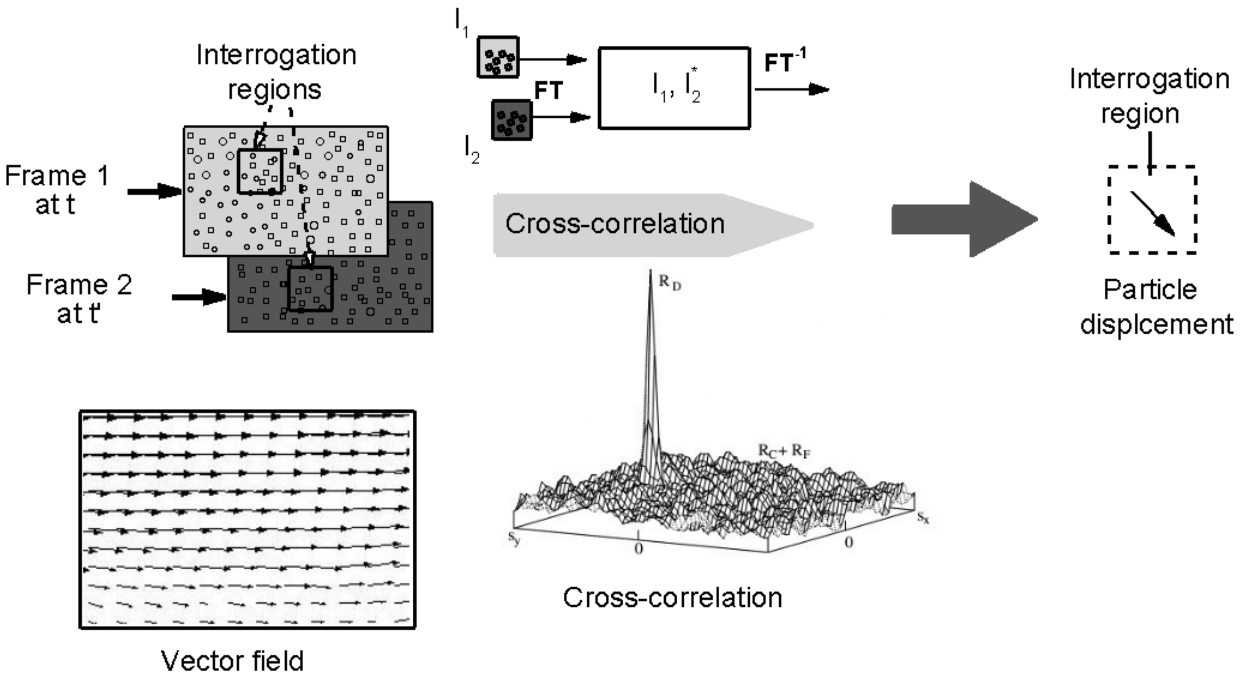

Fig. A2: PIV image processing.

Commercially available Microsoft® Windows®-based software named as INSIGHT 4G™ is used for global image capture, analysis, and display purposes during PIV measurements. Two basic methods of PIV image recording as recorded separately on individual frames (multi frame/single exposure) or multiple recorded on one frame (single/multi exposure) are available in this software, and the double-frame single exposure method is used in the present study for image acquisition.

These raw PIV images are further processed using cross-correlation algorithm to generate the velocity vector field. The cross-correlation algorithms available within the software are Fast Fourier Transform (FFT) Correlation, Hart Correlation, and Direct Correlation. FFT based algorithm is used in this work for the cross-correlation of initial and the final positions of the particle images. Particles are matched up to detect their spatially shifted partners and FFT is performed to produce the maximum correlation (i.e. peak value) over the IA and regarded as the particle displacement. The location in the correlation map is identified using Gaussian Peak as recommended for FFT correlation engine. The IA as well as the length of the sides has been taken equal. For better results, the number of particles per interrogation area should be at least 5 and the maximum particle displacement in an interrogation area should be equal to ¼ of the size of the interrogation area [150], see Fig. A3.

The grid engines of PIV cross-correlation available in the software are Nyquist Grid, Recursive Nyquist Grid, Rectangular Grid, and Deformation Grid. Nyquist Grid is the classic PIV grid and is generally used for fast results without spot offsets. Nyquist Grid uses 50% overlap of the subsequent IAs that results in limited spatial resolution of the velocity vectors, and processing uses only a single pass. Recursive Nyquist Grid is used for better accuracy with higher spatial resolution than Nyquist Grid. The images are processed in two passes: first pass computes the vector field according to Nyquist Grid with a starting window size and the second pass refines the vector field with optimized window offset based on the results of the first pass. Smaller window size for the second pass may be used to increase the vector resolution. Rectangular grid provides full control of grid parameter as compared to the Nyquist or Recursive Nyquist Grids. Deformation Grid is used for flows with high shears and for the highest accuracy. The images

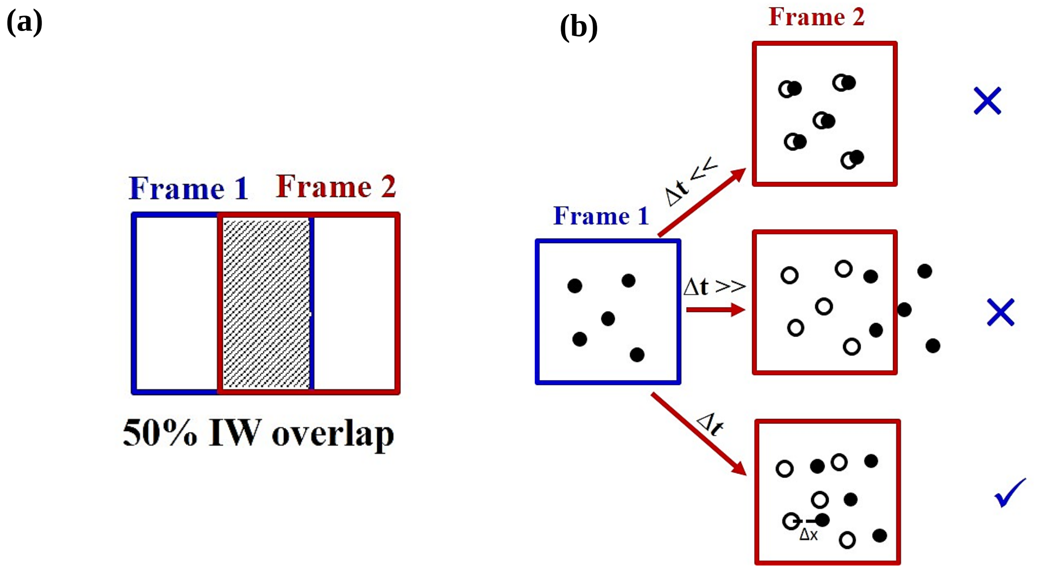

Fig. A3: Selection of pulse repetition time Δt.

are processed in multiple passes with image deformation before each pass by using the local flow found in the previous pass.

Design rules for PIV

- Proper laser light in the measurement section
- Over lapping between two images > 50%
- Image density $N_i > 10$ per IW
- In-plane motion $|\Delta X| < 0.25$ IW size
- Out-of-plane motion $|\Delta z| < 0.25$ light sheet thickness

A.3 Data acquisition and data reduction

In a turbulent flow, strong velocity variation within the interrogation volume causes gradient as well as the detection-bias and affects the measurements due to out-of-plane particle motion [150]. In this investigation, special attention has been paid towards deciding the optimal laser pulse separation time (Δt) for both laminar and turbulent flows. It has been taken care of that the particles move at the most eight pixels between the image pairs, and the ratio of out-of-plane displacement to the laser sheet thickness must be smaller than 0.25 [138, 155, 138]. Therefore, Δt has to be adjusted in order to optimize both the maximum cross-correlation value and the dynamic range. Based on the desired velocity magnitude and resolution, Δt is varied from 1000 to 2000 μs for different flow conditions. The number of images acquired for flow analysis (sample size) has also been recognized as one of the main source of error for determining the mean and fluctuating statistics in PIV experiments [125, 138, 155]. In order to meet the convergence of the statistical quantities, such as mean and fluctuating velocity components, sufficient number (N) of PIV images must be recorded and processed. For a straight channel with high blockage ribs mounted on one wall, an ensemble average of 300 samples is sufficient to provide a time-averaged flow field with a limited uncertainty in mean (< 5%) and rms (<10 %) velocities over the entire region of interest except for a small region in core of the shear layer [155]. Time-average of 200 PIV measurements of instantaneous fields was used to determine the mean flow velocity and second moments of pulsating velocity in rectangular duct with a rib [157]. However, most of the researchers in the pertinent field have found 1,000 PIV realizations to be suitable [125, 138, 156]. In the present investigations, 300-400 PIV realizations have been adopted; and therefore, during each of the experiments, 150-200 instantaneous image pairs at a frequency of 7.25 Hz are acquired. The parameters associated with PIV image acquisition for different measurement zones are compiled in Table A1. During image acquisition, the components of PIV data acquisition system should be operated in a particular sequence, as mentioned in the following points.

Step 1: Initially it has been ensured that all the components of the experimental setup are functioning correctly along with the proper alignment of the laser and the camera.

Step 2: The PIV components such as CCD camera, laser, and synchronizer are sequentially switched on. The INSIGHT-4G software pre-loaded on the PIV workstation is started and the data acquisition parameters such as method of synchronization, capture mode, number of realizations, laser pulse separation time, pulse energy and laser control (internal or external) are suitably entered.

Step 3: The component of the machine model, such as DC motor, synchronous motor and speed drive are switched on. The rotational speed (rpm) and traverse speed set for required experiment run. The rotational (rpm) is control by speed drive and measured by digital tachometer. The traverse speed is provided to the traversing table by synchronous motor and changed by changing the gear assembly between traversing table and synchronous motor shaft.

Step 4: The tool pin at pre-set rpm is insert in a seeded experimental material and the experimental material move toward the desired direction (forward or backward) at given traverse speed.

Step 5: Once the experimental move with a given speed to the test section, the image acquisition is started with the help of INSIGHT-4G^{TM} software and the synchronizer. And capture sufficient image pairs for processing.

Step 6: On completion of the image acquisition, the raw images have been stored in the hard drive for processing/post-processing.

The details mentioned in Table A2 have been adopted in the program for the determination of various parameters related to fluid flow.

Table A1: PIV acquisition parameters.

Area of interest (AOI)	200×200 mm^2
Actual image size	2048×2048 pixels
interrogation-window	16×16 pixels
Calibration factor	21.5 pixels/mm
Frequency (f)	7.5 Hz
Number of image pairs (N_i)	150-200
Pulse separation time (Δt)	500-3000 μs

Table A2: Determination of parameters related to flow.

parameter	Description
u_{rms} v_{rms}	Standard deviations shows the RMS fluctuation in the velocity at beach node from all the vector fields use to create average vector field. The u standard deviation and v standard deviation show the standard deviation of the single velocity component.
Velocity magnitude, V	$\sqrt{u^2 + v^2}$
$\frac{\partial u}{\partial x}$	$\frac{1000\{u(i+1,j) - u(i-1,j)\}}{\{x(i+1,j) - x(i-1,j)\}}$
$\frac{\partial v}{\partial x}$	$\frac{1000\{v(i+1,j) - v(i-1,j)\}}{\{x(i+1,j) - x(i-1,j)\}}$
$\frac{\partial u}{\partial y}$	$\frac{1000\{u(i,j+1) - u(i,j-1)\}}{\{y(i,j+1) - y(i,j-1)\}}$
$\frac{\partial v}{\partial y}$	$\frac{1000\{v(i,j+1) - v(i,j-1)\}}{\{y(i,j+1) - y(i,j-1)\}}$
Vorticity	$\frac{1000}{2}\left[\frac{\{v(i+1,j) - v(i-1,j)\}}{\{x(i+1,j) - x(i-1,j)\}} - \frac{\{u(i,j+1) - u(i,j-1)\}}{\{y(i,j+1) - y(i,j-1)\}}\right]$
Rate-of-strain	$1000\sqrt{2\left[\frac{\{u(i+1,j) - u(i-1,j)\}}{\{x(i+1,j) - x(i-1,j)\}}\right]^2 + \left[\frac{\{u(i,j+1) - u(i,j-1)\}}{\{y(i,j+1) - y(i,j-1)\}} + \frac{\{v(i+1,j) - v(i-1,j)\}}{\{x(i+1,j) - x(i-1,j)\}}\right]^2 + 2\left\{\frac{\{v(i,j+1) - v(i,j-1)\}}{\{y(i,j+1) - y(i,j-1)\}}\right\}^2}$

Appendix B

B.1 Calculation of differential flow properties

The vorticity and strain rates fields are both a consequence of the deformation tensor, which is:

$$\frac{d\vec{U}}{d\vec{X}} = \begin{bmatrix} \frac{du}{dx} & \frac{dv}{dx} & \frac{dw}{dx} \\ \frac{du}{dy} & \frac{dv}{dy} & \frac{dw}{dy} \\ \frac{du}{dz} & \frac{dv}{dz} & \frac{dw}{dz} \end{bmatrix}$$

When using the vorticity vector, $\vec{\omega}$, and the strain tensor, $\vec{\varepsilon}$, the deformation tensor can be expressed as:

$$\frac{d\vec{U}}{d\vec{X}} = \begin{bmatrix} \varepsilon_{xx} & \frac{\varepsilon_{xy}}{2} & \frac{\varepsilon_{xz}}{2} \\ \frac{\varepsilon_{yx}}{2} & \varepsilon_{yy} & \frac{\varepsilon_{yz}}{2} \\ \frac{\varepsilon_{zx}}{2} & \frac{\varepsilon_{zy}}{2} & \varepsilon_{zz} \end{bmatrix} + \begin{bmatrix} 0 & \frac{\omega_z}{2} & -\frac{\omega_y}{2} \\ -\frac{\omega_z}{2} & 0 & \frac{\omega_x}{2} \\ \frac{\omega_y}{2} & -\frac{\omega_x}{2} & 0 \end{bmatrix}$$

Where $\varepsilon_{ij} = {}^1\!/_2 \left({}^{\partial u_i}\!/_{\partial x_j} + {}^{\partial u_j}\!/_{\partial u_i} \right)$, and $\omega_i = \varepsilon_{ijk} \, {}^{\partial u_j}\!/_{\partial x_k}$ 2D PIV is a two-dimensional technique that can only provide two-components of the velocity, the measurable deformation matrix reduces to

$$\frac{d\vec{U}}{d\vec{X}} = \begin{bmatrix} \varepsilon_{xx} & \frac{\varepsilon_{xy}}{2} \\ \frac{\varepsilon_{yx}}{2} & \varepsilon_{yy} \end{bmatrix} + \begin{bmatrix} 0 & \frac{\omega_z}{2} \\ -\frac{\omega_z}{2} & 0 \end{bmatrix}$$

Since the third velocity component, and ${}^{d}\!/_{d_z}$ terms cannot be measured. Since the vorticity and strain rates fields cannot be directly measured, differentiation schemes must be used to derive these quantities. Such schemes, however, are susceptible to errors resulting from different grid spacing as well as noise within the velocity data. It is therefore important to be able to study and characterize various differentiation schemes in order to ascertain their performance.

In a study of several differentiation schemes, Raffel et al. [145] were able to document estimates for the first derivative, *df/dx*, of a function f(x) at a discrete location, *fi(xi)* (see Table B1). Here, ε_U is the velocity measurement uncertainty. The accuracy of each scheme is defined as the truncation error associated with each scheme, and the uncertainty of each scheme is dependent on the velocity measurement uncertainty within the velocity field. Table B1 suggests that the forward and backward differentiation schemes would perform poorly, as both their accuracies and uncertainties are the highest.

Table B1. First order differential operators for data spaced at uniform ΔX intervals along the x-axis, [145].

Operator	Implementation	Accuracy	Uncertainty
Forward difference	$\left(\frac{df}{dx}\right)_{i+1/2} \approx \frac{f_{i+1}-f_i}{\Delta x}$	O(ΔX)	$\approx 1.41\frac{\varepsilon_U}{\Delta X}$
Backward difference	$\left(\frac{df}{dx}\right)_{i-1/2} \approx \frac{f_i-f_{i-1}}{\Delta x}$	O(ΔX)	$\approx 1.41\frac{\varepsilon_U}{\Delta X}$
Centre difference	$\boldsymbol{\left(\frac{df}{dx}\right)_i \approx \frac{f_{i+1}-f_{i-1}}{2\Delta x}}$	$\mathbf{O(\Delta X^2)}$	$\boldsymbol{\approx 0.7\frac{\varepsilon_U}{\Delta X}}$
Richardson extrapolation	$\left(\frac{df}{dx}\right)_i \approx \frac{f_{i-2}-8f_{i-1}+8f_{i+1}-f_{1+2}}{12\Delta x}$	$O(\Delta X^3)$	$\approx 0.95\frac{\varepsilon_U}{\Delta X}$
Least squares	$\left(\frac{df}{dx}\right)_i \approx \frac{2f_{i+2}+f_{i+1}-f_{i-1}-2f_{1-2}}{10\Delta x}$	$O(\Delta X^2)$	$\approx 1.0\frac{\varepsilon_U}{\Delta X}$

Table B1 suggests that the centre differencing scheme should produce the best results since it best maximizes the accuracy while minimizing the uncertainty, it in fact does not perform as well as the least-squares scheme. Also of interest is the effect of the grid spacing. Table B1 suggests that reducing the size of the grid spacing should decrease the accuracy, while increasing the uncertainty.

B.2 Error in strain rate calculation close to the pin

The strain-rate is found to decrease with radial distance except first measured point, in the PIV results. Near the pin surface or first possible measured point in Fig. B1, the strain rate found less experimentally but in actual it has maximum value, compare to second. During processing every interrogation window has velocity vector and vectors formed throughout the plane of interest. Spurious or bad vectors are formed during the process and the main reason to form spurious vector are insufficient particle seeding density, in-plane loss-of-pairs, out-of-plane loss-of-pairs, insufficient light and gradients.

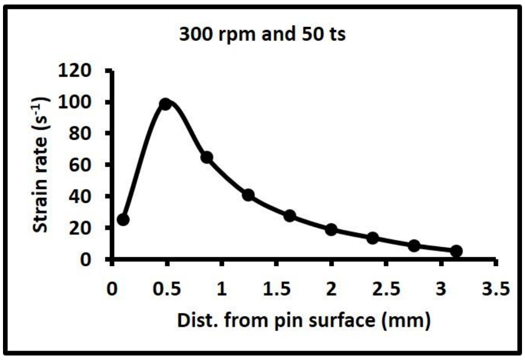

Fig. B1: Strain rate variation in radial direction from pin surface

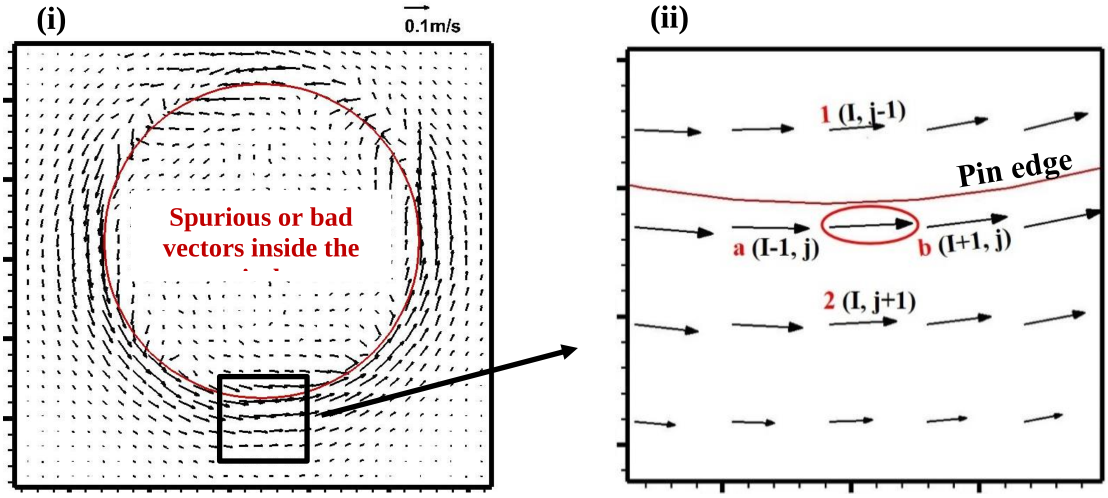

Fig. B2: i) Velocity vectors around the pin and spurious vectors inside the pin area, ii) enlarge area.

Herein the within the pin area, there is no light and seeding particle, hence pin area is formed a dark place. In dark place (inside red circle in Fig. B2) spurious vectors are formed as shown in Fig. B2. Since PIV provides the velocity vector field sampled on a two dimensional, evenly spaced grid, finite differencing has to be employed in the estimation of the special derivatives of the velocity gradient tensor, du/dx. For strain rate calculation centre difference method is used for PIV data and the differential operators for PIV data are shown in Table B1. In Fig. B2 (ii), the spurious vector 1 just inside the circle or pin area have almost same velocity magnitude as the second velocity vector 2 at the pin surface. Due to this, the velocity gradient near to the pin surface (1st point in Fig. B1) is small, hence the strain rate is also small.

Table B2: Velocities magnitude with respect to the co-ordinates and velocity gradient in x and y directions.

(I, j)	**(x (mm), y (mm), u (mm s^{-1}), v (mm s^{-1}))**
1 (I, j-1)	**(46.916, 36.727, 62.70, 4.87)**
2 (I, j+1)	**(46.916, 35.969, 77.25, 3.96)**
a (I-1, j)	**(46.537, 36.348, 88.36, -1.78)**
b (I+1, j)	**(47.29, 36.348, 92.36, 11.54)**

$$\frac{\partial u}{\partial x} = \frac{u_b - u_a}{x_b - x_a} = \left(\frac{92.36 - 88.36}{47.29 - 46.537}\right) = 5.31$$

$$\frac{\partial v}{\partial x} = \frac{v_b - v_a}{x_b - x_a} = \left(\frac{11.54 - (-1.78)}{47.29 - 46.537}\right) = 17.69$$

$$\frac{\partial u}{\partial y} = \frac{u_2 - u_1}{y_2 - y_1} = \left(\frac{77.25 - 62.7}{35.969 - 36.727}\right) = -19.32$$

$$\frac{\partial v}{\partial y} = \frac{v_2 - v_1}{y_2 - y_1} = \left(\frac{3.96 - 4.87}{35.969 - 36.727}\right) = -1.56$$

Mathematically we can understand the reason behind low value of strain rate close to the pin surface. Here we try to explain the strain rate at the vector inside the red colour ellipse in Fig. B2 (ii), can say measuring point. The coordinates of the measuring point and adjacent vectors, front (vector b), back (vector a), upper (vector 2) and lower (vector 1) are (i, j), (i+1,j), (i-1, j), (i, j-1) and (i, j+1), respectively and their respected values are shown in Table B2. Vector 2 is a bad or spurious vector formed by auto-correlation or cross-correlation, due to this, magnitude of vector 2 represent the wrong value. Hence the velocity gradient in y- direction, as shown in Table B2 with red colour, is incorrect.